FACTA UNIVERSITATIS

Series
AUTOMATIC CONTROL AND ROBOTICS
Vol. 23, № 1, 2024

$$mr\omega^2 h - mgr = 0$$

$$\omega = \frac{2\pi N}{60}$$

$$h = \frac{g \times 3600}{4\pi^2 N^2} = \frac{894.56}{N^2}$$

Scientific Journal FACTA UNIVERSITATIS publishes original high scientific level works in the fields classified accordingly into the following periodical and independent series:

Architecture and Civil Engineering	*Linguistics and Literature*	*Physical Education and Sport*
Automatic Control and Robotics	*Mathematics and Informatics*	*Physics, Chemistry and Technology*
Economics and Organization	*Mechanical Engineering*	*Teaching, Learning and Teacher Education*
Electronics and Energetics	*Medicine and Biology*	*Visual Arts and Music*
Law and Politics	*Philosophy, Sociology, Psychology and History*	*Working and Living Environmental Protection*

SERIES: **AUTOMATIC CONTROL AND ROBOTICS**

FACTA UNIVERSITATIS

SERIES **AUTOMATIC CONTROL AND ROBOTICS**
Vol. 23, Nº 1, 2024

UNIVERSITY OF NIŠ

INSTRUCTION FOR AUTHORS

As an author, you are kindly advised to use the paper template available for downloading on journal web site (section Download documents). This way you have nothing to change in terms of paper and text format. Simply applying the styles defined in the document will be sufficient.

Paper submitted for publication may be written in English, French or German (preferably in English) and submitted in the final camera-ready form. It is mandatory to submit your original work in Microsoft Word format (.doc not .docx) by using our online manuscript submission system. You have to make "New Submission" and upload your paper by using the online interface. All subsequent versions should be uploaded by using the same paper ID and your defined password. We are unable to process files sent by E-mail. We will do the final formatting and all necessary format conversions of your paper.

Articles are usually 10 to 25 type-written pages long. However, in special cases, shorter or longer articles may be accepted with appropriate reasoning. Author name, affiliation and complete address are to be placed underneath the title. Each paper should be preceded by a brief summary (50-150 words) in the same language. The text should be concise.

Letters, figures, and symbols should be clearly denoted so that no doubts about their meaning can arise. Symbols which may lead to confusion (e.g. letter I and figure 1, figure 0 and letter O) should be distinguished by marks which are explained in "Remarks for the typesetter".

Equations should be typewritten using MathType add-on (http://www.mathtype.com). For equations in your paper (Insert | Object | Create New | or MathType Equation), and, with the number, placed in parentheses at the right margin. Reference to equations should use the form "Eq. (2)" or simply (2). Each formula should occupy one line.

All figures should be numbered with consecutive Arabic numbers, have descriptive captions, and be mentioned in the text. Figures submitted must be of a standard high enough for direct reproduction. Line drawings should be prepared in electronic form. Figures should be planned in advance, so as to allow reduction to 12.75 cm in column width.

References should be quoted in the text by the corresponding number in square brackets and listed at the end of the manuscript in the order as they shown in the paper, in the same way as the following examples (for a journal, book, unpublished paper, proceeding, thesis, user manual, internet document):

[1]   B. M. Danković, "A class of almost orthogonal filters," Journal of Circuits, Systems, and Computers, vol. 18, no. 5, pp. 923–931, 2009. [Online]. Available: http://dx.doi.org/10.1142/S0218126609005447
[2]   J. H. Holland, *Adaptation in Natural and Artificial Systems*. University of Michigan Press, Ann Arbor, 1975.
[3]   M. T. Milojković, D. S. Antić, S. S. Nikolić, Z. D. Jovanović, S. Lj. Perić, "On a new class of quasi-orthogonal filters," International Journal of Electronics, [Online]. Available: http://dx.doi.org/10.1080/00207217.2012.743087, to be published.
[4]   M.-B. Radac, R.-A. Achimescu, R.-E. Precup, S. Preitl, C.-A. Dragos, A.-I. Stinean, "Design and experiments for model-free PI control of DC drives," in *Proceedings of 8th IEEE International Symposium on Applied Computational Intelligence and Informatics*, Timisoara, Romania, pp. 103–108, 2013. [Online]. Available: http://dx.doi.org/10.1225/sc.2013.018
[5]   D. Mitić, Digital variable structure systems based on input-output model. PhD thesis, University of Niš, Faculty of Electronic Engineering, 2006.
[6]   Inteco, "The laboratory anti-lock braking system controlled from PC," User's manual, 2008. [Online]. Available: www.inteco.com.pl
[7]   MATLAB, The Language of Technical Computing, 2013. [Online]. Available: http://www.mathworks.com/products/matlab [Accessed on December 2013].

Electronic submission. Papers for consideration should be submitted to the Series Editor in electronic form via the Journal's home page: http://casopisi.junis.ni.ac.rs/index.php/FUAutContRob/index.

Contents

Regular Papers

Survey Papers

Regular Paper

ADAPTATION OF THE FEEDBACK TRANSFER FUNCTION FOR OSICILATION BASED TESTING OF SECOND-ORDER ACTIVE RC FILTERS

UDC (621.3.018.8)

Dejan Mirković, Miljana Milić, Milena Stanojlović Mirković

University of Niš, Faculty of Electronic Engineering, Department of Electronics, Republic of Serbia

ORCID iDs: Dejan Mirković https://orcid.org/0000-0001-5877-1404
           Miljana Milić https://orcid.org/0000-0001-7037-7709
           Milena Stanojlović Mirković https://orcid.org/0000-0002-0935-6922

Abstract. *This paper, explores possible solutions for the feedback transfer functions applied in active RC filters for oscillation-based testing (OBT). Three types of filter transfer functions, namely low-pass (LP), high-pass (HP) and band-pass (BP) are examined. Active filters are realized with the realistic operational amplifier model targeting the 180nm CMOS technology. To confirm the theoretical insights, three realizations of LP, HP, BP second-order filterers with proposed feedbacks are designed and simulated. One of the solutions, namely the BP filter, is further examined by inserting defects in the circuit. Based on the time domain simulations, the key parameters are extracted from the oscillating filter's output signal. The fault dictionary has been created and appropriate classification of the defects is performed.*

Key words: *Feedback loop, active RC filters, transfer function, oscillation-based testing, fault dictionary.*

1. INTRODUCTION

High reliability of the contemporary electronic systems is in a high demand. Following the "more than Moor" law, these systems increase in size and complexity [1]. As a result, the testing structures should follow the same trend. However, more complex testing structures introduce additional costs in both time and resources. While the digital circuitry testing techniques are well established [2], testing of the analog circuitry is particularly

challenging due to a nearly infinite range in signal values and verity of functions that the circuit may implement.

In general, two systematic approaches are usually employed in testing and design of analog circuits. The first is known as the simulation-before-test (SBT) where the circuit under test (CUT) with the defect is simulated and the response of the circuit is recorded [3]. After the set of faulty circuits is simulated, the fault dictionary containing responses of the fault-free (FF CUT) and faulty circuits is formed. Based on the comparison between these responses the presence of the defect can be detected. SBT allows designers to identify and rectify potential issues in the design phase before physical prototypes are built, saving time and resources. The second approach is simulation-after-test (SAT) which provides insights into how the system performs under actual operating conditions, helping to identify discrepancies between simulation and reality. However, SAT is typically performed after the design has been finalized, limiting the opportunity for early detection and correction of design flaws. SAT approach involves expenses related to equipment, materials, and personnel, which can significantly increase development costs [4]. Therefore, SBT is usually favored over the SAT in early phases of testing since it is more flexible and less expensive to apply. In this work the SBT approach is adopted, as well.

The defects in the circuits are classified as the hard (catastrophic) and the soft (parametric) defects [5]. All defects that are radically changing the topology of the circuit are considered as hard defects. These defects are the result of the physical destruction of the component and/or connection between components (over-loading, systematic design errors, extreme working conditions etc.). Accordingly, hard defects are modeled as short circuits between nodes and open circuits of connection paths. When a hard defect is present in the circuit, significant degradation of the CUT performance is expected leading to permanent malfunction. On the other hand, soft defects do not jeopardize the CUT's functionality. Usually, only some properties are outside the specified limits (e.g. speed, bandwidth, power consumption, etc.), but the circuit still preserves its function. Soft defects can arise due to the component aging or suboptimal operational conditions such as variations in ambient temperature. For the circuit analysis the soft defects are modeled as the change in component value which lies outside the tolerance range.

When testing the analog circuitry several topics should be addressed. One would be in which domain to analyze the response of the circuit (DC, frequency, time, etc.). There is also a selection of the test point i.e. where the acquisition of the desired signal will take place. The availability of the test point sometimes cannot be easily ensured. One of the most challenging is the synthesis of the input test signal. Unlike with the digital circuitry, where only one format of the test vector is available (array of bits), with analog, there is a myriad of waveform shapes that can be applied as the test signal. Therefore, it is always interesting and challenging to consider the methodologies that guarantee the testing quality while requiring the fewest modification of the system. One such methodology is the Oscillation-Based Testing (OBT) [6],[7]. Several authors confirmed the value and usability of this technique in analog and mixed-signal filtering circuitry. In [8] the OBT technique was successfully applied to wideband current conveyer filters, and can be implemented as the Built-in Self-Test structure in Very-Large Scale Integrated circuits (VLSI) [9], [10]. The efficiency of OBT is in the fact that there is no need for the input test signal i.e. problem of the test signal synthesis is circumvented. Also, only one test point, usually the output of the CUT, is enough to observe the effect of the defects in the CUT. After the OBT is applied the diagnosis of the defects can be performed as shown in [11].

   The key idea behind OBT is to turn CUT into an oscillator [12]. To achieve this, one must provide some form of positive feedback in the system. This can be done in a verity of ways depending on the CUT transfer function. For the discrete time systems, like in [13], it is usually not possible to find closed form solution for the loop gain, but if the system is linear, there is a possibility to find the appropriate feedback transfer function which will enable sustained oscillations in the system. Therefore, the prime goal of this paper is to examine these possibilities for the three, second-order, filter transfer functions, namely: low-pass (LP), high-pass (HP) and band-pass (BP). Unlike the [14], where the comprehensive set of self-tuning active filters is covered, or the [15] where novel LC ladder passive network is presented, in this paper only the Sallen-Key RC realizations are considered [16],[17]. All filter, and feedback, circuits are designed with the realistic model of the operational amplifier targeting 180nm CMOS process node.

   The rest of the paper is organized in six sections. The second section will cover the basic theoretical background of the OBT methodology with the emphasis on filters application. Here, the appropriate feedbacks for the three examined filter structures will be discussed from the theoretical point of view. In the third section, the circuit realization of the OBT structures for the examined filters will be presented. The structures for the OBT of the band-pass (BP) filter will undergo additional testing using intentionally introduced defects. This process aims to illustrate the practical application of the OBT methodology alongside the newly proposed feedback transfer functions. The defects modeling for circuit simulation will be discussed in the fourth section. The fifth section will cover the simulation results and discussion regarding the theoretical and practical considerations. Finally, in the conclusion, key findings will be outlined.

2. THE OBT FEEDBACK TRANSFER FUNCTIONS

   To get the insight into the working principle of the OBT, the basic theoretical background will be briefly covered. Fig. 1 shows the general system with single positive feedback.
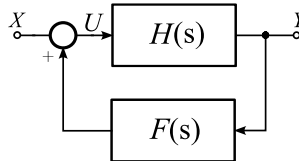
Fig. 1 General structure of the system with single positive feedback

Transfer function of the filter is denoted with $H(s)$ while the transfer function of the feedback is denoted with $F(s)$. The overall transfer function of the system is given by,

$$T(s) = \frac{Y}{X} = \frac{H(s)}{1 - F(s)H(s)} \tag{1}$$

   By observing (1), it can be concluded that the system becomes instable when loop gain $F(s)H(s)$ approaches unity. According to the Barkhausen stability criterion there are two simultaneous conditions that push the system toward the instability,

$$\left| F(j\omega)H(j\omega) \right| = 1 \qquad (2)$$

$$\angle \left\{ F(j\omega)H(j\omega) \right\} = 2k\pi, k = 0, 1, 2, \ldots \qquad (3)$$

i.e. the magnitude of the loop gain equals one and the phase is the integer multiple of the 2π radians [18]. The conditions (2) and (3) are usually used when analyzing the oscillators in the electronic circuits. On the other hand, one can also use the null of the system's determinant when $F(s)$ and $H(s)$ cannot be easily determined in the circuit. The system given in Fig. 1 can be described in a matrix form as,

$$\begin{bmatrix} 1 & -H(s) \\ -F(s) & 1 \end{bmatrix} \begin{bmatrix} Y \\ U \end{bmatrix} = \begin{bmatrix} 0 \\ X \end{bmatrix} \qquad (4)$$

where the determinant of the system is $\Delta(s) = 1 - F(s)H(s)$. For $F(s)H(s) = 1$,

$$Re\left\{ \Delta(j\omega) \right\} = 0 \qquad (5)$$

$$Im\left\{ \Delta(j\omega) \right\} = 0 \qquad (6)$$

i.e. real and imaginary part of the system's determinant simultaneously equals to zero. Therefore, either conditions (2) and (3) or (5) and (6) can be used as the theoretically well-established methods to relate the stability conditions and circuit's parameters. It should be noted that, when oscillator circuits are considered, like in OBT, there is no input signal i.e. $X=0$. It means that the system given in (4) may have infinite number of solutions or no solution [19]. However, by careful selection of the circuit parameters, one of the solutions can be ensured, i.e. sustained oscillations should be possible.

The choice of $F(s)$ strongly depends on the $H(s)$. The second-order low-pass and high-pass filter general transfer function is,

$$H_{LP}(s) = G \frac{1}{\left(s^2 / \omega_0^2 + s / (Q\omega_0) + 1 \right)}, \qquad (7)$$

where G is the low-frequency gain of the filter, Q is the quality factor, and ω_0 is the cutoff angular frequency of the filter. The phase characteristic of the low-pass transfer function (7) is given with,

$$\angle \left\{ H_{LP}(j\omega) \right\} = -\text{atan} \left(\frac{\omega / (Q\omega_0)}{1 - \omega^2 / \omega_0^2} \right). \qquad (8)$$

As the frequency ω approaches ω_0, (8) converges to the $-\pi/2$. To obtain the frequency of oscillations in vicinity of ω_0 feedback transfer function should introduce additional $\pi/2$ phase shift to fulfill the condition (3) for $k=0$. This can be achieved with the first order all-pass transfer function of a form,

$$F_{LP}(s) = -\frac{1 - {s}/{\omega_0}}{1 + {s}/{\omega_0}}, \tag{9}$$

which gives the following phase response,

$$\angle\{F_{LP}(j\omega)\} = \pi - 2\operatorname{atan}({\omega}/{\omega_0}). \tag{10}$$

Similarly, for the second order high-pass transfer function,

$$H_{HP}(s) = G\frac{{s^2}/{\omega_0^2}}{\left({s^2}/{\omega_0^2} + {s}/{(Q\omega_0)} + 1\right)}, \tag{11}$$

with phase response,

$$\angle\{H_{HP}(j\omega)\} = \pi - \operatorname{atan}\left(\frac{{\omega}/{(Q\omega_0)}}{1 - {\omega^2}/{\omega_0^2}}\right), \tag{12}$$

the appropriate $F(s)$ would be the sign inverted (9), i.e.,

$$F_{HP}(s) = \frac{1 - {s}/{\omega_0}}{1 + {s}/{\omega_0}}, \tag{13}$$

$$\angle\{F_{HP}(j\omega)\} = -2\operatorname{atan}({\omega}/{\omega_0}). \tag{14}$$

In case of a high-pass filter, the feedback provides additional $-\pi/2$ of the phase shift, to compensate for the $\pi/2$ obtained in (12) when ω approaches ω_0. In (11), G represents the high-frequency gain of the filter.

The general form of the second order band-pass filter transfer function and associated phase response are,

$$H_{BP}(s) = G\frac{{s}/{\omega_0}}{\left({s^2}/{\omega_0^2} + {s}/{(Q\omega_0)} + 1\right)} \tag{15}$$

$$\angle\{H_{BP}(j\omega)\} = \frac{\pi}{2} - \operatorname{atan}\left(\frac{{\omega}/{(Q\omega_0)}}{1 - {\omega^2}/{\omega_0^2}}\right). \tag{16}$$

According to (16), in a vicinity of ω_0, condition (3) is automatically fulfilled. Therefore, the simple unity feedback should be enough to open the possibility for sustained oscillations, i.e. $F_{BP}(s) = 1$. In this case ω_0 is the central frequency of the filter, and the expected gain for $\omega = \omega_0$ is $G_0 = GQ$.

The influence of the proposed $F(s)$ to the $H(s)$ is illustrated in Fig. 2 where the frequency responses of the open loop transfer functions, $H(s)F(s)$, are shown. All examples are given for the $f_0 = \omega_0/(2\pi) = 10$kHz.

a) $H_{LP}(s)F_{LP}(s)$, $G=2$, $Q=1$ b) $H_{HP}(s)F_{HP}(s)$, $G=2$, $Q=1$

c) $H_{BP}(s)F_{BP}(s)$, $G=2/\sqrt{2}$, $Q=\sqrt{2}/2$, $G_0=1$
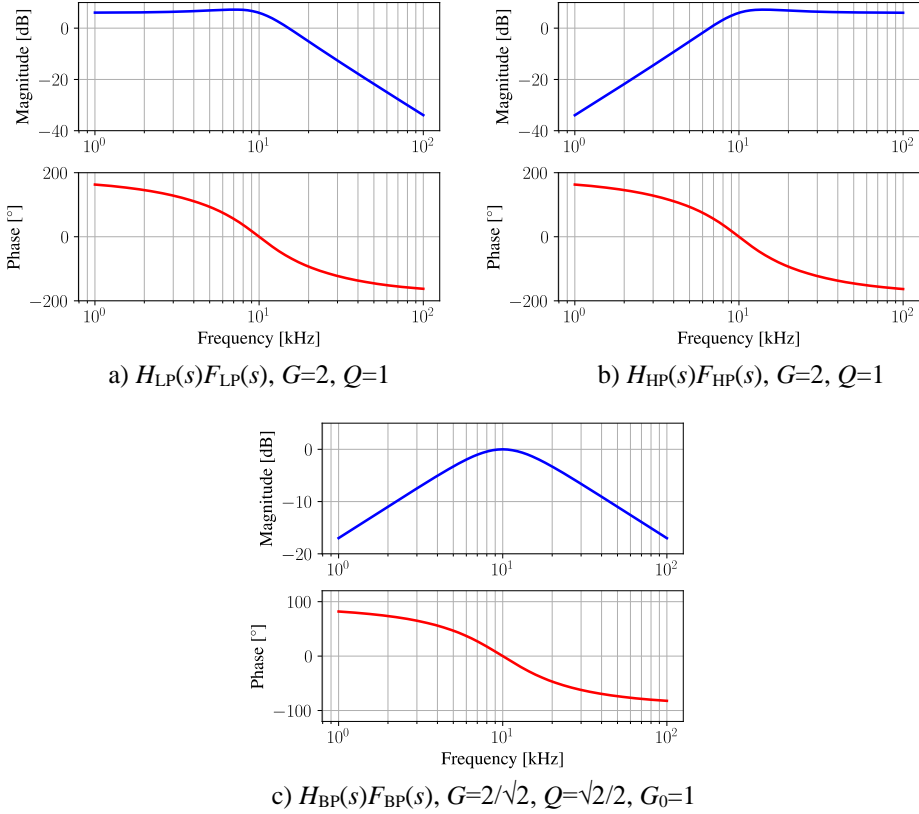
Fig. 2 Frequency responses of the $F(s)H(s)$ for a) LP, b) HP and c) BP cases, $f_0 = \omega_0/(2\pi)$ =10kHz

As can be seen from Fig. 1a and Fig. 1b the introduced all-pass $F(s)$ ensures the zero crossing of phase for the LP and HP filters at the $\omega = \omega_0$. This is also the case for the BP filter with unity feedback shown in Fig. 1c. For all three cases LP, HP, and BP there is a continuous, monotonic, phase response. By now only the phase response is considered i.e. the proposed feedback transfer functions are derived with respect to the phase responses only (condition (3)). To achieve the sustained oscillations, condition (2) must also be met, i.e. there must be enough gain/attenuation in the loop. This is the part that will be determined experimentally by adjusting the gain of the filter. The gain will be held in the allowed boundaries to keep the filter in the stable state when proposed $F(s)$ is not applied. As it will be discussed in the next section, for the examined circuit realizations, G and Q parameters are mutually dependent thus by choosing one, the other is automatically determined.

3. CIRCUIT REALIZATION OF THE OBT STRUCTURES

In this section circuit realization of the proposed OBT structures will be discussed. The LP, HP and BP have the Sallen-Key topologies. To obtain highly realistic simulation results, the model of the operational amplifier (opamp) designed for the 180nm CMOS technology process is utilized. The internal topology of the employed opamp is shown in Fig. 3. The topology contains the folded cascode input stage (transistors M1-M12) and inverter-based class-AB output stage (transistors M13 and M14) biased with the floating voltage reference source (transistors M15-M18). The BP1-3 and BN1-3 are the voltage biasing points for the entire opamp [20]. The opamp is internally compensated with the $C_1=C_2=1.2$pF and $R=1.5$kΩ. The nominal power supply voltage for the 180nm technology is 1.8V and the common-mode voltage for the signals is set to $V_{CM}=1$V.
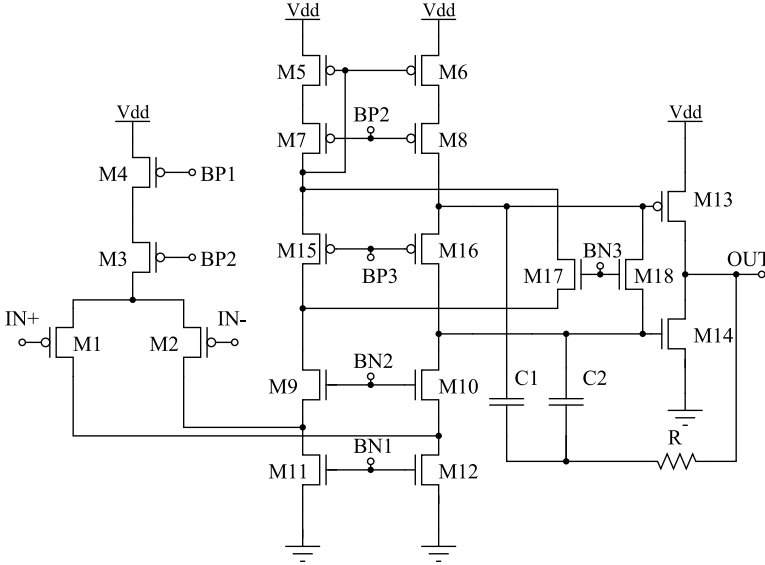
Fig. 3 The schematic of the opamp model used in realization of the OBT filter structures

Table 1 summarizes the key opamp parameters, where the DC-gain (A_{DC}), gain-bandwidth product (*GBW*), phase margin (*PM*), settling time (t_s) and slow-rate (*SLR*), are given for the unity-gain configuration. The opamp itself will introduce some phase shift as well. However, this should not contribute significantly to the overall loop phase shift since The Gain-Bandwidth Product (GBW) exceeds the target Oscillation-Based Testing (OBT) oscillation frequency, f_0, by three orders of magnitude, where f_0 is set at 10kHz. Therefore, in further derivations of the circuit transfer functions opamp will be considered as an ideal.

Table 1 The key opamp parameters

A_{DC} [dB]	*GBW* [MHz]	*PM* [°]	t_s [ns]	*SLR* [V/μs]
103.16	38.72	58.80	268.46	23.72

The proposed circuit realization of the OBT structures for the LP and HP filters are shown in Fig. 4a and Fig. 4b, respectively. The test mode is selected by setting the switch at the position 1. The normal mode of operation is for the switch position 0.

a) LP OBT   b) HP OBT
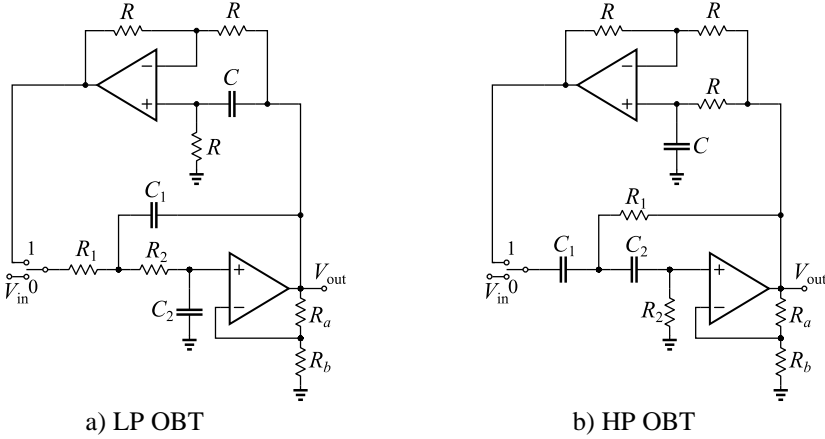
Fig. 4 The OBT structures for the LP and HP filters

As suggested in (9) and (13) the first order all-pass filters are connected between the output node (V_{out}) and the switch node 1. Assuming an ideal opamp the transfer functions of first-order all-pass filters are,

$$F_{LP,HP}(s) = p \cdot \frac{1-sRC}{1+sRC}, p = \begin{cases} -1 & for\ LP \\ 1 & for\ HP \end{cases} \quad (19)$$

According to (19) the RC constant should satisfy the relation, $\omega_0 = 1/(RC)$. The general form of Q and ω_0 for the LP and HP filters from Fig. 4 are,

$$\omega_0 = \frac{1}{\sqrt{C_1 R_1 C_2 R_2}}, Q = \begin{cases} \left[(1-G)\sqrt{\frac{R_1}{R_2}\frac{C_1}{C_2}} + \left(\sqrt{\frac{R_1}{R_2}} + \sqrt{\frac{R_2}{R_1}}\right)\sqrt{\frac{C_2}{C_1}} \right]^{-1} & for\ LP \\ \left[(1-G)\sqrt{\frac{R_2}{R_1}\frac{C_2}{C_1}} + \left(\sqrt{\frac{C_2}{C_1}} + \sqrt{\frac{C_1}{C_2}}\right)\sqrt{\frac{R_1}{R_2}} \right]^{-1} & for\ HP \end{cases}, \quad (20)$$

where, $G = 1 + R_a/R_b$. Since the prime goal is the proof-of-concept i.e. to force the CUT to oscillate, following simplifications are made, $R_1 = R_2 = R$, $C_1 = C_2 = C = 1/(\omega_0 R)$ leaving the R_a/R_b as the free parameter that sets both, G and Q of the filter. For this choice of component values, G should be smaller than three to keep the filter stable since, $Q = 1/(3 - G)$.

The proposed OBT structure for the BP filter is shown in Fig. 5. According to (16) only unity feedback should be applied.
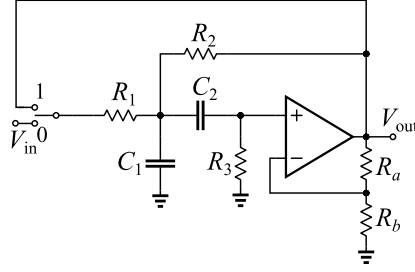
Fig. 5 The OBT structures for the BP filter

The Q and ω_0 for the BP shown in Fig. 5 are,

$$\omega_0 = \frac{1}{\sqrt{C_1(R_1 \parallel R_2)C_2R_3}}, Q = \omega_0\left[\frac{1}{C_2R_3} + \frac{1}{C_1R_1}\left(1 + \frac{R_1}{R_3} + (1-G)\frac{R_1}{R_2}\right)\right]^{-1}, \qquad (21)$$

Selecting the $R_1=R_2=R$ and $C_1=C_2=C$, results with the $\omega_0=\sqrt{2}/(RC)$ and $Q=\sqrt{2}/(4-G)$. The filter's stability is preserved for the G smaller than four.

4. DEFECTS MODELING FOR CIRCUIT SIMULATION

To demonstrate the application of the proposed OBT structures one of them will be additionally analyzed by introducing defects into the passive components. The BP OBT structure is chosen for this purpose. Two types of hard defects are introduced namely, the stack-at-short (SAS) and the stack-at-open (SAO). In the circuit simulation, the SAS is modeled by setting the small resistance of $1m\Omega$ across the component terminals while the SAO is modeled by the large resistance of $1T\Omega$ in series with the component. The extremely small resistance value of $1m\Omega$ ensures that the voltage drop for the expected mA currents will be in the sub μV range that can be considered as a short circuit. Also, $1T\Omega$ resistances should keep the currents in pA range for voltages of the order of 1V modeling the open circuit.

Considering that the variation of the on-chip resistances and capacitances is very large (about 20%), the significant amount of component value change must be introduced to provoke the soft defect [21]. Since on-chop components are realized as the polygons of the certain width, W, and lengths, L, the soft defects are modeled by relating the ±50% change of component dimensions (W and/or L) to the component value. It is important to note that the resistance value is proportional to the L/W ratio and that the capacitance value is proportional to the WL product. E.g. changing the L and W in the same direction by the same amount will not influence the resistance but will influence the capacitance value. On the other hand, by changing the L and W in the opposite directions by the same amount will not influence the capacitance value (area stays the same) but it will influence the resistance value. Therefore, adopted absolute change in the resistance and capacitance values from the nominal one are $\Delta R = [-67\%, -50\%, -33\%, 50\%, 100\%, 200\%]$ and $\Delta C = [-75\%, -50\%, 50\%, 125\%]$, respectively. In total there are six soft defects for each resistor and four for each capacitor. Since, BP filter contains five resistors and two capacitors the total number of the soft defects is thirty-eight. Considering two hard defects per component the total number of hard defects is fourteen.

5. SIMULATION RESULTS

The SPICE simulation results for the OBT structures of the LP, HP and BP filters are shown in Fig. 6. The waveforms of the output voltage, V_{out}, are given in subfigures a), c) and e) while the corresponding spectrum, obtained from 4096-point FFT, is given in subfigures b), d) and f). Based on the waveforms, it takes about 0.4ms for the OBT structures to start oscillating. It can be concluded that the theoretical assumptions regarding the proposed feedback transfer functions are valid.

a) LP OBT waveform

b) LP OBT spectrum

c) HP OBT waveform

d) HP OBT spectrum

e) BP OBT waveform

f) BP OBT spectrum
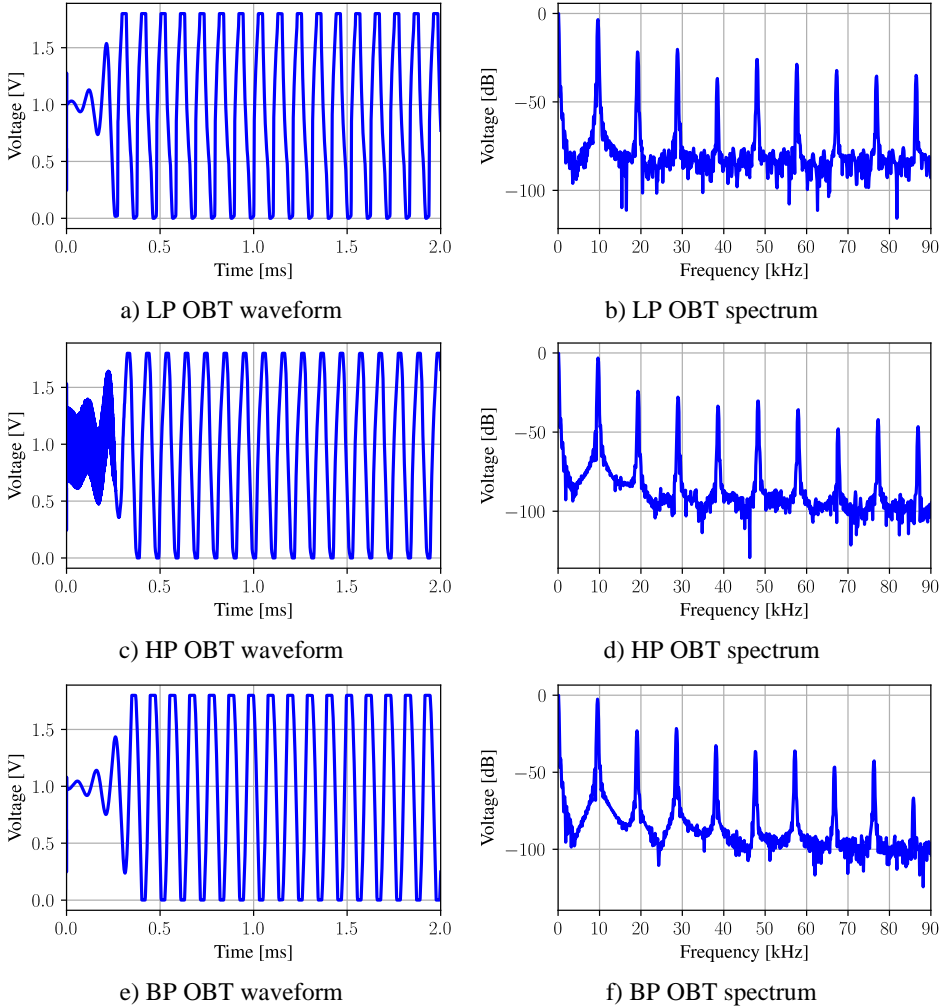
Fig. 6 The simulation results for the LP, HP, and BP OBT structures

The columns two through four in Table 2 summarize the most-commonly observed parameters for the FF CUT when OBT is applied. These parameters are, oscillating frequency, f_0, output voltage amplitude, V_{out}, the total-harmonic distortion, *THD* (calculated up to 10th

harmonic) and average supply current, I_{DD}. Due to the component non-idealities, obtained oscillating frequency slightly differs from the target 10kHz.

Table 2 The OBT parameters for the FF CUT in test mode

CUT	f_0 [Hz]	V_{out} [mV]	THD* [%]	I_{DD} [mA]	G	Q	C [pF]	R [kΩ]	R_a [kΩ]
LP	9645	900	22.37	1.296	2	1	45	350	50
HP	9645	900	12.70	1.407	2	1	45	350	50
BP	9564	900	12.43	1.192	2.25	0.808	60	375	62.5

* Calculated up to 10th harmonic

The values of the G and Q are given in the sixth and seventh column, respectively. The nominal values of the components are given in the last three columns. R_b is set to 50kΩ in each realization. Since the integrated circuits implementation is intended, relatively large value is chosen for R to keep the values of C in pF range ($\omega_0 \propto 1/(RC)$).

The complete fault dictionary for fourteen hard defects introduced into the BP OBT structure is given in Table 3. The first two columns contain the component name and the defect type. The rest of the columns contains the observed parameters. The defects are detected by tracking the deviation between parameters of the FF CUT and the faulty CUT.

Table 3 The fault dictionary for hard defects of the BP OBT structure

Comp.	Defect	f_0 [Hz]	V_{out} [V]	I_{DD} [A]	THD [%]
C_1	SAO	187.08E+3	899.77E-3	430.72E-6	7.08
C_2	SAO	-	10.88E-15	1.192E-3	-
R_1	SAO	-	6.83E-15	1.192E-3	-
R_2	SAO	-	115.77E-18	147.64E-6	-
R_3	SAO	-	249.80E-15	1.192E-3	-
R_a	SAO	-	62.01E-15	1.192E-3	-
R_b	SAO	1.32E+3	900.00E-3	188.11E-6	25.55
C_1	SAS	-	5.27E-15	1.192E-3	-
C_2	SAS	-	1.89E-15	199.27E-6	-
R_1	SAS	14.96E+3	899.77E-3	516.28E-6	44.68
R_2	SAS	-	3.77E-15	1.192E-3	-
R_3	SAS	18.14E+3	899.77E-3	188.78E-6	9.38
R_a	SAS	1.33E+3	899.65E-3	194.89E-6	25.39
R_b	SAS	-	62.51E-15	1.192E-3	-

The hard defects classification for the BP OBT structure is presented in Table 4. The total coverage is 100% since the effect of all introduced defects is such that changes one or more of the observed parameters of the FF CUT. Two classes of the response are identified: Oscillations and No-oscillations. The Oscillations class covers the defects that do not change the oscillation frequency of the OBT structure but changes one of the other observed parameters (V_{out}, THD or I_{DD}). The No-oscillation class contains the defects that do not allow oscillations (denoted with a dash in the frequency and THD columns of Table 3). In the case of the BP OBT structure there are five defects in Oscillation class and they can be detected by *THD* or the I_{DD} deviation from the same parameters of the FF CUT given in Table 2 (BP row).

There are nine defects in the No-oscillation class, where two of them can be detected by the deviation of I_{DD} (R_2 SAO and C_2 SAS) and five cannot be diagnosed since they produce no change in the power supply current, I_{DD}.

Table 4 Classification of hard defects for the BP OBT structure

Response class	Oscillations	No oscillations	
Diagnosed	by frequency, THD or current	by current	Undiagnosed
Number	5	2	7
Percentage	35.71%	14.29%	50.00%

The fault dictionary for the soft defects in resistors and capacitors of the BP is presented in Tables 5 and 6, respectively. Again, 100% coverage is achieved. In this case the fifty-fifty split between Oscillations and No-oscillations classes is identified as summarized in Table 7.

Table 5 The fault dictionary for soft defects in resistors of the BP OBT structure

Comp.	ΔR [%]	f_0 [Hz]	V_{out} [V]	I_{DD} [A]	THD [%]
R_1	200	-	156.60E-15	1.192E-3	-
	100	-	74.95E-12	1.192E-3	-
	50	-	18.80E-6	1.192E-3	-
	-33	9.75E+3	899.70E-3	954.000E-6	4.14
	-50	10.35E+3	899.80E-3	818.700E-6	15.67
	-67	11.00E+3	899.80E-3	714.700E-6	32.51
R_2	200	4.11E+3	899.80E-3	474.500E-6	20.27
	100	5.62E+3	899.80E-3	598.600E-6	16.83
	50	6.96E+3	899.80E-3	754.500E-6	22.93
	-33	-	319.90E-15	1.192E-3	-
	-50	-	142.30E-15	1.192E-3	-
	-67	-	67.34E-15	1.192E-3	-
R_3	200	-	443.30E-15	1.192E-3	-
	100	-	35.92E-12	1.192E-3	-
	50	-	7.98E-6	1.192E-3	-
	-33	10.00E+3	899.80E-3	805.300E-6	20.21
	-50	10.64E+3	899.80E-3	651.200E-6	8.89
	-67	11.50E+3	899.80E-3	511.000E-6	29.17
R_a	200	-	148.40E-15	1.192E-3	-
	100	-	254.70E-15	1.192E-3	-
	50	-	592.60E-15	1.192E-3	-
	-33	8.42E+3	899.70E-3	673.200E-6	19.14
	-50	7.61E+3	899.70E-3	516.700E-6	15.00
	-67	6.43E+3	899.70E-3	365.800E-6	26.31
R_b	200	96.42E+3	899.90E-3	352.000E-6	22.38
	100	7.58E+3	899.80E-3	510.000E-6	20.73
	50	8.49E+3	899.80E-3	676.400E-6	25.32
	-33	-	597.40E-15	1.192E-3	-
	-50	-	274.10E-15	1.192E-3	-
	-67	-	156.20E-15	1.192E-3	-

One half of soft defects does not produce oscillations but preserve the same I_{DD} as the FF CUT (undiagnosed). The other half of soft defects keeps the OBT structure in the oscillation state and can be diagnosed by deviation in frequency, THD or I_{DD}. Finally, for a better insight the classification results given in Tables 4 and 7 are presented graphically in Fig. 7

Table 6 The fault dictionary for soft defects in capacitors of the BP OBT structure

Comp.	ΔC [%]	f_0 [Hz]	V_{out} [V]	I_{DD} [A]	THD [%]
	125	-	155.00E-15	1.192E-3	-
C_1	50	-	227.50E-9	1.192E-3	-
	-50	11.70E+3	899.80E-3	778.900E-6	6.88
	-75	13.89E+3	899.80E-3	624.800E-6	17.04
	125	5.61E+3	899.80E-3	760.500E-6	17.35
C_2	50	7.27E+3	899.80E-3	910.700E-6	3.42
	-50	-	189.10E-15	1.192E-3	-
	-75	-	60.73E-15	1.192E-3	-

Table 7 Classification of soft defects for the BP OBT structure

Response class	Oscillations	No oscillations
Diagnosed	by frequency, THD or current	Undiagnosed
Number	19	19
Percentage	50.00%	50.00%

a) Hard defects   b) Soft defects
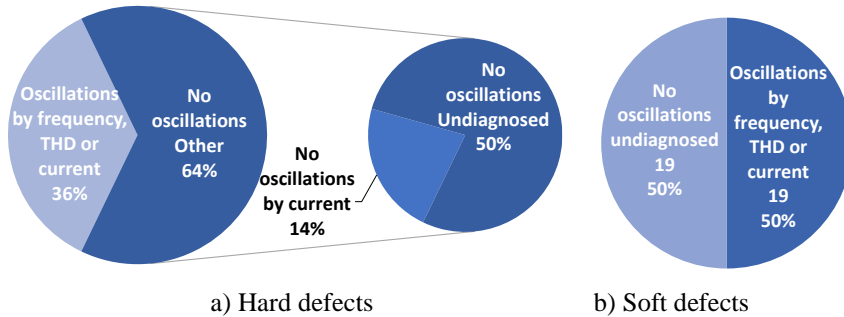
Fig. 7 The share of the diagnosed/undiagnosed defects in the response classes for the BP OBT structure

6. CONCLUSION

In this paper, possible solutions for the feedback transfer functions applied in OBT test structures of active RC filters are examined. The proposed feedback transfer functions are successfully applied to three types of second-order Sallen-Key filters LP, HP, and BP. The solutions are derived according to the phase responses of the examined filters.

For each examined filter the key relations between filters' cut-off/central frequency, Q factor and the gain G, are derived. Based on these relations an appropriate strategy for selecting the values of the circuit's elements is given.

The proposed OBT structures are custom designed targeting the 180nm CMOS process. The internal topology and main characteristics of the opamp are presented. The opamp is designed with the goal of minimizing its influence on the overall frequency characteristics of the filter. The theoretical assumptions regarding proposed feedback functions are confirmed with the SPICE simulations showing that all three of the proposed OBT structures oscillate at the filters cut-off/central frequency.

The OBT is further demonstrated on the OBT BP structure where total of fourteen hard and thirty-eight soft defects are introduced into the BP passive components. In both cases 100% defect coverage is achieved. For better insight the defects are classified first by the response type, and then by the parameter that can be used for the defect diagnosis.

There are two main contributions of this work. Firstly, it is the introduction of the all-pole transfer functions in the LP and HP OBT structures which enabled the oscillation frequency near the filters' cut-off frequency. These cases are not previously examined in [11] and [13]. Secondly, based on the simulation results for the BP OBT structure, it was shown that tracking the power-supply current as an additional parameter to the output voltage waveform and spectrum, improvements in the defects diagnosis can be achieved (e.g. 14% in the No-oscillations class, for hard defects, Fig. 7a). In the future work the proposed methodology could be applied to different circuit topologies with the goal of exploring the possibilities for the defects' detection and diagnosis.

REFERENCES

[1] G. Q. Zhang, M. Graef, and F. van Roosmalen," The rationale and paradigm of "more than Moore", *56th Electronic Components and Technology Conference 2006*, San Diego, CA, USA, 2006, pp. 7, doi: 10.1109/ECTC.2006.1645639.

[2] S. Qamar, W. H. Butt, M. W. Anwar, F. Azam, and M. Q. Khan, "A Comprehensive Investigation of Universal Verification Methodology (UVM) Standard for Design Verification," *Proceedings of the 2020 9th International Conference on Software and Computer Applications*, 2020, pp. 339–343, doi: 10.1145/3384544.3384547.

[3] M. Karmani, C. Khedhiri, B. Hamdi, and B. Bensalem, "A Fault Dictionary-Based Fault Diagnosis Approach for CMOS Analog Integrated Circuits," *International Journal of VLSI Design & Communication Systems*, vol. 2, no. 3, 2011, doi: 10.5121/vlsic.2011.2301.

[4] D. Monda, G. Ciarpi, and S. Saponara, "Diagnosis of faults induced by radiation and circuit-level design mitigation techniques: Experience from vco and high-speed driver cmos ics case studies," *Electronics (Switzerland)*, vol. 10, no. 17, 2021, doi: 10.3390/electronics10172144.

[5] D. Perry, M. Nakamoto, N. Verghese, P. Hurat, and R. Rouse, "Model-based approach for design verification and co-optimization of catastrophic and parametric-related defects due to systematic manufacturing variations," *Design for Manufacturability through Design-Process Integration*, 2007. doi: 10.1117/12.712471.

[6] K. Arabi and B. Kaminska, "Oscillation-test methodology for low-cost testing of active analog filters," *IEEE Trans Instrum Meas*, vol. 48, no. 4, pp. 798–806, 1999, doi: 10.1109/19.779176.

[7] M. Milić, M. A. Stošović, and V. Litovski, "Oscillation based analog testing A case study," Proceedings of the 34th International Convention on Information and Communication Technology, Electronics and Microelectronics – MIPRO, vol. 1, pp. 118-123, May, 2011, ISBN 1847-3938.

[8]   P. Petrashin, L. Toledo, W. Lancioni, P. Osuch, and T. Stander, "Oscillation-Based Test Applied to a Wideband CCII," *VLSI Design*, vol. 2017, 2017, doi: 10.1155/2017/5075103.

[9]   M. Ballot and T. Stander, "A RF amplifier with oscillation-based BIST based on differential power detection," *Proceedings - IEEE International Symposium on Circuits and Systems*, 2021. doi: 10.1109/ISCAS51556.2021.9401388

[10] H. P. Nel, T. Stander, and F. C. Dualibe, "Built-In Oscillation-Based Self-Testing of a 2.4 GHz LNA in 0.35μ m CMOS," *2018 25th IEEE International Conference on Electronics Circuits and Systems, ICECS 2018*, 2018. doi: 10.1109/ICECS.2018.8618052.

[11] M. A. Stošović, M. Milić, and V. Litovski, "Analog filter diagnosis using the oscillation based method," *Journal of Electrical Engineering*, vol. 63, no. 6, 2012, doi: 10.2478/v10187-012-0052-4.

[12] M. Petrovic and M. Milic, "Analog Device Design for Testability in the Case of Oscillation Based Testing," *Proceedings of the International Conference on Microelectronics, ICM*, 2017. doi: 10.1109/MIEL.2017.8190122.

[13] M. Milic and V. Litovski, "Oscillation-based testing method for detecting switch faults in High-Q SC biquad filters," *Facta Universitatis, Series: Electronics and Energetics*, vol. 28, no. 2, 2015, doi: 10.2298/fuee1502223m.

[14] D. Mitić, G. Jovanović, M. Stojčev, and D. Antić, "On Design of Self-tuning Active Filters," *Facta Universitatis, Series: Automatic Control and Robotics*, vol. 19, no. 1, 2020, doi: 10.22190/fuacr2001059m.

[15] D. Živaljević and S. V. Nikolić, "New Type of Nearly Monotonic Passband Filters with Sharp Cutoff," *Facta Universitatis, Series: Automatic Control and Robotics*, vol. 16, no. 1, 2017, doi: 10.22190/fuacr1701061z.

[16] R. P. Sallen and E. L. Key, "A practical method of designing RC active filters," *IRE Transactions on Circuit Theory*, vol. 2, no. 1, 1995, doi: 10.1109/tct.1955.6500159.

[17] V. Litovski, "Active RC Cascade Circuit Synthesis," in Lecture Notes in Electrical Engineering, vol. 596, 2019. doi: 10.1007/978-981-32-9852-1_15.

[18] L. Von Wangenheim, "On the Barkhausen and Nyquist stability criteria," *Analog Integrated Circuits and Signal Processing*, vol. 66, no. 1, 2011, doi: 10.1007/s10470-010-9506-4.

[19] A. G. S. Ventre, "Determinants and Systems of Linear Equations," in *Calculus and Linear Algebra*, (2023). doi: 10.1007/978-3-031-20549-1.

[20] M. P. Garde, A. Lopez-Martin, R. G. Carvajal, and J. Ramírez-Angulo, "Super Class-AB Recycling Folded Cascode OTA," *IEEE J Solid-State Circuits*, vol. 53, no. 9, 2018, doi: 10.1109/JSSC.2018.2844371.

[21] D. D. Mirkovic, M. J. Stanojlovic Mirkovic, M. L. J. Milic, and V. Z. Petrovic, "A Defects Classification Algorithm for the Hybrid OBT–IDDQ Fault Diagnosis Technique in Analog CMOS Integrated Circuits," *Journal of Circuits, Systems and Computers*, vol. 0, no. 0, p. 2450146, doi: 10.1142/S0218126624501469.

Regular Paper

SKEW CONTROL OF RAIL MOUNTED WIDE SPAN MULTI-MOTOR DRIVES

UDC (621.313.323)

Vojkan Kostić, Nebojša Mitrović, Milutin Petronijević, Bojan Banković, Filip Filipović

University of Niš, Faculty of Electronic Engineering, Department of Power Engineering, Republic of Serbia

ORCID iDs: Vojkan Kostić   https://orcid.org/0000-0002-7714-469X
         Nebojša Mitrović   https://orcid.org/0000-0003-3767-3244
         Milutin Petronijević   https://orcid.org/0000-0003-2396-0891
         Bojan Banković   https://orcid.org/0000-0002-5504-599X
         Filip Filipović   https://orcid.org/0000-0002-1930-9273

Abstract. *In this paper, the construction skewing problem of rail mounted wide span multi-motor drives is considered. A new skew control algorithm is proposed, and the controller design is analyzed in detail. Additionally, a PLC program algorithm for the practical implementation of the proposed solution is presented. The practical implementation of the skew control is described as a concrete example from an industrial environment. Subsequently, in order to determine performance, the characteristic time dependencies were recorded.*

Key words: *Skew control, rail mounted wide span multi-motor drive, gantry crane.*

1. INTRODUCTION

The application of controlled multi-motor drives is very common in the industry [1]. Motor operation control of multi-motor drives is realized at the control level of the entire multi-motor drive, usually utilizing programmable logic controllers (PLCs) and industrial communication networks. As a rule, high control performance is achieved by employing controlled electric motor drives that utilize various vector control methods for precise speed/torque regulation. A comparison of different control structures for controlled multi-

motor drives is presented in [2,3]. Examples of electric motor drive applications in different branches of industry (metallurgy, mining, sugar industry) are shown in [4-6].

In the industry, wide span multi-motor drives, used for the transportation of goods and materials, are often encountered. Structurally, these drives consist of two movable legs connected by a bridge, which as a whole form a gantry [3,6,7]. In the case of drives with a wide span, a very common practical problem is the occurrence of construction skewing. The most common causes of skewing are the geometrical imperfection of the construction, elasticity of construction, skidding of one side in relation to the other, uneven loading of individual sides due to the position of the load, as well as the influence of wind on drives located outdoors [7]. The impermissibly large skewing can result in the damage to the construction, and in the worst case, its destruction [8]. Bearing in mind the above, the fundamental technical requirement for a controlled multi-motor drive with a wide span is the synchronous movement of both sides. Accordingly, finding a practical solution that solves the skew control problem in a simple manner is very significant.

Skew control analysis, although of great importance for the operation of controlled multi-motor drives with a wide span, is not sufficiently represented in the literature. The skewing problem of cranes, primarily from the standpoint of mechanical construction, but also control, is analyzed in [7]. The specific problem of container skewing in container cranes has been analyzed in [9,10]. The author of this paper has considered the construction skewing problem of rail mounted wide span multi-motor drives in [6,8,11-13].

In this paper, in Section 2, a new skew control algorithm for rail mounted wide span multi-motor drive is proposed. Additionally, the design of the skew controller is analyzed in detail. In the appropriate hardware environment typical for controlled multi-motor drives, which implies the application of frequency converters and PLC systems interconnected by one of the industrial communication networks, the implementation of the proposed skew control algorithm is simple with a minimal hardware upgrade. The necessary additional hardware consists of two absolute encoders and two inductive proximity switches with appropriate markers, the number of which is determined by calculation. By designing the skew controller as described and verifying it experimentally, desired drive performances can be achieved. In Section 3 of this paper, the PLC program algorithm for the practical implementation of the proposed skew control algorithm is presented in detail. The practical implementation of skew control in the industry, on the gantry crane installed at a sugar beet open storage in the TE-TO Senta sugar factory, is presented in Section 4. Upon commissioning the gantry crane, time dependencies of characteristic quantities were recorded to determine the performance of the described skew control algorithm. These dependencies were recorded in a similar manner to that described in [14]. Characteristic results are shown in Section 5.

2. SKEW CONTROL

The principle block diagram for the skew control between two induction motors (IM_i and IM_k) supplied by frequency converters (FC_i and FC_k) is shown in Fig. 1. Given that the two movable legs are connected by a bridge which represents an elastic connection, the motors are not rigidly coupled.

Elastically coupled induction motors drive the wide span construction and they are speed-controlled by the appropriate frequency converters. The frequency converters operate in the

speed mode, utilizing their own speed controllers. Depending on the required drive performance, the motor speed, n_i and n_k, can be estimated or measured using appropriate encoders. The controlled multi-motor drive is speed-controlled and the main speed reference is n^*.
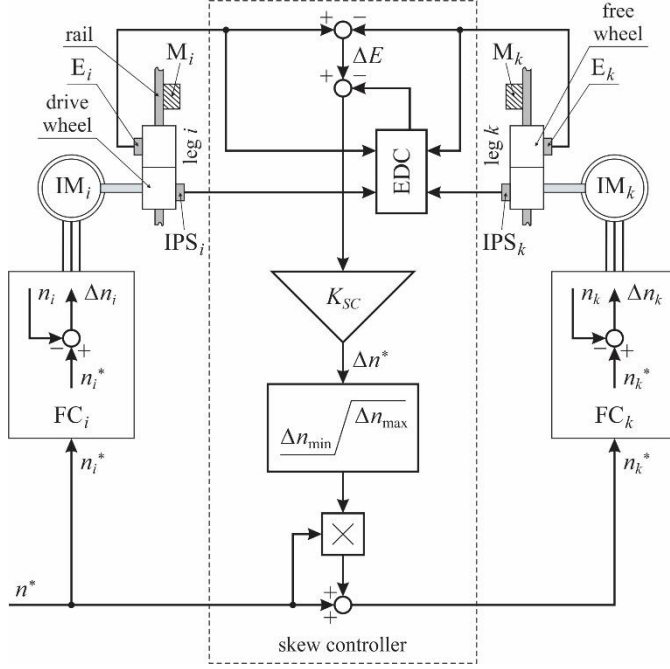
Fig. 1 The principle block diagram for skew control

Skew control between two movable legs connected by a bridge is realized by a skew controller, which is designed in the PLC system and it is a superior controller to the speed controller of the follower (slave) frequency converter, FC_k. Since high performance is not required from the PLC system, it is possible to use the existing PLC for the drive control. The operation principle of the skew controller is based on the fact that the motor driving the leg which lags by position needs to accelerate to reduce the lagging, while the motor driving the leg which leads by position needs to decelerate to reduce leading. In this way, the skew is reduced.

In the skew control algorithm, whose principle block diagram is shown in Fig. 1, the desired speed reference for one frequency converter (FC_i) is set to the main speed reference, $n_i^*=n^*$. For the second frequency converter (FC_k), the desired speed reference is obtained after correction of the main speed reference by the skew controller, $n_k^*=n^*+\Delta n^* \cdot n^*$. The reference correction, Δn^*, is proportional to the algebraic difference of absolute encoder positions, $\Delta E=E_i-E_k$, corrected by the external disturbances compensator, EDC. The reference correction is calculated in relative units, and the conversion to absolute units is achieved by multiplying by the main speed reference, $\Delta n^* \cdot n^*$. The proportional gain of the skew controller, K_{SC}, can be calculated by:

$$K_{SC} = \frac{\Delta n_d^*}{\Delta E_g} \;, \tag{1}$$

where Δn_d^* is the desired reference correction for the given encoder positions difference ΔE_g.

To ensure the stable drive operation under large external disturbances, it is desirable to limit the reference correction, Δn^*, by a limiter within the range of $\Delta n_{min} \div \Delta n_{max}$.

The encoder positions difference, ΔE, can deviate from the actual skew value for several reasons, such as differences in wheel circumferences where encoders are mounted, slippage of those wheels, differences in clearances of gearboxes, etc. The external disturbances compensator, EDC, takes into account and compensates all external influences on the position difference of two encoders by measuring the actual skew when inductive proximity switches, IPS_i and IPS_k, are above markers, M_i and M_k, symmetrically mounted along the construction runway. The slippage of drive wheels, as the biggest external disturbance, can be eliminated by mounting encoders on free wheels, as shown in Fig. 1.

The operation principle of the external disturbances compensator is illustrated in Fig. 2.
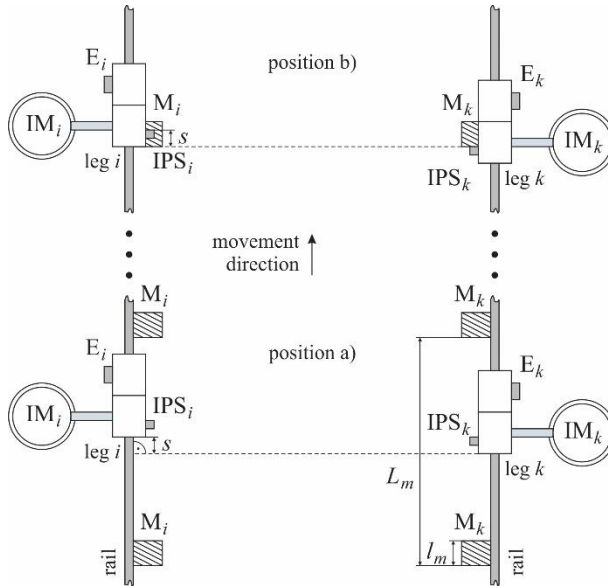
Fig. 2 The operation principle illustration of the external disturbances compensator

Position a) in Fig. 2 illustrates the controlled multi-motor drive with a wide span whose construction is skewed by the value s. The skew value represents the distance between the construction reference point on the motor side IM_i and the normal to the movement direction drawn from the construction reference point on the motor side IM_k.

Position b) in Fig. 2 illustrates the operation principle of the external disturbances compensator. The actual skew of the construction, s, is measured by encoders, and it is the distance travelled by the first activated inductive proximity switch over the associated marker until the activation moment of the second inductive proximity switch. The output from the external disturbances compensator, i.e. the compensation value, is the difference

between the difference of absolute encoder positions and the actual skew, $EDC = \Delta E - s$, and it corresponds to the influence of external disturbances on the construction skewing. In this way, with each passage over the markers, the influence of all external disturbances, accumulated between two pairs of markers, is eliminated.

For each wide span construction, the value of critical skew, s_{cr}, which can compromise its stability, is known. The skew controller is designed according to the allowable maximum skew, s_{max}, which must be less than the critical skew, $s_{max} < s_{cr}$. Depending on the technical requirements, the value of the allowable maximum skew in practice should be chosen from the range of $(0.4 \div 0.8)\, s_{cr}$.

The length of all markers along the runway should be the same and equal to the allowable maximum skew, $l_m = s_{max}$, to enable the skew control in the manner explained in Section 3.

The distance between each pair of markers along the runway, L_m, must be such that, during the movement of the drive between markers, external influences on the position difference of two encoders cause the construction skewing less than the allowable maximum skew. Let the drive move at a constant linear speed v. The distance between the markers will be covered in time:

$$t_m = \frac{L_m}{v} .$$ (2)

Also, let us assume that during the movement of the drive, due to external disturbances (such as differences in wheel circumferences where encoders are mounted, slippage of those wheels, differences in clearances of gearboxes, etc.), the maximum expected difference between linear speeds of leg i and leg k of the drive is Δv. To ensure that during the movement of the drive between markers external influences on the position difference of two encoders cause construction skewing less than the allowable maximum skew, the following must be met:

$$t_m \leq \frac{s_{max}}{\Delta v} .$$ (3)

The distance between each pair of markers, based on equations 2 and 3, is:

$$L_m \leq \frac{s_{max}}{\Delta v / v} .$$ (4)

Finally, the expression for calculating the distance between each pair of markers, L_m, can be written as follows:

$$L_m \leq \frac{s_{max}}{\Delta v_\%} \cdot 100\% ,$$ (5)

where $\Delta v_\%$ is the maximum expected difference between linear speeds of the leg i and leg k of the drive, expressed in percentages.

The number of marker pairs, N_m, for a runway of the length L, can be calculated using the following expression:

$$N_m \geq \frac{L}{L_m} .$$ (6)

In practice, the maximum expected difference between linear speeds of the leg i and leg k of the drive, $\Delta v_\%$, is a few percent at most. When adopting this value, one should consider the fact that a higher value increases safety, but it also increases the number of markers, so a compromise solution needs to be found.

To ensure stable drive operation under large external disturbances, it is desirable to limit the reference correction, Δn^*, by a limiter within the range of $\Delta n_{min} \div \Delta n_{max}$, where $\Delta n_{min} = -\Delta n_{max}$. Limiter saturation values should be adopted assuming irregular operation of the skew control (e.g., failure of one encoder), with the condition that the allowable maximum skew, s_{max}, is reached within the desired time, t_d. In the case of irregular operation of the skew control, the worst-case scenario is when the limiter operates at its saturation value, e.g. Δn_{max}. Then there is the maximum difference between linear speeds of leg i and leg k of the drive, Δv_{max}, which amounts to:

$$\Delta v_{max} = \Delta n_{max} \cdot \frac{1}{I_{dw}} \cdot \frac{\pi}{60} \cdot D_{dw} \ ,$$ (7)

where I_{dw} is the drive wheel gearbox ratio, and D_{dw} is the drive wheel diameter.
Under the above conditions, the following applies:

$$\Delta v_{max} = \frac{s_{max}}{t_d} \ .$$ (8)

The limiter saturation value, based on equations 7 and 8, is:

$$\Delta n_{max} = I_{dw} \cdot \frac{60}{\pi \cdot D_{dw}} \cdot \frac{s_{max}}{t_d} \ .$$ (9)

Finally, the expression for calculating the limiter saturation value, Δn_{max}, in percentages of the drive maximum main speed reference, n_{max}^*, can be written as follows:

$$\Delta n_{max,\%} = \frac{1}{n_{max}^*} \cdot I_{dw} \cdot \frac{60}{\pi \cdot D_{dw}} \cdot \frac{s_{max}}{t_d} \cdot 100\% \ .$$ (10)

The desired time, t_d, is adopted depending on the required drive performance. It should be noted that a smaller value provides a wider limiter range and faster skew controller response, but it can cause control instability. The typical limiter saturation value is in the range of $(5 \div 15)$ %.

If it is adopted that the desired reference correction is equal to the limiter saturation value in relative units, $\Delta n_d^* = \Delta n_{max,\%} / 100\%$, for the given encoder positions difference corresponding to the encoder position increment for the distance travelled in the length of the allowable maximum skew, $\Delta E_g = E_{p,max}$, the proportional gain of the skew controller, K_{SC}, can be calculated using the expression:

$$K_{SC} = \frac{\Delta n_{max,\%}}{E_{p,max}} \cdot \frac{1}{100\%} \ .$$ (11)

The encoder position increment for the distance travelled in the length of the allowable maximum skew, $E_{p,max}$, is:

$$E_{p,\max} = E_{p,1m} \cdot s_{\max} \ , \tag{12}$$

where $E_{p,1m}$ is the encoder position increment per meter of travel.

The encoder position increment per meter of travel, $E_{p,1m}$, can be calculated as follows:

$$E_{p,1m} = E_{p,rev} \cdot I_{fw} \cdot \frac{1}{\pi \cdot D_{fw}} \ , \tag{13}$$

where $E_{p,rev}$ is the encoder position increment per revolution, I_{fw} is the free wheel gearbox ratio, and D_{fw} is the free wheel diameter.

Finally, for the proportional gain of the skew controller, K_{SC}, by substituting expressions 10, 12, and 13 into expression 11, is obtained:

$$K_{SC} = \frac{1}{n_{\max}^*} \cdot \frac{I_{dw}}{I_{fw}} \cdot \frac{D_{fw}}{D_{dw}} \cdot \frac{60}{t_d} \cdot \frac{1}{E_{p,rev}} \ . \tag{14}$$

The designed skew controller should be experimentally verified upon commissioning the drive, and that in accordance with the desired performance.

In the appropriate hardware environment typical for controlled multi-motor drives, which implies the application of frequency converters and PLC systems interconnected by one of the industrial communication networks, the implementation of the proposed skew control algorithm is simple with minimal hardware upgrade. The necessary additional hardware consists of two absolute encoders and two inductive proximity switches with appropriate markers, the number of which is determined by calculation. By designing the skew controller as described and verifying it experimentally, desired drive performances can be achieved.

3. PLC PROGRAM ALGORITHM FOR SKEW CONTROLLER

Skew control is realized by the skew controller, which is designed in the PLC system by writing the appropriate program code. The PLC program algorithm for the proposed skew controller from Fig. 1 is shown in Fig. 3.

In the "skew check (M)" block, shown in Fig. 4, the fact that the length of all markers along the runway is the same and equal to the allowable maximum skew, $l_m = s_{\max}$, is utilized. Based on information from inductive proximity switches obtained when passing over the markers, this block checks the skew. If the skew exceeds the length of the markers, it sends a signal to stop the drive operation. Skew control by this block is independent of encoder functionality and any external disturbances, and it is active when the drive passes over the markers.

The "position difference (M)" block, whose PLC program algorithm is shown in Fig. 5, measures the difference in positions of the leg i and leg k of the drive, i.e. the actual skew of construction, s, as the difference of absolute encoder positions at the moment of inductive proximity switches activation upon passing over the markers. The actual skew of the construction, s, is taken into account when the inductive proximity switches become inactive, i.e. when the drive passes over the markers.
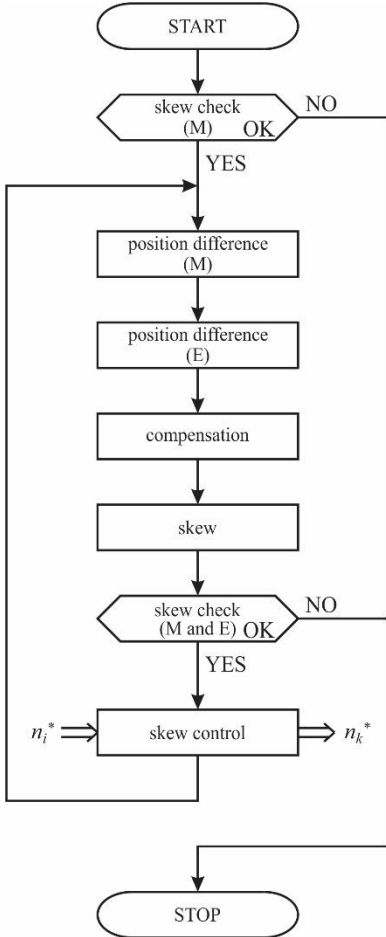
Fig. 3 The PLC program algorithm for the proposed skew controller
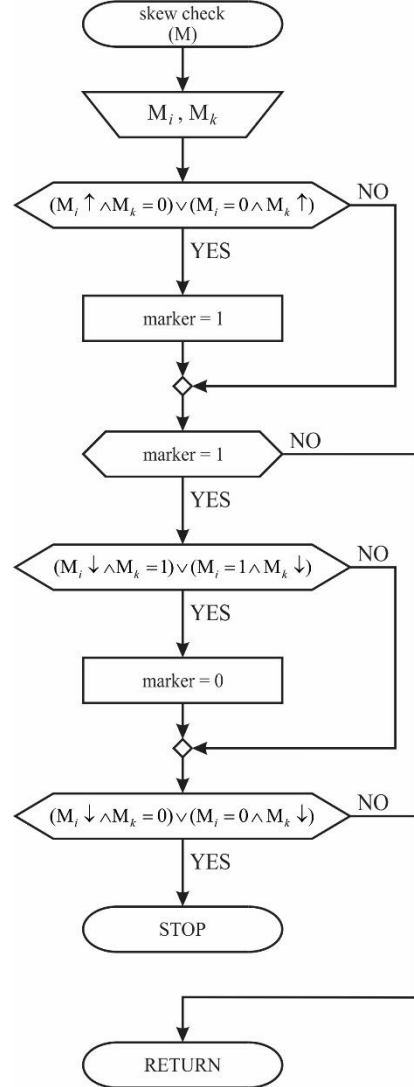
Fig. 4 The PLC program algorithm for the "skew check (M)" block

The "position difference (E)" block, shown in Fig. 6, measures the difference between the absolute positions of two encoders, ΔE, mounted on the free wheels of the leg i and leg k of the drive, in each processor cycle.

The "compensation" block, whose PLC program algorithm is shown in Fig. 7, calculates the compensation value as the difference between the difference of absolute encoder positions and the actual skew, $EDC=\Delta E-s$. Compensation, EDC, is calculated when the inductive proximity switches become inactive, i.e. when the drive passes over the markers.
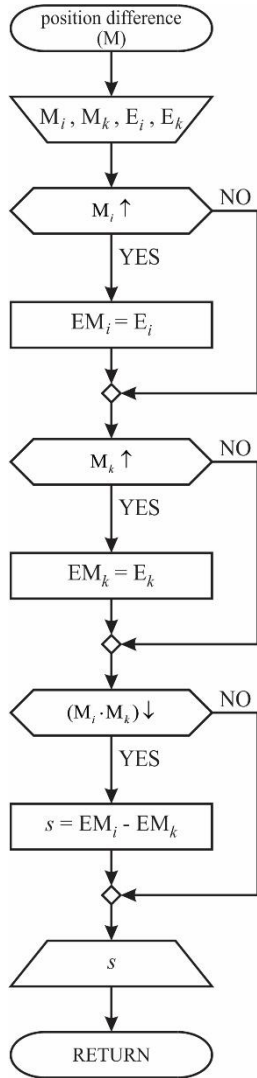
Fig. 5 The PLC program algorithm for the "position difference (M)" block
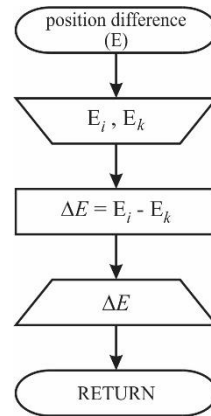
Fig. 6 The PLC program algorithm for the "position difference (E)" block

The "skew" block, shown in Fig. 8, calculates the skew value as the difference between the difference of absolute positions of two encoders and the compensation, $s_{calc} = \Delta E - EDC$, in each processor cycle. The calculated skew value is equal to the actual skew, $s_{calc} = s$, when the drive passes over the markers, i.e. when the compensation is performed. Between two compensation calculations, the calculated skew value may deviate from the actual skew due to the influence of external disturbances.

The "skew check (M and E)" block, shown in Fig. 9, checks the skew by comparing the calculated skew value with the allowable maximum skew in each processor cycle. If the calculated skew exceeds the allowable maximum skew, $s_{calc} > s_{max}$, the block sends a signal to stop the drive operation.
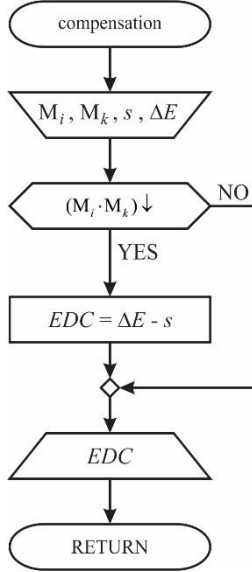
Fig. 7 The PLC program algorithm for the "compensation" block
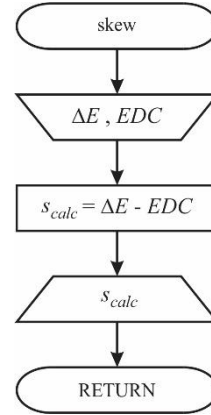
Fig. 8 The PLC program algorithm for the "skew" block

The PLC program algorithm for the "skew control" block is shown in Fig. 10. This block ensures the skew control by calculating the speed reference for one frequency converter, n_k^*, in each processor cycle. The calculation is based on the speed reference of the second frequency converter, n_i^*, and the calculated skew value, s_{calc}. The reference correction, $\Delta n^* = s_{calc} \cdot K_{SC}$, is limited by the limiter within the range of $\Delta n_{min} \div \Delta n_{max}$ to ensure stable drive operation under large external disturbances. The calculated speed reference in absolute units is $n_k^* = n_i^* + \Delta n^* \cdot n_i^*$.

The proposed PLC program algorithm for the skew control is primarily intended to control the skew in rail mounted wide span multi-motor drives. Additionally, the proposed algorithm also checks skew in two independent ways. This ensures the safe operation of wide span multi-motor drives, alongside designing the skew controller as previously described.

4. PRACTICAL IMPLEMENTATION

The proposed skew control algorithm has been implemented in the industry on the gantry crane installed at a sugar beet open storage in the TE-TO Senta sugar factory. Skew control is implemented for the gantry motion drive, whose main structural elements are shown in Fig. 11.
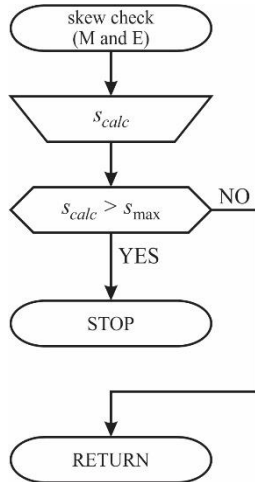
Fig. 9 The PLC program algorithm for the "skew check (M and E)" block
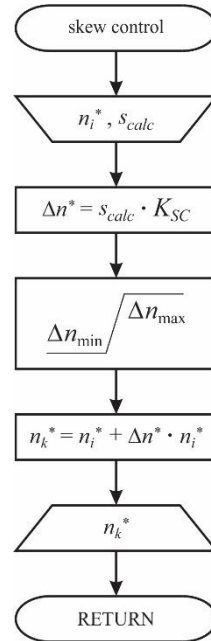
Fig. 10 The PLC program algorithm for the "skew control" block
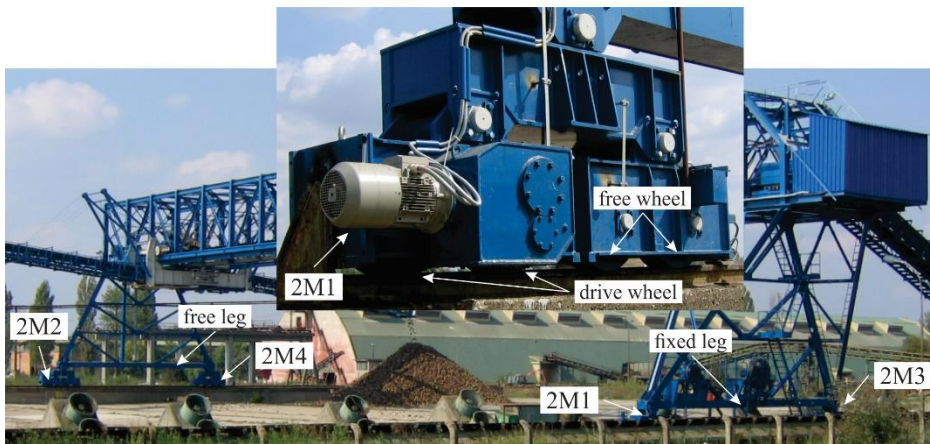
Fig. 11 The gantry motion drive – main structural elements

The gantry motion drive is a controlled multi-motor drive with four three-phase induction motors, 2M1 to 2M4, two per leg, supplied from frequency converters, 2U1 to 2U4, respectively. The operation of the gantry motion drive is controlled by the PLC system, which manages the entire gantry crane operation.

The structure of the gantry is lattice, to decrease the influence of wind. The distance between the fixed leg and the free leg of the gantry crane is 64.5 m. It is evident that this is the wide span construction where two movable legs are connected by a bridge which represents an elastic connection. The fundamental technical requirement for such a construction is the synchronous movement of both sides.

The induction motors 2M1 to 2M4 drive the common load, the gantry crane, and are speed-controlled by appropriate frequency converters. The frequency converters operate in the speed mode, utilizing their own speed controllers. Since high drive performance is not required, the motor speed is estimated.

The skew control between the fixed leg and the free leg of the gantry crane is realized by the skew controller between frequency converters 2U1 and 2U2. The speed reference for frequency converter 2U1 is set to the main speed reference, $n_{2U1}^*=n^*$. For frequency converter 2U2, the speed reference is obtained after the correction of the main speed reference by the skew controller, $n_{2U2}^*=n^*+\Delta n^* \cdot n^*$. In accordance with the theoretical analysis from Section 2, the reference correction, Δn^*, is proportional to the algebraic difference of absolute encoder positions, corrected by the external disturbances compensator, and limited within the set range. The external disturbances compensator takes into account and compensates all external influences on the position difference of two encoders by measuring the actual skew when inductive proximity switches are above markers, symmetrically mounted along the crane runway. The slippage of drive wheels, as the biggest external disturbance, is eliminated by mounting encoders on free wheels.

The following data about the gantry motion drive are known:
- three phase induction motors: 5.5 kW, 1455 rpm;
- transmission mechanism – drive wheel: I_{dw}=394.7368, D_{dw}=0.5 m;
- transmission mechanism – free wheel: I_{fw}=15.6466, D_{fw}=0.5 m;
- length of the crane runway: L=300 m;
- critical skew: s_{cr}=1 m;
- absolute encoders: multiturn, resolution 12 bits per revolution, 2^{12} revolutions.

For the chosen encoders, the position increment per revolution is $E_{p,rev}=2^{12}=4096$. The encoder position increment per meter of travel, calculated using expression 13, has a value of $E_{p,1m}=40800$. The maximum encoder position increment is $(2^{12} \cdot 2^{12})-1=16777215$, meaning the encoder can map the travelled distance of 411.2064 m. Considering the length of the crane runway to be mapped and an appropriate degree of security, it is clear that two absolute encoders have been well chosen.

In accordance with the theoretical analysis from Section 2, and considering the critical skew value, the allowable maximum skew of s_{max}=0.5 m was adopted. Also, in line with the theoretical analysis from Sections 2 and 3, the length of all markers along the crane runway is the same and equal to the allowable maximum skew, $l_m=s_{max}$=0.5 m.

For the adopted value of the maximum expected difference between linear speeds of the fixed leg and the free leg of the gantry crane $\Delta v_\%$=1 %, the distance between each pair of markers, based on expression 5, should satisfy the condition $L_m \leq 50$ m. Also, the number of marker pairs, according to expression 6, should meet the condition $N_m \geq 6$. Considering the obtained values, 6 marker pairs along the crane runway have been adopted, mounted at a maximum distance of 50 m.

The adopted value of the desired time to reach the allowable maximum skew, assuming irregular skew control operation (e.g. failure of one encoder), is t_d=60 s. Also, considering

the nominal motor speed, the adopted drive maximum main speed reference has a value of n_{max}^*=1455 rpm. Now, the saturation value of the skew controller limiter in percentages of the drive maximum main speed reference, based on equation 10, is $\Delta n_{max,\%}$=8.6356 %.

The proportional gain of the skew controller, calculated using expression 14, has a value of K_{SC}=1/236230.

Based on the calculated values for the proportional gain of the skew controller and for the saturation value of the skew controller limiter, the following values have been adopted: K_{SC}=1/236230 and $\Delta n_{max,\%}$=10 %. Now, the limiter setting is $\pm$ 10 %. The designed skew controller was experimentally verified upon commissioning the drive.

5. EXPERIMENTAL RESULTS

Upon commissioning the gantry crane installed at a sugar beet open storage in the TE-TO Senta sugar factory, to determine the performance of the described skew control algorithm implemented in the gantry motion drive, time dependencies of characteristic quantities were recorded using frequency converters (ASC550 series) and PLC system (90 series, CPU 07 KT 98), utilizing the "907 AC 1131" software, all manufactured by ABB.

The time dependencies of motor speeds and the calculated skew value were recorded, with a sampling time of 20 ms. The PLC system retrieves motor speeds from the frequency converters via the PROFIBUS DP industrial communication network. Motor speeds are estimated quantities, expressed as integer values in [rpm]. The calculated skew value is computed in the PLC system and expressed as an integer value in [cm].

Characteristic time dependencies for the gantry motion drive, for the movement direction that is adopted as positive, are shown in Fig. 12 to Fig. 14.

The desired speed reference for frequency converter 2U1 is set to the main speed reference of the drive, n_{2U1}^*=n^*, and has a value of 1000 rpm. From Fig. 12, it can be concluded that the motor speed n_{2U1} "well" follows the speed reference, with a certain ripple that is a consequence of various external disturbances.

The time dependence of the calculated skew value, s_{calc}, is shown in Fig. 14. The gantry crane moved between two pairs of markers for some time, and the skew controller reduced the skew (s_{calc}) to a value of 0 cm. At the moment $t \approx 0.1$ s the inductive proximity switches become inactive, i.e. they passed over the markers. External disturbances compensation was performed. The calculated skew value is now equal to the actual skew and has a value of $s_{calc} = -2$ cm. The "minus" sign indicates that, relative to the direction of the gantry crane movement, the free leg lags behind the fixed leg.

So, while the gantry crane was moving between two pairs of markers, the skew controller reduced the skew (s_{calc}) to a value of 0 cm. However, due to various external influences on the position difference of two encoders, the calculated skew value differs from the actual skew by -2 cm. This difference is compensated when the inductive proximity switches pass over the markers ($t \approx 0.1$ s).

After the moment $t \approx 0.1$ s, to reduce the skew, for frequency converter 2U2, the speed reference is obtained after correction of the main speed reference, n^*=n_{2U1}^*, by the skew controller, n_{2U2}^*=n^*+$\Delta n^* \cdot n^*$. Considering that the free leg lags behind the fixed leg, it should hold true that $n_{2U2}^* > n_{2U1}^*$. By analyzing Fig. 13, it is clear that the motor speeds difference n_{2U1}-n_{2U2} varies within the range of about -22 rpm to 10 rpm, with the mean value certainly being less than zero, consistent with the previous conclusion.
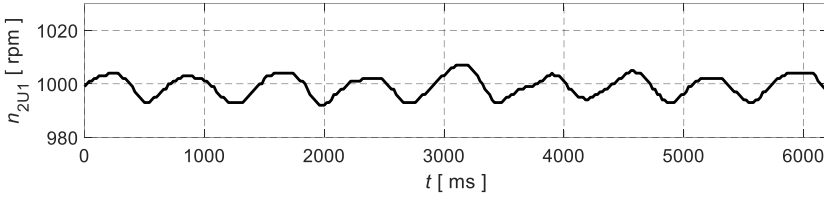
Fig. 12 The motor speed of 2M1, n_{2U1}

Fig. 13 Motor speeds difference between 2M1 and 2M2, n_{2U1}-n_{2U2}
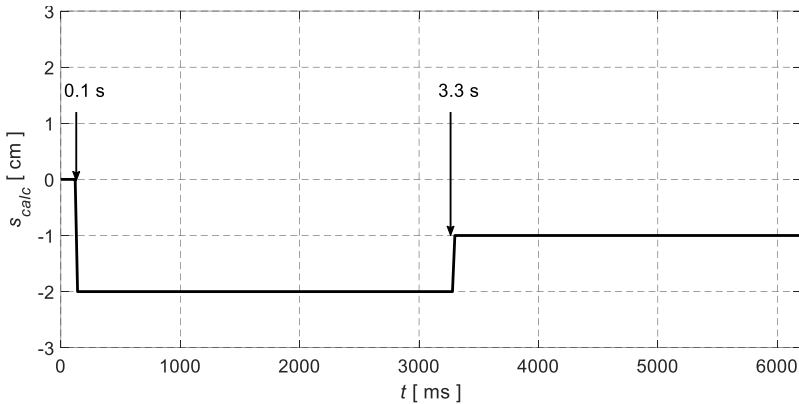
Fig. 14 The calculated skew value, s_{calc}

As a consequence of the skew controller operation, at the moment $t \approx 3.3$ s the skew decreases, and the calculated skew value is $s_{calc} = -1$ cm. Considering that the free leg lags behind the fixed leg, it should hold true that $n_{2U2}^{*} > n_{2U1}^{*}$. By analyzing Fig. 13, it is clear that the motor speeds difference n_{2U1}-n_{2U2} varies within the range of about -16 rpm to 2 rpm, with the mean value certainly being less than zero, consistent with the previous conclusion.
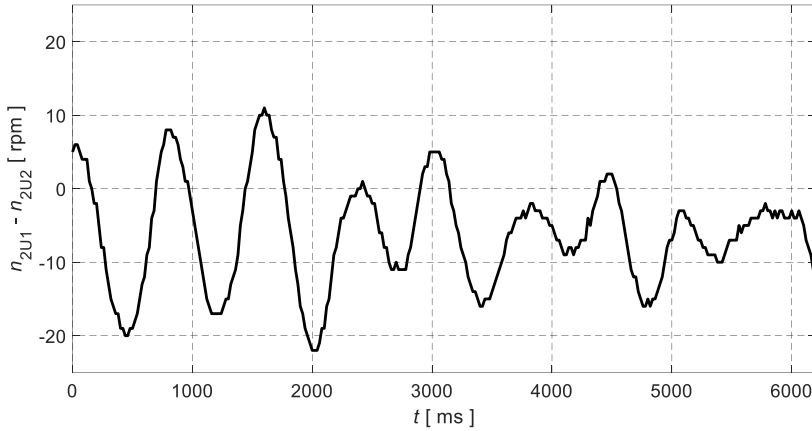
If the gantry crane continues to move, as a consequence of the skew controller operation, the skew will continue to decrease, and the calculated skew value will reach the value of

$s_{calc} = 0$ cm. Due to the limited number of points in recording the time dependencies, that moment is not shown in Fig. 12 to Fig. 14.

Based on the presented analysis, it can be concluded that during the operation of the gantry motion drive, the calculated skew value changes within narrow limits, far less than the allowable maximum skew. Additionally, it is clear that as a consequence of the skew controller operation, the calculated skew value decreases. Since the calculated skew value may differ from the actual skew due to various external influences on the position difference of two encoders, special attention is paid to analyzing the operation of the external disturbances compensator. It is clear that when the inductive proximity switches pass over the markers, all external disturbances compensation is realized. Due to various external disturbances, and as a consequence of the skew controller operation, a difference in motor speeds occurs, which is limited by the limiter to ensure stable drive operation.

Considering the above, as well as the experimental results shown in Fig. 12 to Fig. 14, the conclusion is that the implementation of the skew control algorithm in the gantry motion drive is necessary, and that the proposed algorithm, whose principle block diagram is shown in Fig. 1, has satisfactory performance.

6. CONCLUSION

In this paper, a simple and practical method for skew control of rail mounted wide span multi-motor drives is proposed. The design of the skew controller is analyzed in detail, and the PLC program algorithm for the practical implementation of the proposed solution is presented. This innovative skew control algorithm is suitable for implementation in existing drives. In the appropriate hardware environment typical for controlled multi-motor drives, which implies the application of frequency converters and PLC systems interconnected by one of the industrial communication networks, the implementation of the proposed skew control algorithm is simple with minimal hardware upgrade. The necessary additional hardware consists of two absolute encoders and two inductive proximity switches with appropriate markers, the number of which is determined by calculation.

An unavoidable requirement in forming the skew control algorithm is maintaining safety and functionality in specific situations, such as the failure of key components, occurrences of wear, skidding of one side in relation to the other, uneven loading of individual sides due to the position of the load, and the influence of wind on drives located outdoors. For this reason, the external disturbances compensator is formed as a separate structure in the control algorithm. This compensator, based on the additional system of markers, corrects potential skew calculation errors and ensures the reliable operation of the skew controller. By designing the skew controller as described and verifying it experimentally, desired drive performances can be achieved.

Additionally, the practical implementation of the proposed skew control algorithm in the industry, on the gantry crane installed at a sugar beet open storage in the TE-TO Senta sugar factory, is presented. Upon commissioning the gantry crane, time dependencies of characteristic quantities were recorded in order to determine the performance of the described solution. In this paper, part of the detailed performance analysis results is shown, which confirmed good control characteristics.

REFERENCES

[1] Borislav Jeftenić, Milan Bebić, Saša Štatkić, "Controlled multi-motor drives", *International Symposium on Power Electronics, Electrical Drives, Automation and Motion, SPEEDAM 2006*, Taormina, Italy, 23-26 May 2006, ISBN: 1-4244-0193-3 (Print), pp. 1392-1398, doi: 10.1109/SPEEDAM.2006.1649985.

[2] Francisco J. Perez-Pinal, Ciro Nunez, Ricardo Alvarez, Ilse Cervantes, "Comparison of multi-motor synchronization techniques", *The 30th Annual Conference of IEEE Industrial Electronics Society, IECON 2004*, Busan, Korea (South), 2-6 November 2004, vol. 2, pp. 1670-1675. doi: 10.1109/IECON.2004.1431832.

[3] Keum-Shik Hong, Umer Hameed Shah, "Dynamics and control of industrial cranes", Advances in Industrial Control, Springer, ISSN 1430-9491, 2019.

[4] A. K. Paul, I. Banerjee, B. K. Snatra, N. Neogi, "Application of AC motors and drives in steel industries", *Fifteenth Natinal Power System Conference (NPSC)*, IIT Bombay, December 2008, pp. 159-163.

[5] Vojkan Kostić, Nebojša Mitrović, Bojan Banković, Filip Filipović, Milutin Petronijević, "Optimal design and control of multi-motor drive system for industrial application", *The Journal Tehnički vjesnik – Technical Gazette (TV-TG)*, December 2020, ISSN 1330-3651 (Print), ISSN 1848-6339 (Online), vol. 27, no. 6, pp. 1815-1824. doi: https://doi.org/10.17559/TV-20180509152814.

[6] Nebojsa Mitrovic, Milutin Petronijevic, Vojkan Kostic and Borislav Jeftenic, "Electrical drives for crane application", InTech, Mechanical Engineering, Murat Gokcek (Ed.), April 2012, ISBN: 978-953-51-0505-3, pp. 131-156. doi: 10.5772/35560.

[7] J. Verschoof, "Cranes - design, practice and maintenance", 2nd Edition, Professional Engineering Publishing Limited, London, UK, 2002, ISBN 1 86058 373 3.

[8] Nebojša Mitrović, Vojkan Kostić, Milutin Petronijević, Borislav Jeftenić, "Practical implementation of load sharing and anti skew controllers for wide span gantry crane drives", *Strojniški vestnik – Journal of Mechanical Engineering*, 2010, ISSN 0039-2480, UDC 621.875.5, vol. 56, no. 3, pp. 207-216.

[9] G.E. Smid, J.B. Klaassens, H.R. van Nauta Lemke, A. El Azzouzi, R. van der Wekken, "Automatic skew control on container transhipment cranes", *IFAC Proceedings Volumes*, Elsevier, 2000, ISSN 1474-6670, vol. 33, issue 26, pp. 977-982. https://doi.org/10.1016/S1474-6670(17)39272-8.

[10] Quang Hieu Ngo, Keum-Shik Hong, Kyeong Han Kim, Yong Jeong Shin and Sang-Hei Choi, "Skew control of a container crane", *International Conference on Control, Automation and Systems*, Seoul, Korea (South), 2008, pp. 1490-1494. doi: 10.1109/ICCAS.2008.4694378.

[11] Nebojsa Mitrovic, Vojkan Kostic, Milutin Petronijevic, Borislav Jeftenic, "Multi-motor drives for crane application", *Advances in Electrical and Computer Engineering*, 2009, ISSN 1582-7445, e-ISSN 1844-7600, vol. 9, no. 3, pp. 57-62. doi: 10.4316/AECE.2009.03011.

[12] N. Mitrovic, V. Kostic, M. Petronijevic and B. Jeftenic, "Practical implementation of multi-motor drives for wide span gantry cranes", *Iranian Journal of Science & Technology, Transaction B: Engineering*, 2010, ISSN 1028-6284, vol. 34, no. B6, pp. 649-654.

[13] Nebojša Mitrović, Vojkan Kostić, Milutin Petronijević, Borislav Jeftenić, Bojan Banković, "Skew controller for rail mounted wide span gantry cranes", *15th International symposium on power electronics - Ee 2009*, Novi Sad, Republic of Serbia, October 28th - 30th, 2009, ISBN 978-86-7892-208-4, paper no. T2-1.3, pp. 1-4.

[14] Igor Kocić, Saša S. Nikolić, Darko Mitić, Petar Đekić, Nikola Danković, Nebojša Jotović, "Data collection tool for process identification using PLC and Kepware tools", *FACTA UNIVERSITATIS Series: Automatic Control and Robotics*, vol. 21, no. 3, 2022, pp. 177–186. https://doi.org/10.22190/FUACR221118014K.

ADAPTIVE COMPLEX FILTERS BASED TRANSMITTER IQ IMBALANCE REJECTION

UDC (621.394.618)

Borisav Jovanović[1], Srđan Milenković[2]

[1]University of Niš, Faculty of Electronic Engineering, Department of Electronics, Republic of Serbia
[2]Lime Microsystems, Surrey Tech Centre, Occam Road, Guildford, Surrey, UK

ORCID iDs: Borisav Jovanović   https://orcid.org/0000-0002-4211-5426
         Srđan Milenković   N/A

Abstract. *This paper presents an efficient method for compensation of frequency-dependent (FD) transmitter In-phase Quadrature (IQ) imbalance. Proposed method compensates imbalance by exploiting indirect learning architecture (ILA) and complex filters whose coefficients are determined in an iterative process. Compensation performance is assessed after the method has been implemented in a Software Defined Radio (SDR) platform, capable of transmitting modulations at different central frequencies. Measured results demonstrate that the imbalance related images are reduced down to the noise floor. After applying the proposed IQ imbalance correction method, the transmitter image rejection ratio (IRR) is increased by 15dB in the case of an SDR transmitter operating at central frequency of 1.7 GHz. The ADC/DAC sampling rate is 61.44MS/s, while the signal bandwidth, for which the compensation is performed, is 30.72MHz. The advantage of the proposed method is low complexity in terms of a reduced number of coefficients. The method is generic and can be utilized for IQ imbalance compensation when wideband signals are transmitted.*

Key words: *In-phase, quadrature imbalance, complex filters, indirect learning architecture, digital predistortion.*

1. INTRODUCTION

Identification of nonlinear systems with memory effects is one of the challenging topics in wireless communications. The Orthogonal Frequency Division Multiplexing

(OFDM) systems have been widely used in many communication standards achieving high data rates and spectral efficiency [1]. However, performance of OFDM systems is significantly degraded in a presence of power amplifier (PA) nonlinearities and its memory effects. The degradation is caused by signal multi-carrier nature which introduces high peak-to-average power (PAPR) ratios and inter-modulation product terms. The resulting in-band interference severely degrades the signal quality. In addition, PA nonlinearity introduces out-of-band interference producing spectral regrowth [2].

Digital pre-distortion (DPD) is an efficient method that improves performance and energy efficiency of wireless infrastructure, compensating various transmitter imperfections [2]. DPD is basically used for compensation of PA distortions which arise due to the nonlinear PA transfer characteristics. DPD is implemented in the base-band (BB), before the digital-to-analogue (DA) conversions and BB to radio-frequency (RF) frequency up-conversions are performed. Other imperfections which can be compensated by DPD include transmitter in-phase and quadrature (IQ) imbalance and the crosstalk which exist between different channels in multi-input multi-output (MIMO) systems [3].

The IQ imbalance (IQI) occurs when the phase or amplitude of I and Q signal components are not perfectly matched. The impact of IQI on signal quality can be harmful, leading to the spectral regrowth, increased error rates and reduced system performance. This paper presents an efficient frequency-dependent (FD) IQI compensation method dedicated for usage in software-defined radio (SDR) transceivers. The compensation method is implemented in the BB using complex finite impulse response (FIR) filters whose coefficients are determined in an iterative process. The advantage of proposed method is that the IQI compensation is performed during the transmitter operation. Another advantage is low complexity in terms of reduced number of complex valued coefficients. Steps for efficient imbalance mitigation are thoroughly described, starting from a mathematical model to complete realization in SDR.

This paper is organized as follows. Related work is given in the following section. In the Section 3 the IQI mitigation method is described. In Section 4, the simulation setup is presented, followed by simulation results. The measured results are presented in Section 5. Section 6 is dedicated to discussion. The conclusion is drawn in the last section.

2. RELATED WORK

The IQI of RF transceivers is caused by various sources, such as the mismatches in the components of the transmitter chain, imperfections in the analog circuits including the analogue low-pass filters (LPF), phase and gain mismatches in mixers or limitations in the analogue-to-digital (ADC) and digital-to-analogue converters (DAC) [4].

Various techniques are employed for compensation of the IQ imbalance in wideband transmitters which can be generally divided in calibration and adaptive techniques.

Calibration methods are based on the measurement of actual imbalances in the hardware and applying digital correction schemes to compensate for these imbalances [5], [6]. Calibration techniques rely on utilization on test signals and their operations are performed at transceiver start-up [5]. Adaptive compensation techniques neutralize imbalance during transceiver operation [6].

The Refs [5]-[7] investigate the mismatches between LPFs of transmitter I and Q signal paths as a source of the FD IQI. In order to equalize the LPF frequency responses, a feedback path, consisting of additional ADC, is used to bring back the transmitter

output signal to the BB for imbalance detection [5], [6]. The imbalance is compensated using digital filters [5], [7]. In Ref. [5] the single-tone signals are used as the test signals. The least squares (LS) optimization method is employed to minimize the error that exists between the desired filter response and the measured one. In Refs. [8], [9] the transmitter impairments are reduced using complex-valued FIR filters. The coefficients are calculated in an iterative process which is based on the LS method.

DPD is often employed for the FD IQI mitigation [10]. Many publications combine the IQI compensation with PA linearization. Such publications extend the parallel Hammerstein structure [11], Volterra series model [12] and asymmetrical complexity-reduced Volterra series model [13]. Impairments are cancelled using the complex-valued filters. The filter coefficients are determined in an adaptive process that utilizes monitoring path in form of additional receiver [11]-[13]. Although efficient, methods suffer from an increase in computational complexity compared to an independent IQI compensation [14].

Most of the techniques which are found in the literature are implemented using laboratory equipment, in which modulation waveforms are created by software and vector signal generators (VSG).

In previous work [15] memory polynomial (MP) DPD is created that jointly compensates transmitter FD IQI, PA nonlinearity and PA memory effects. The disadvantage of MP DPD is limited signal bandwidth, because DAC/ADC sampling frequency should be at least five times greater than signal bandwidth. For ADC/DAC sample rate of 61.44MS/s, the maximum signal bandwidth of 20MHz is achieved [15]. In the Ref. [16] both transmitter and receiver IQI are calibrated in the same process. The method is developed for IQI compensation and wideband fifth generation new radio (5G NR) signals transmission. The maximum signal bandwidth of 100MHz is achieved at ADC/DAC sampling rate of 245.75MS/s [16]. The FD IQI is compensated by complex filters [17]. The IQI calibration method [16] does not use monitoring path and coefficient calculation process is not adaptive. The calibration procedure is executed only at transceiver power-up. The method [16] utilizes single tone test signals for IQI identification and calibration. During calibration process the digital modulator is stopped and numerically controlled oscillator (NCO) is employed for test signal generation [16].

Unlike the method described in [16], the proposed method is adaptive and utilizes a monitoring path for IQI identification. This implies that compensation is performed during the transceiver normal operation. The transmitter impairments are reduced using adaptive complex-valued FIR filters. The coefficients are calculated in an iterative process that is based on the recursive least squares (RLS) method. The method can be employed in the applications when wideband signals are transmitted.

3. IQ Imbalance Correction Method

The signal $x(n)$, consisting of quadrature components $x_I(n)$ and $x_Q(n)$, is modified by the IQ imbalance source into the signal $y(n)$, consisting of components $y_I(n)$ and $y_Q(n)$.

$$y_I(n) = x_I(n) \cdot G_I(\omega)\cos(\omega n + \varphi_I(\omega))$$
$$y_Q(n) = x_Q(n) \cdot G_Q(\omega)\sin(\omega n + \varphi_Q(\omega))$$

(1)

Amplitude response functions of I and Q channels are denoted by $G_I(\omega)$ and $G_Q(\omega)$, while corresponding channel phases are $\varphi_I(\omega)$ and $\varphi_Q(\omega)$. The IQ imbalance is defined by gain and phase imbalance functions, $\varepsilon_{err}(\omega)$ and $\varphi_{err}(\omega)$, which are defined by (2) and (3) [10]:

$$\varepsilon_{err}(\omega) = \frac{G_I(\omega)}{G_Q(\omega)} \tag{2}$$

$$\varphi_{err}(\omega) = \varphi_I(\omega) - \varphi_Q(\omega) \tag{3}$$

Transmitter IQI leads to the incomplete image signal rejection which is quantified by image rejection ratio (IRR) [10]:

$$IRR(\omega) = 10 \log \frac{1 + \varepsilon_{err}(\omega)^2 + 2\varepsilon_{err}(\omega)\cos(\varphi_{err}(\omega))}{1 + \varepsilon_{err}(\omega)^2 - 2\varepsilon_{err}(\omega)\cos(\varphi_{err}(\omega))} \tag{4}$$

The functions $\varepsilon_{err}(\omega)$ and $\varphi_{err}(\omega)$ are frequency dependent. The transmitter, which is composed of real valued circuits, has positive symmetrical $\varepsilon_{err}(\omega)$ around the DC and negative symmetrical $\varphi_{err}(\omega)$ [18]. In this case, the imbalance can be compensated using two real-valued FIR filters positioned in the BB, in separate I and Q signal paths. However, in RF, the transmitter symmetry may be degraded. It was proven that transmitters produce asymmetric $\varepsilon_{err}(\omega)$ and $\varphi_{err}(\omega)$ [9]. The utilization of valued digital filters is required for IQI compensation [9].

The generalized diagram of the circuit dedicated for wideband IQ imbalance correction is depicted in Fig. 1a). The correction scheme is based on utilization of a complex FIR filters, adopted from [9]. The IQ imbalance correction method utilizes an indirect learning architecture (ILA) which is comprised of two complex filters, denoted with predistorter and postdistorter, as depicted in Fig. 1a). The predistorter takes at input the complex-valued signal $xp(n)$, produced by a digital modulator. The real and imaginary parts of $xp(n)$ are denoted with $xp_I(n)$ and $xp_Q(n)$, respectively.
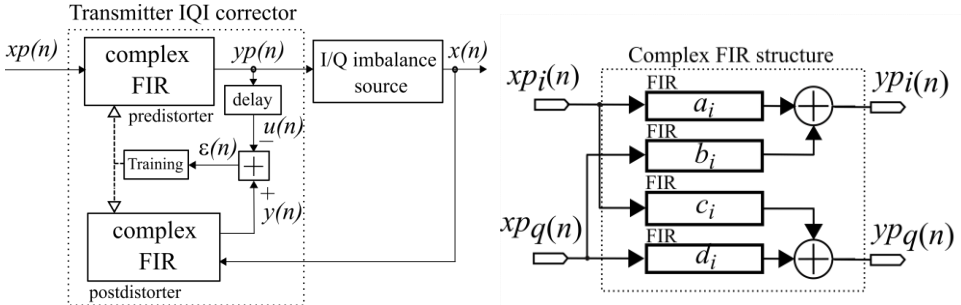

Fig. 1 a) Indirect learning architecture dedicated for IQI rejection b) complex FIR structure

The predistorter produces at output the signal $yp(n)$ consisting of $yp_I(n)$ and $yp_Q(n)$ components:

$$yp(n) = yp_I(n) + \mathbf{j} \cdot yp_Q(n) =$$

$$\sum_{i=0}^{N} (a_i \cdot xp_I(n-i) + b_i \cdot xp_Q(n-i)) + \mathbf{j} \sum_{i=0}^{N} (c_i \cdot xp_I(n-i) + d_i \cdot xp_Q(n-i)) \tag{5}$$

The parameter N represents the filter order, while a_i, b_i, c_i, d_i are FIR coefficients. Postdistorter is a simple copy of predistorter, both sharing the same set of coefficients.

$$y(n) = y_I(n) + \mathbf{j} \cdot y_Q(n) =$$

$$\sum_{i=0}^{N} (a_i \cdot x_I(n-i) + b_i \cdot x_Q(n-i)) + \mathbf{j} \sum_{i=0}^{N} (c_i \cdot x_I(n-i) + d_i \cdot x_Q(n-i)). \tag{6}$$

The block diagram of the complex FIR dedicated for IQ correction is depicted in Fig. 1b). The circuit is composed of four real valued FIR filters. Two real-valued FIRs are positioned in I and Q signal paths. The other two are located in the cross paths. The FIR filters have length N. The coefficients are calculated in an adaptive process using RLS algorithm. The RLS aims to minimize the sum of the squares of the difference between the predistorter and postdistorter outputs. The RLS cost function $K(n)$ is defined as:

$$K(n) = \sum_{m=0}^{n} \lambda^{n-m} ((u_I(m) - y_I(m))^2 + (u_Q(m) - y_Q(m))^2), \tag{7}$$

where $u_I(n)$ and $u_Q(n)$ are real and imaginary parts of the $yp(n)$, delayed by loop delay from predistorter output to the postdistorter output. The λ is the RLS "*forgetting factor*" [10]. In order to minimize $K(n)$, system of linear equations is formed by setting to zeros the partial derivatives of $K(n)$ in respect to a_i, b_i, c_i, d_i. To express system of equations in a matrix form, the coefficients a_i, b_i, c_i, d_i are stored in the vector $\mathbf{S}(n)$.

$$\mathbf{S}(n) = [s_i \quad s_{i+N+1} \quad s_{i+2(N+1)} \quad s_{i+3(N+1)}]_{4(N+1)}^{T}$$

$$= [a_i \quad b_i \quad c_i \quad d_i]_{4(N+1)}^{T}, \quad i = 0,...,N. \tag{8}$$

The signals $u_I(n)$ and $u_Q(n)$ are stored in the vector $\mathbf{u}(n)$:

$$\mathbf{u}(n) = [u_i]_{4(N+1)} = [u_I(n) \quad u_Q(n) \quad 0 \quad ... \quad 0]_{4(N+1)}. \tag{9}$$

The signals $x_I(n)$ and $x_Q(n)$ and its previous samples are stored the matrix $\mathbf{X}(n)$, which has dimension $4(N+1)\mathrm{x}4(N+1)$:

$$\mathbf{X}(n) = \begin{bmatrix} x_I(n-i)_{i,0} & x_Q(n-i)_{i,1} & 0 & ... & 0 \\ -x_Q(n-i)_{i+N+1,0} & x_I(n-i)_{i+N+1,1} & 0 & ... & 0 \\ x_I(n-i)_{i+2(N+1),0} & -x_Q(n-i)_{i+2(N+1),1} & 0 & ... & 0 \\ x_Q(n-i)_{i+3(N+1),0} & x_I(n-i)_{i+3(N+1),1} & 0 & ... & 0 \end{bmatrix}_{4(N+1) \times 4(N+1)} \tag{10}$$

Following the RLS algorithm, after every training step, the elements of matrix $\mathbf{A}(n)$ and vector $\mathbf{B}(n)$ are calculated according to (11) and (12). The matrices $\mathbf{A}(n)$ and $\mathbf{B}(n)$ have dimensions $4(N+1) \times 4(N+1)$ and $4(N+1) \times 1$, respectively.

$$\mathbf{A}(n) = \mathbf{X}(n) \times \mathbf{X}(n)^T + \lambda \cdot \mathbf{A}(n-1) \tag{11}$$

$$\mathbf{B}(n) = \mathbf{X}(n) \times \mathbf{u}(n)^T + \lambda \cdot \mathbf{B}(n-1) \tag{12}$$

The system of equations in matrix form is expressed by (13). The a_i, b_i, c_i and d_i are found by solving the (13).

$$\mathbf{A}(n) \times \mathbf{S}(n) = \mathbf{B}(n) , \tag{13}$$

4. SIMULATION OF IQ CORRECTION METHOD

The IQI corrector model has been implemented in SystemC [19], the set of C++ classes which can be used to system-level modeling [19]. The advantage of SystemC utilization is possibility to simulate the real-time environments, using datatypes offered by standard C++ and additional ones, defined in the SystemC libraries. The simulation setup is depicted in the Fig. 2. The figure presents the transmitter and receiver paths consisting of the digital modulator, predistorter, postdistorter, the IQ imbalance source, inverse SINC filter, ADC and DAC, modeled in SystemC.
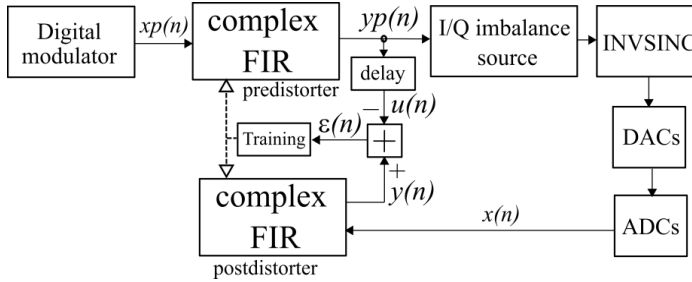
Fig. 2 Simulation setup for IQ imbalance rejection

As a test waveform the low intermediate frequency (low-IF) waveform is used. It consists of the sixteen single frequency tones. The waveform is generated at the rate of 61.44MS/s. The frequencies of successive tones are spaced by 0.96MHz, covering the frequency range from DC to the 15.36MHz.

The SystemC model of IQ corrector is designed based on (5). The order of complex filter is represented by parameter N. In every training step, new elements of matrices $\mathbf{A}(n)$ and $\mathbf{B}(n)$ are calculated according to (11) and (12). The coefficients are obtained after the system of equations (13) is solved. For this task the LU decomposition method is used. After the signal is processed by predistorter, the imbalance is inserted into signals (Fig. 2).

The IQI source is created based on measured data. For this purpose, the RF transceiver IC LMS7002M [20] is tuned to central frequency of 3.55GHz. Transmitter IQ gain and phase error values are determined for the BB frequencies in the range between -30.72MHz and 30.72MHz, with a step of 5MHz. The imbalance values are calculated and used as inputs of IQI source model. Derived gain and phase imbalance functions manifest FD behavior and they are depicted in Fig. 3a).
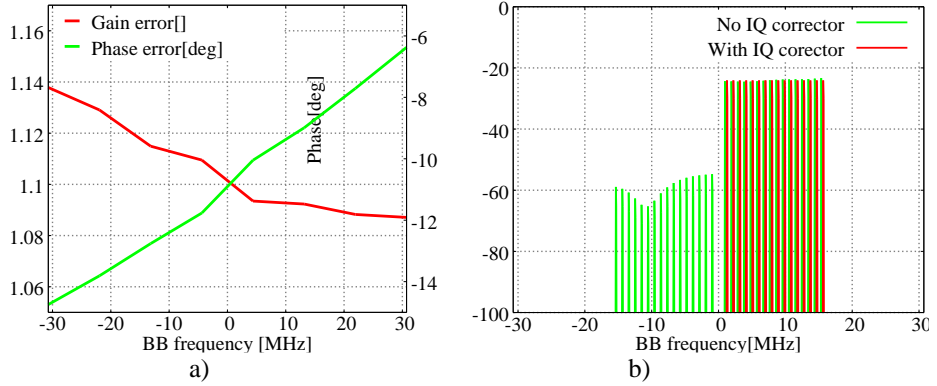
Fig. 3 a) Measured gain and phase errors of transmitter at 3.55GHz, b) Simulation results of transmitter output a) when correction is bypassed and b) when correction is applied.

The DAC roll-off is compensated by an inverse SINC filter. In simulations the arithmetical precision of 18 bits is adopted and the number of points for FFT is set to 2^{16}. The simulation results shows efficiency of the proposed method in image rejection. Fig. 3b) depicts the power spectral densities of transmitter output signal when corrector is bypassed and in the case when IQI correction method is applied. As it can be seen from Fig. 3b), imbalance produced tone signals are completely removed. The presented results correspond to the 18-bit ADC/DAC resolution and utilized filter order is N=16.
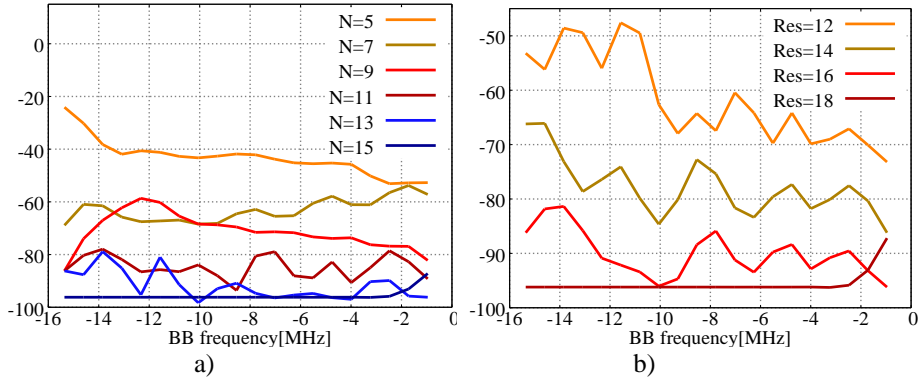
Fig. 4 a) IRR results as a function of filter order N and BB frequency. b) The impact of ADC/DAC resolution Res on IRR results at different BB frequencies.

Simulations gave valuable information about required complex filter order N and ADC/DAC sampling rate. In simulations, the influence of filter order N on IQI mitigation performance is investigated. The N is gradually increased from N=5 to N=15. The IRR results, as a function of N, are presented in Fig. 4a). The results correspond to the 18-bit ADC/DAC resolution and the sample rate of 61.44MS/s. The results in Fig. 4a) show dependence between the selected filter order and obtained IRR values. The imbalance is more efficiently compensated with the increase of N. On the other side, lower N occupies

less hardware resources. If we take the result as satisfactory when IRR is improved over 60dB, it can be concluded that filter order should be greater or equal than N=7.

Finally, the impact of ADC/DAC resolution on IQI mitigation performance is analyzed. The resolution, denoted with parameter Res, is changed from Res=12 to Res=18, with a step of ΔR=2. In the simulations the filter order is set to 16 and the sample rate is 61.44MS/s. The amplitudes of tones at negative frequencies are determined and IRR values calculated. The IRR results are presented in Fig. 4b). The imbalance related images are efficiently suppressed if Res is greater or equal than 14.

5. IMPLEMENTATION AND MEASURED RESULTS

Measurement results are obtained after the method has been implemented in the LimeSDR board [21]. The SDR incorporates a transceiver IC LMS7002M [20] for the frequency conversion between BB and RF. The chip is capable of transmitting modulations at different central frequencies from several MHz to 3.8GHz. The transmitter exhibits FD IQI whose amount is increased with the increase of central frequency [16].
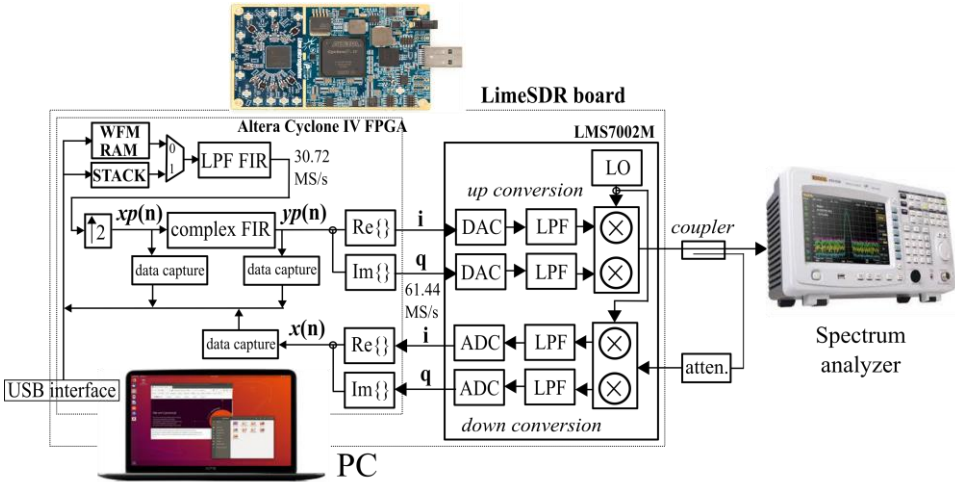
Fig. 5 IQI corrector implementation in the SDR board.

The general block diagram of the SDR board is depicted in Fig. 5. For clarity, only hardware blocks, which are required for method description, are shown in Fig. 5. The Altera Cyclone IV FPGA chip is utilized for the implementation of IQI compensation circuits [20]. The board uses 12-bit DAC/ADCs and it is connected to the CPU core through the USB interface [21]. For the development or demo, the test waveform can be uploaded and played from FPGA internal RAM blocks. In real applications, the CPU core performs digital modem functions transmitting the waveforms over USB interface at a rate of 30.72MS/s [21].

The SDR board implements both transmit (TX) and receive (RX) channels [21]. The IQ corrector is located in the TX path (Fig.5.). For IQ imbalance identification additional

RX channel is used, whose output is represented by the signal $x(n)$ in the Fig. 5. The monitoring path is utilized by the complex filter training process.

The interpolation circuit is used to double the data rate from 30.72MS/s to 61.44MS/s. It is followed by the IQ corrector (the predistorter), implemented as 8th order complex FIR filter. The number of real-valued coefficients is $4(N+1) = 36$. The circuit operates at 61.44MS/s sample rate. Its implementation in FPGA is optimized by multiplexing input data and executing the operations at the clock frequency of 122.88MHz, which is determined by longest propagation delay of FPGA blocks. The 18-bit arithmetic precision is adopted based on the simulation results.

The predistorter occupies following FPGA resources: 2130 combinatorial adaptive look-up tables (ALUT), 3402 dedicated logic registers and 18 DSP blocks. The FPGA have the provision of capturing following signals: the corrector input $xp(n)$, output $yp(n)$ and monitoring path input $x(n)$. The $xp(n)$, $yp(n)$ and $x(n)$ data streams are made available to the CPU core over the USB interface. The coefficients are calculated by software performing the role of the postdistorter. In each RLS iteration step, after the coefficients are calculated, they are sent back to LimeSDR board via USB interface. Beside LimeSDR board and CPU core, the hardware equipment includes the Rigol DSA1030 spectrum analyzer (SA). The SA input is connected to TX output and SA is used for IRR measurements.

a)   b)
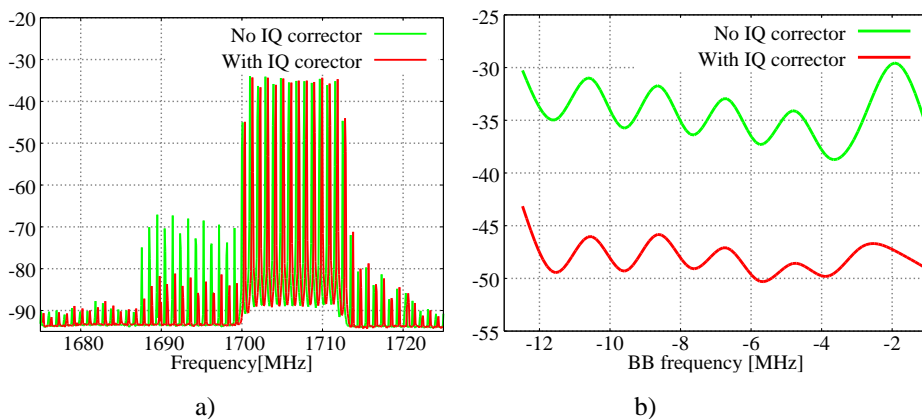
Fig. 6 a) Spectra of signals obtained at transmitter output when 13-tone waveforms is applied, obtained at central frequency of 1.7GHz b) Measured IRR results obtained at the same central frequency.

The software consists of Lime Suite GUI application [21] dedicated to configuration of SDR board and specially created command-line application. At the beginning of measurement process, the configuration file is loaded into LMS7002M using Lime Suite GUI. Also, the LMS7002 DAC and ADC sample rate is configured to 61.44MHz. Upon loading the configuration files, the LMS7002M transmitter is set in un-calibrated state.

The command-line application is created specifically for IQ calibration process control. It implements the postdistorter, performing the operations defined by (11) – (13). In order to automate the measurement process, the application provides control of SA via virtual instrument software architecture (VISA) interface. The IRR measurements are conducted before the calibration, and after the calibration is done.

In order to assess the IQI mitigation performance, asymmetrical positive-band thirteen-tone waveform is used as a test signal. The waveform is generated at the rate of 30.72MS/s. The frequencies of successive tones are spaced by 0.96MHz, covering the frequency range from DC to the 12.48MHz. Besides, the LMS7002M local oscillator (LO) is tuned to the frequency of 1700MHz.

Fig. 6a) illustrates the results by showing power spectral densities of the transmitter output with and without using IQI corrector. The IRR values, measured at negative BB frequencies, are given in Table 1. It can be seen from Fig. 6b) that IRR is increased from 35dB, measured for un-calibrated transmitter, to approximately 50dB.

Table 1 IRR at negative frequencies for 13-tone waveform

f [MHz]		-6.72	-5.76	-4.8	-3.84	-2.88	-1.92	-0.96
IRR[dB]	Corr. off	32.92	37.3	34.08	38.46	35.4	29.56	36.31
	Corr. on	47.08	50.27	48.57	49.81	47.04	47.38	49.19
f [MHz]			-12.48	-11.52	-10.56	-9.6	-8.64	-7.68
IRR[dB]	Corr. off		30.27	34.92	30.99	35.76	31.71	36.4
	Corr. on		43.15	49.46	46.01	49.32	45.82	49.07

6. DISCUSSION

The simulation and measurement results demonstrate an efficient IQI mitigation without sacrificing the transmitter output power. The advantage of the proposed method is that the transmitter's static IQ calibration procedure is not required.

The IQI correction is implemented using a complex FIR filter whose coefficients are found iteratively by an RLS algorithm. The postdistorter is implemented in the software. In each iteration step, new coefficients are calculated and sent back to the predistorter. The FIR registers are programmed periodically, once after every several seconds during the transmitter operation. In simulations the impact of complex filter order N on IRR results is analyzed. It is shown that N should be greater than 8 in order to have IRR values greater than 60dB. Furthermore, in simulations the impact of ADC/DAC resolution on the IQI compensation performance is analyzed. The resolution Res=14 gives satisfactory IRR results.

The IQ compensation performance of the method is evaluated after it is implemented in low-cost SDR board. The resolution of ADC/DACs, located in the transceiver IC LMS7002M, is limited to 12 bits [21]. The data rate of digital interface between FPGA and LMS7002M is limited to 61.44MS/s [21]. The ADC/DAC sampling rate is 61.44MS/s, while the signal bandwidth, for which the compensation is performed, is 30.72MHz.

The method provides low complexity in terms of a reduced number of coefficients. The number of coefficients is $4(N+1)$. For parameter N=8, the number of coefficients is 36. A reduced number of coefficients enables savings of FPGA resources. It is worth mentioning that beside the IQ corrector, the TX chain includes the other digital blocks, such as the crest factor reduction (CFR) and post-CFR FIR filters, for which implementation significant amount of FPGA resources is required [22].

In a simulation and in real measurements asymmetrical multi-tone signal is used as test waveform. However, in a simulation and in real measurements the system parameters are not identical. In simulations, the waveform sample rate is 61.44MS/s. The highest tone is positioned at 15.36MHz, which is half of the Nyquist frequency. In the measurements, the

sample rate of the input waveform is 30.72MHz, and therefore, it was impossible to generate a tone at 15.36MHz. Instead, in measurements, thirteen-tone waveform is used. After the interpolation block is utilized, the sample rate is increased to 61.44 MS/s and the Nyquist frequency became 30.72MHz. The highest tone in the waveform is made close to the half of the Nyquist frequency. The measurement results, which are presented in Table 1, confirm the accuracy of the simulation results. Before compensation is performed, the average IRR is 34.16 dB. After the compensation is performed, the average IRR becomes 47.85dB. Although the IQI effects are observed and analyzed for negative image frequencies, the method gives similar results if IQI is present at positive frequencies.

The advantage of the proposed IQ corrector, compared to MP DPD [15], is reduced ADC/DAC sampling rate. For example, in order to transmit 100MHz wideband signals, the MP DPD ADC/DAC sampling frequency must be at least 500MHz [15]. If the proposed method is used for transmission of 100MHz signals, very high-speed ADC and DAC are not required. Sufficient ADC/DAC sample rate is 245.76MS/s. Transmitted signal bandwidth maximum is equal to the half of a sampling frequency. Moreover, being adaptive, the proposed method has significant advantage over the method presented in [16]. The proposed IQ calibration method is generic and can be applied in wideband transmitters.

Table 2 Comparison of proposed method with the methods found in literature

reference	BB bandwidth [MHz]	Sample rate [MS/s]	Central frequency [GHz]	Before comp. IRR[dB]	After comp. IRR[dB]
[23]	400	800	11	20	45
[13]	150	10000	1	40-45	50-55
[16]	100	245.76	1.5-3.5	20-30	45-55
proposed	30.72	61.44	1.7	35	50

Another advantage of the proposed IQ corrector is reduced complexity. The MP DPD parameters are chosen to accommodate a specific PA architecture and transmitter IQI characteristics. The number of MP DPD coefficients is significantly larger than in the proposed method. In order to achieve similar IQI compensation performance, the MP DPD memory length should be equal to complex filter order. For the selected nonlinearity order $M=2$ and memory length $N=8$, the total number of MP DPD real-valued coefficients is 72 [15]. For $N=8$, the number of coefficients in proposed IQ corrector is 36. The number of utilized DSP blocks is directly related to the number of coefficients and it is limited by FPGA resources. Moreover, measured results showed that the IQ gain and phase errors get increased with the increase of SDR central frequency, demanding greater N value [16]. When comparing measured results with the results from literature test-bed conditions cannot be neglected, such as the number of bits of the waveforms, the data rate and DAC/ADC resolution. The measured results found in literature are produced using laboratory equipment that relies on high-performance signal generators. Moreover, calibration procedures are realized in MATLAB. The Ref. [23] uses a wideband transmitter with a 400MHz bandwidth, operating at 11GHz.

The circuit parameter estimation is carried out by high-performance BB/DAC boards and the CPU board, where a DAC with 16-bit resolution and 800MS/s sampling rates were used. The CPU board performs signal processing. Automatic parameter estimation

software is achieved using MATLAB. By compensating for IQI, the image components were reduced less than the IRR threshold of 45dB, the method yields increase in IRR by 10-15dB. In Ref. [13] 10dB IRR enhancement is achieved. The method produces more that 50dB IRR on both sidebands, which indicates that the FD IQI is mitigated well. In the Ref. [16] 20-25dB increase in IRR is achieved for the signal bandwidth of 100MHz.

7. CONCLUSION

In this paper we consider the effects of the IQ imbalance in wireless transmitters and propose low complexity IQ correction method, based on the indirect learning architecture. The method yields linearization results comparable with conventional DPD solutions while minimizing the number of coefficients. The method performance has been evaluated after it is implemented on the SDR board. The measurement results show excellent performance in terms of IRR. The IQI images are suppressed down to the noise floor. In case of multi tone waveform the IRR improvement of 15dB is achieved. Measured results are derived with ADC/DAC sample rate of 61.44MS/s. Transmitted signal bandwidth is 30.72MHz. The proposed method is generic and can be utilized in other SDR platforms transmitting wideband signals.

REFERENCES

[1] V. Stanković and Z. Perić, "OFDM Low Complexity Channel Estimation using Time-Frequency Adjustable Window Functions", *Facta Universitatis, Series: Automatic Control and Robotics*, 2022, vol. 21, no. 2, pp. 107–116, DOI:10.22190/FUACR210824009S

[2] J. K. Cavers, "The effect of quadrature modulator and demodulator errors on adaptive digital predistorters for amplifier linearization", *IEEE Transactions on Vehicular Technology*, 1997, vol. 46, no. 2, pp. 456–466, DOI:10.1109/25.580784

[3] Z. A. Khan, E. Zenteno, P. Händel, M. Isaksson, "Digital Predistortion for Joint Mitigation of I/Q Imbalance and MIMO Power Amplifier Distortion", *IEEE Transactions on Microwave Theory and Techniques*, 2016, vol. 65, no. 1, p. 322–333. DOI: 10.1109/TMTT.2016.2614933

[4] M. Valkama, "Advanced I/Q signal processing for wideband receivers: Models and Algorithms", Ph.D. dissertation, Tampere (Finland): Tampere University of Technology, 2001. ISBN:9521507152

[5] J. Tuthill and A. Cantoni, "Efficient compensation for frequency-dependent errors in analog reconstruction filters used in IQ modulators", *IEEE Transactions on Communications*, 2005, vol. 53, no. 3, pp. 489–496, DOI:10.1109/TCOMM.2005.843455

[6] A. G. K. C. Lim, V. Sreeram and G.Q. Wang, "Digital compensation in IQ modulators using adaptive FIR filters", *IEEE Transactions on Vehicular Technology*, November 2004, vol. 53, no. 6, pp. 1809–1817, DOI:10.1109/TVT.2004.836934

[7] P. Kiss and V. Prodanov, "One-tap wideband I/Q compensation for zero-IF filters", *IEEE Transactions on Circuits and Systems I: Regular Papers*, June 2004, vol. 51, no. 6, pp. 1062–1074, DOI:10.1109/TCSI.2004.829233

[8] L. Ding, Z. Ma, D. R. Morgan, M. Zierdt and G. T. Zhou, "Compensation of frequency-dependent gain/phase imbalance in predistortion linearization systems", *IEEE Transactions on Circuits and Systems I: Regular Papers*, 2008, vol. 55, no. 1, pp. 390–397, DOI:10.1109/TCSI.2007.910545

[9] L. Anttila, M. Valkama and M. Renfors, "Frequency-Selective IQ Mismatch Calibration of Wideband Direct-Conversion Transmitters", *IEEE Transactions on Circuits and Systems II: Express Briefs*, vol. 55, no. 4, pp. 359-363, April 2008, DOI:10.1109/TCSII.2008.919500.

[10] J. K. Cavers and M. W. Liao "Adaptive compensation for imbalance and offset losses in direct conversion transceivers", *IEEE Transactions on Vehicular Technology*, November 1993, vol. 42, no. 4, p. 581–588, DOI:10.1109/25.260752

[11] L. Anttila, P. Handel, and M. Valkama, "Joint mitigation of power amplifier and I/Q modulator impairments in broadband direct-conversion transmitters", *IEEE Transactions on Microwave Theory and Techniques*, April 2010, vol. 58, no. 4, pp. 730–739. DOI:10.1109/TMTT.2010.2041579

[12] H. Cao, A S. Tehrani, C. Fager, T. Eriksson and H. Zirath, "I/Q imbalance compensation using a nonlinear modeling approach", *IEEE Transactions on Microwave Theory and Techniques*, 2009, vol. 57, no. 3, pp. 513–518. DOI: 10.1109/TMTT.2008.2012305

[13] W. Li, Y. Zhang, L.K. Huang, J. Cosmas, C. Maple and J. Xiong, "Self-IQ-Demodulation Based Compensation Scheme of Frequency-Dependent IQ Imbalance for Wideband Direct-Conversion Transmitters. *IEEE Transactions on Broadcasting*. 2015, vol. 61. no. 4, pp. 666-673, DOI: 10.1109/TBC.2015.2465138.

[14] F. Mkadem, M. C. Farres, S. Boumaiza, and J. Wood, "Complexity reduced Volterra series model for power amplifier digital predistortion", *Analog Integrated Circuits and Signal Processing*, 2014, vol. 79, pp. 331–343, DOI:10.1007/s10470-014-0266-4

[15] B. Jovanović and S. Milenković, "Transmitter IQ Imbalance Mitigation and PA Linearization in Software Defined Radios", *Radioengineering Journal,* Vol. 31, No. 1, April, 2022, pp. 144-154 , ISSN 1210-2512, DOI:10.13164/re.2022.0144

[16] B. Jovanović and S. Milenković: "IQ Imbalance Correction in Wideband Software Defined Radio Transceivers", *Radioengineering Journal*, December, 2023, pp. 479-491, ISSN 1210-2512, DOI:10.13164/re.2023.0479

[17] S. Nikolić, G. Stančić and S. Cvetković, "Realization of Digital Filters with Complex Coefficients", *Facta Universitatis, Series: Automatic Control and Robotics*, 2018, vol. 17, no. 1, pp. 25–38, DOI:10.22190/FUACR1801025N

[18] B. Razavi, "Design Considerations for Direct-Conversion Receivers", *IEEE Transactions on Circuits and Systems II: Analog and Digital Signal Processing*, 1997, vol. 44, no. 6, pp. 428–435. DOI:10.1109/82.592569

[19] SystemC (2023), http://accellera.org/downloads/standards/systemc

[20] Limemicrosystems, LMS7002M (accessed 2023), https://limemicro.com/technology/lms7002m/

[21] Limemicrosystems, LimeSDR (accessed 2023), https://limemicro.com/products/boards/limesdr/

[22] B. Jovanović and S. Milenković, "PA Linearization by Digital Predistortion and Peak To Average Power Ratio Reduction in Software Defined Radios", *Journal of Circuits Systems and Computers*, 2020, vol. 29, no. 9, pp. 1–19. DOI: 10.1142/S0218126620501479

[23] M. Kim, Y. Maruichi and J. I. Takada, "Parametric Method of Frequency Dependent I/Q imbalance Compensation for Wideband Quadrature Modulator", *IEEE Transactions on Microwave Theory and Techniques*, 2013, vol. 61, no. 1, pp. 270–280, DOI: 10.1109/TMTT.2012.2228215

Regular Paper

CONTROL SYSTEM OF CATENARY CONTINOUS VULCANIZATION LINE FOR RUBBER CABLES

UDC (681.5.015:675.92.028.2)

Igor Kocić[1], Saša S. Nikolić[1], Staniša Perić[1], Miloš Madić[2], Milan Trifunović[2], Nikola Danković[1]

[1]University of Niš, Faculty of Electronic Engineering, Department of Control Systems, Republic of Serbia
[2]University of Niš, Faculty of Mechanical Engineering, Department of Production and Information Technologies, Republic of Serbia

ORCID iDs: Igor Kocić   https://orcid.org/0009-0002-8569-1180
        Saša S. Nikolić   https://orcid.org/0000-0003-2745-3862
        Staniša Perić   https://orcid.org/0000-0003-4766-195X
        Miloš Madić   https://orcid.org/0000-0002-2310-2590
        Milan Trifunović   https://orcid.org/0000-0002-4653-6957
        Nikola Danković   https://orcid.org/0000-0003-0986-5695

Abstract. *The paper presents the control system of a continuous vulcanization line for the production of cables and conductors with rubber insulation, where the vulcanization process takes place in water and steam (vapour) atmosphere. The control, monitoring and recording of relevant parameters of the whole technological process was carried out with help of PLC (Programmable Logic Controller) and HMI (Human Machine Interface) and KepwareEx server. The control system is used to generate control signals for the regulation of speed, tension force, extruder temperature, water level and steam pressure in the vulcanization tube according to the technological parameters of the line. The monitoring system enables visualization of all technological units of the line via the HMI screens. The parts and entirety of the line are represented by conveniently drawn symbols that change colour depending on the current state and display the variables relevant to the operation of this object. Through the use of the KepwareEx server and database, the values of the variables important for the operation of the plant are recorded in real time. The developed supervisory and control system allows easy operation and monitoring of all important parameters of the plant.*

Key words: *Production line, Rubber conductors, PLC, HMI, KepwareEx*

1. INTRODUCTION

Rubber cables are cables with a rubber sheath and a copper conductor. The number of copper conductors ranges from one to several conductors. They are characterized by good electrical conductivity, robustness and flexibility, which make them ideal for supplying portable electrical equipment, devices on ships and in mines. The main characteristics are weather resistance, abrasion resistance, oil resistance, resistance to high mechanical forces and loads, flexibility and softness, resistance to UV radiation, etc. The high quality and performance is mainly due to the use of standard elastomers. According to the complexity of the assemblies and production units, the lines for the production of rubber cables, medium-voltage and high-voltage cables are very sophisticated and complex. The paper presents the control system of the line for continuous vulcanization of rubber conductors and cables with cross-section from 4 mm² to 95 mm². The line produces cables with insulation and rubber sheath type H05RR-F 300/500V (SRPS EN 50525-2-21 (EN 50525-2-21 / VDE 0285-525-2-21), H07RN-F 450/750V (SRPS EN 50525-2-21 (EN 50525-2-21 / VDE 0285-525-2-21), EpN50 0.6/1KV (SRPS N.C5.350), H01N2-D 100V (SRPS EN 50525- 2-81 (EN 50525-2-81 / VDE 0285-525-2-81) [1].

2. DESCRIPTION OF PRODUCTION PROCESS

The production process of cables with insulation and/or rubber sheathing consists of several production units and stages. They can be basically divided as follows: drawing out the wires of the desired dimensions, stranding them into multi-wire construction which depending on the construction can have one or more copper wires, insulating them on vulcanization lines to obtain a rubber-insulated conductor, stranding conductors into the rope which consists of two or maximum five rubber-insulated conductors and finally insulating the rope by applying a rubber sheath in the vulcanization process (Fig. 1). Vulcanization is a process in which rubber or elastomer materials are passed through a vulcanization tube in a high-pressure water and steam atmosphere. The vulcanization process can be serial or continuous. The rubber used is mostly based on synthetic rubber; ethylene-propylene-diene acid (EPDM), ethylene propylene copolymer (EPR) etc. [2, 3, 4]. In rubber processing, an extruder and a vulcanization tube are used because of undesirable agglomerates and impurities. The process of insulation and sheathing is carried out by melting the rubber obtained by extrusion and applying it to the copper wire or conductor.

Basically, the technological process of continuous vulcanization (CV line) of rubber conductors (cross-linking of rubber) begins in the extruder. Rubber granules or rubber in the form of tapes are inserted into a heated extruder; rubber insulation is prepared in the zones of the extruder, which are heated to a temperature of 80°C to 95°C, depending on the type of rubber. During extrusion, the insulation material is pushed through the extruder barrel at a certain temperature and under certain pressure and under the action of the extruder screw, and after exiting the from extruder barrel, it is applied to the copper conductor passing through the head in which the extruder die is mounted. After that the conductor with the applied insulation enters the vulcanization tube, in which a constant steam pressure (12 bar to 20 bar, corresponding to a temperature of 188°C to 213°C) is maintained [4]. Water vapour in the tube, through which the insulated conductor passes, causes the insulating material to absorb moisture as well as possible, which supports and accelerates the vulcanization process. By regulating the temperature of the extruder, the number of revolutions of the extruder screw,

the pressure of steam and water, the speed of the line (passage of the conductor through the pipe) at the exit of the vulcanization pipe, the insulation of the cable hardens. At the part of the pipe called the meeting point (place of contact between water and steam), the steam pressure is balanced by the water pressure with the constant presence of disturbance caused by water leakage at the exit of the cable from the pipe. Changing the parameters of the vulcanization process - pressure and speed (vulcanization time) - affects the mechanical properties of the elastomer and its tensile strength.
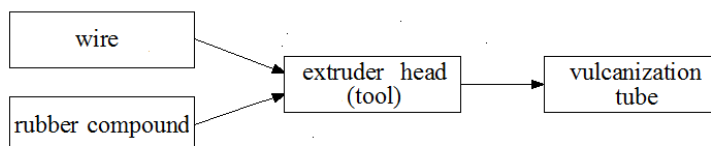

Fig. 1 Simplified block diagram of the technological process of vulcanization

Conventional continuous vulcanization lines are divided according to different spatial settings of the extruder, unwinding system, the vulcanization section (steam section) and winding system.

The line for the production of conductors and cables with rubber insulation consists of the following technical and technological units:
- loading and dosing of rubber granulates or rubber bands,
- unwinding of conductor or wires from the drum,
- tractions (capstans) systems,
- extruders and temperature control systems,
- systems for opening and closing tube, cooling the final product,
- systems for inlet water, inlet steam and meeting point regulation,
- measurement and control of diameter, tension and final cable marking,
- winding of the final product on drums.

A simplified diagram of the process flow is shown in Fig. 2. The production process starts with switching on the main control cabinet and the cabinets distributed along the line, switching on the unwinding drive and loading the drums with non-insulated cable on unwinder, switching on the winding drive and loading the empty drums on the winding device, switching on the system for loading rubber granulate, the extruder and the extruder temperature control system [5, 6, 7]. Unwinding of non-insulated cables or cores is done with an unwinding device. A system of two unwinders and accumulator for the unwound semi-product is used. When changing from one unwinder or rewinder to another, the accumulator receives a certain amount of product so that the production process can continue without interruption. Based on the position of the moving wheel of the wire accumulator, the rotation speed of the unwinder is controlled by the position control method with the PI-controller [8, 9, 10]. After leaving the accumulator system, the uninsulated wire enters the traction system of the line. The traction system consists of three traction devices (capstans). The first traction device is the main traction device, which is located directly behind the accumulator. It operates in the speed mode and its speed is equal to the actual line speed. The second traction device is located directly at the exit of the vulcanization tube. The tube has the shape of a gear wheel; the cable follows the shape of the gear wheel due to its weight. The measurement of

the position of the conductor in the pipe is made by a sensor for the position of the cable in the pipe. The output signals of the sensor for the position of the cable in the tube is used for regulate the speed of the second traction device by using part of the signal in the control system of the PID controller with two degrees of freedom. A third traction device is located behind the cooling trough and monitors the speed in relation to the position of the dancer [5, 6, 11] who placed behind the second traction device.

The extruder is tempered with a heated medium, using distilled water [7]. The water system consists of a central tank with a volume of 1000 l, with controlled level and automatic refilling. Water in that system heated to 40°C and fed through a system of pipes to the heat exchanger of each zone of the extruder. The zones are heated according to the technological parameters. The heat exchanger of each zone consists of a heater and a circulation pump. The extruder barrel (cylinder) is made of a metal layer in which there are placed pipes that surround it and is divided into several temperature zones through which heated water is inlet. The extruder operates in the speed mode and is synchronized with the speed of the main traction device of the line. The application of insulation and the process of vulcanization of the conductor begin with the start of the extruder drive, unwinding drive, tractions device s drive and winding drive.

The centre of insulated conductor is determined so that the insulation is applied evenly around the circumference, the vulcanization tube toward the extruder is closed with a telescopic cylinder and the outlet of tube is closed with a water sealing system, the high-pressure pumps are started, which inject water from the tube outlet side through a proportional control valve, and the introduction of steam is started through a proportional control valve on the inlet side of the vulcanization tube. The control and monitoring is done by the main worker of the plant in cooperation with the auxiliary workers, who perform the loading and unloading of the drums and supervise the unwinding and winding. After leaving the vulcanization tube, the rubber-insulated conductor is cooled in cooling tubs. At the exit of the tub, the water is wiped off with compressed air, the cable is marked, the diameter of the conductor and insulation is measured, and it is packed into process or final drums. The whole process is monitored by the HMI panels, and the relevant process parameters are entered into the database [12, 13, 14, 15, 16, 17]. In the event of a high priority fault, the entire line is stopped with an audible alarm. When the line is stopped either by a completed job or by the occurrence of an error, steam automatically is let out from the pipe; the pipe is flooded with water and cooled.

Figure 3 shows parts of the production process. Figure 3a shows the unwinders and part of the vulcanization tube, Figure 3b shows the main traction device, Fig. 3c shows the heat exchanger for temperature control of the extruder zones, Fig. 3d shows a system of pipes and valves for introducing and discharging water vapour into the pipe, Fig. 3e shows a part of the vulcanization tube directly behind the extruder with a telescopic cylinder to close the tube, Fig. 3f shows the system of pipes and the valve to let water into the pipe on the side of the outlet of the vulcanization pipe, and in the background we see the second traction device directly behind the vulcanization tube, water seal system and the water wiping system.
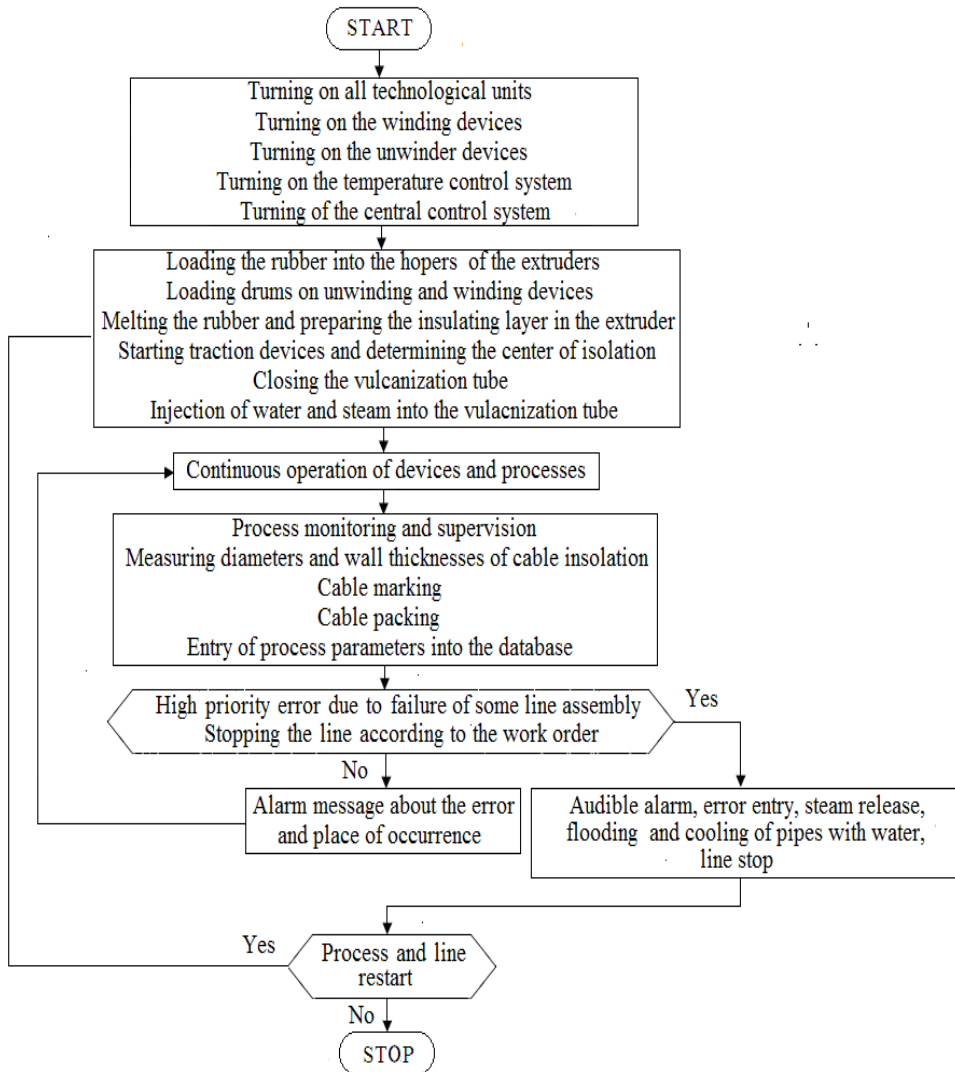
Fig. 2 A simplified block diagram of the rubber cable manufacturing process

Fig. 3 a) Rope unwinding, part of the tube for vulcanization and winding, b) main traction (capstan) device, c) extruder with tempering system, d) steam injection, e) tube closing system, f) water inlet and traction (capstan) device at the exit from the tube

3. CONTROL SYSTEM AND CONTROLLERS

All parts and units of the production process are fully automated; the operation of all drives and units is synchronized with the speed of the main traction device. The designing of the monitoring and control system is a very complex task. The central system for monitoring and control of the plant requires the connection of all parts of the production process into a single functional unit, i.e., the connection of all control and measurement devices into a single unit, taking into account all technical and technological requirements. The control system consists of several PLCs and data acquisition systems, systems for controlling DC and AC motors, on-off valves, proportional valves, heaters, where control is done by position, speed, temperature, pressure, level, etc. One or more different controllers are used for each technological unit. The aim of the implementation is to provide the management of the continuous vulcanization line (CV line) using a PLC and an HMI panel to control the speed of the line, the temperature of the extruder zones, the temperature of the vulcanization tube, the water level in the tube, the steam pressure in the tube, and to allow easy monitoring of all process parameters and their recording in the corresponding database tables in real time [18, 19]. When designing such a control system, it is first necessary to know the production process well and have an accurate overview of all discrete and analogue inputs and outputs, as well as to choose the method and type of control. Then select suitable PLCs and controllers for direct current (DC) and three-phase (AC) drives, as shown in the block diagram in Fig. 4.
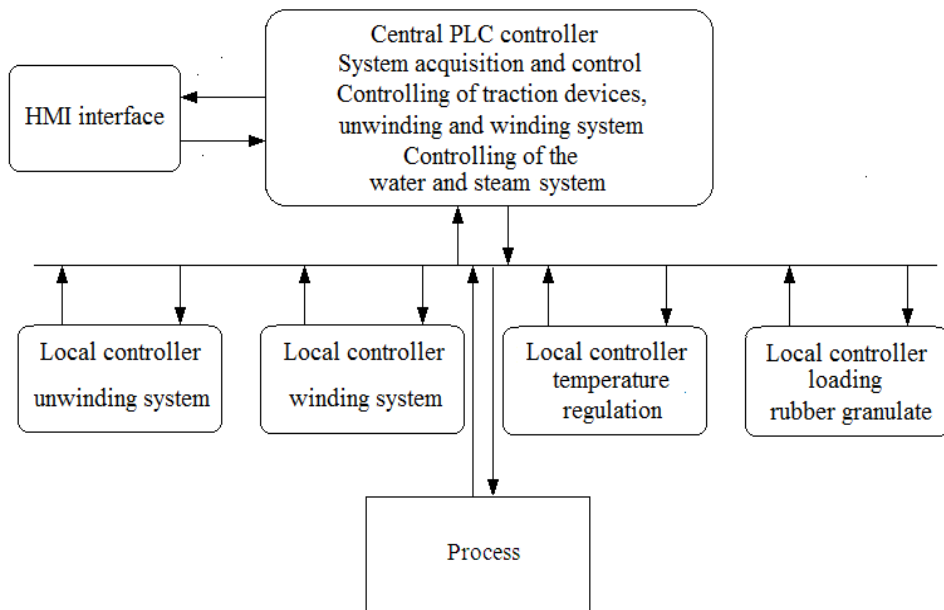

Fig. 4 Control system of the line for continuous vulcanization in the atmosphere of water vapour

One or more different controllers are used for each technological unit. The main controller is Allen Bradley Compact Logix L35E [12, 13]. It monitors and controls the entire process and is located in the main control cabinet. In the technological units for unwinding, winding and temperature control of extruder smaller Allen Bradley PLCs of the MicroLogix 1400 type [20] are used, located in control cabinets along the line. Rubber granulate loading is controlled by a Siemens LOGO 7 PLC. Monitoring and setting of process parameters is performed by a central 15" HMI (touch screen) Magelis XBTGT 7430, a panel located on the main control panel of the line. Unwinding and winding parameters are monitored and set via local 5.7" Magelis HMI panels HMI GTO. All PLCs except the rubber loading and dosing controller, which are connected to the central PLC via an analogue connection, are connected via Modbus or Ethernet IP protocol. In the cabinets along the line there are also controllers for AC drives ABB type ACS 880 [16, 17] and controllers for DC drives Siemens type Sinamics DCM 6RA80 series [14, 15]. Software on the main PLC is written in the ladder diagram and FBD diagram. The control software on PLC consists of the main routine, the indication routine, OP panel routine, routine for inserting, discharging water and steam and control the meeting point of steam and water, temperature control routine, line speed control routine, analogue signal and signal scaling routine and communication routine. The program for PLCs was written in the software packages RSLogix 5000 V20, RSLogix 500 V8.2 and Siemens LOGO! Soft, and the software for HMI panels was developed in the Vijeo Designer V6.0 and V6.2 software packages. Setting of AC and DC controllers was done with the HMI panel for ABB controllers and the Starter tool for Siemens Sinamics controllers.

Maintenance managers can monitor the process using the Kepwarex server and process monitoring application [21, 22]. Different access levels have been defined and permissions have been created at the level of: operator I: worker, operator II: worker, technologist and engineer. The HMI panel consists of several screens corresponding to individual process units. They display the values of process parameters with flows based on the actual appearance of the process. The main screen of the HMI panel also represents the scheme of the entire plant and can be seen in Fig. 6; all technological units from unwinding to winding are clearly visible. Clicking on individual elements opens the screens of the individual parts of the process with the corresponding values and fields for setting the process parameters. The states of the parts of the process are colour-coded and signalled, *yellow* - ready, *red* - malfunction and *green* - operation. Process and status visualization, display and measurement of parameters relevant to process operation, monitoring of alarm signals, selection of manual and automatic operation of the line, monitoring of trend graphs, etc. are easily enabled. The speed of the line is set by the HMI panel or the line speed potentiometer, the speed of the extruder and the main puller is set only by the potentiometers on the main control panel. All default values are set according to the type of the product being manufactured. All devices in the line are synchronized with the main drive unit (main capstan) and accelerate and decelerate the line according to the set ramp times, increasing or decreasing the speed of the line, the number of revolutions of the extruder screw, ensuring a constant thickness of the applied insulation.

In the old control system of line, the meeting point regulation was done by on-off control of the water and steam inlet valves depending on the temperature value at the selected meeting point, so the temperature of the meeting point varied up to ±15°C. In the new solution, the control of the meeting point of water and steam is done by a PID control implemented with the PIDE instruction of the CompactLogix PLC [13] with two degrees of freedom, where the control signal is routed to the proportional valve for the water inlet, while the steam pressure is kept at a constant value. Both valves, for the inlet of

Fig. 5 a) Main control cabinet with CopmactLogix L35E PLC, b) main control desk with HMI panel, c) unwinder cabinet with ABB controllers and MicroLogix 1400 PLC, d) main traction device cabinet with Sinamics DCM converter, e) winder cabinet, f) cable position device cabinet Solz
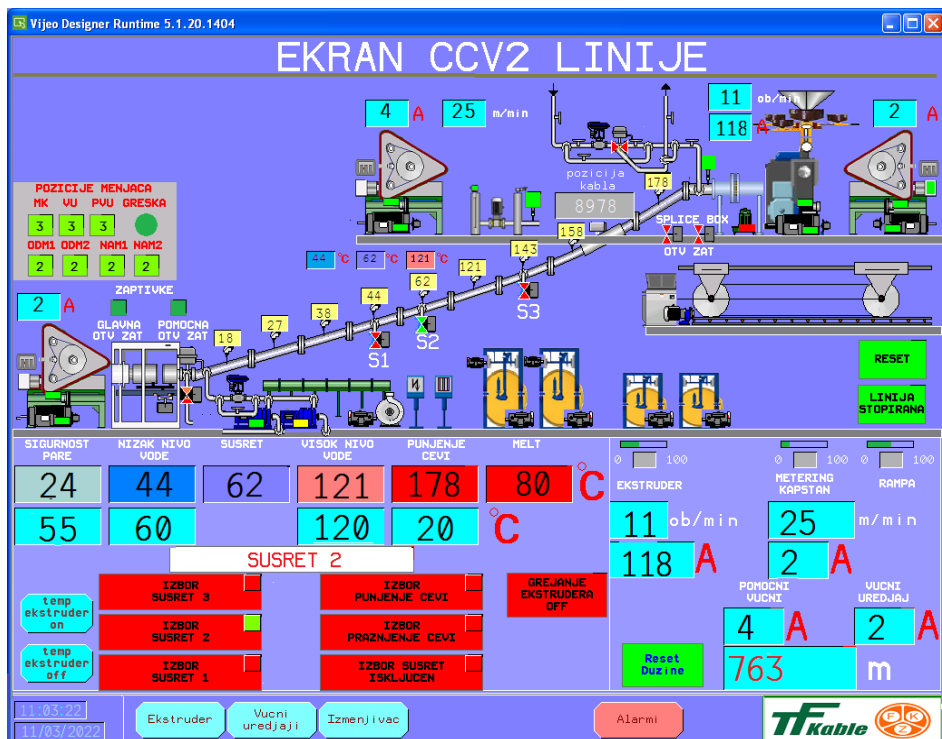
Fig. 6 Technological scheme of the whole line (The main screen)

water and steam, are proportional controlled with current signal. The working pressures in the pipe range from 12 bar to 20 bar. The temperatures at all points of the tube and at the joints are measured by J-type thermocouples, housed in special casings and placed along the vulcanization tube. The signals from the thermocouples are fed into the PLC via temperature cards. Based on the temperature of the meeting point and the temperatures at other points along the pipe, as well as the routine written to control the meeting point, the control signals for the water and steam inlet valves are generated in the range of 4-20 mA. Figure 7 shows the trends of the meeting point temperature corresponding to the set water level and steam pressure (Fig. 7a)) and the trend of the steam pressure when steam is introduced into the vulcanization tube (Fig. 7b)), where the abscissa is the time and the ordinate is temperature of water (Fig. 7a) and the steam pressure in the range from 0 to 20 bar (Fig. 7b). The resulting oscillation of the meeting point steam and water temperature is in a range of less than ± 5 °C.

A block diagram of the vulcanization pipe showing the choice of meeting point is shown in Fig. 8. A total of nine thermocouples, labelled Tc1 to Tc9, are installed to the vulcanization tube. Thermocouples Tc1, Tc2 and Tc9 serve as indicators of the presence of steam at the end of the tube and the presence of water at the entrance to the tube, respectively. In the event that the steam at the end of the pipe drops to the position of thermocouple Tc2, the software automatically turns on both high pressure pumps and tries to push the steam towards the meeting. If this action is unsuccessful, as indicated by the presence of steam at the position

of thermocouple Tc1 (steam safety), the valve for discharging steam is turned on to automatically release the steam from the pipe. When the water reaches the inlet of the pipe Tc9, the pump, which is working at that moment, is switched off. Such situations are accompanied by sound and light alarms. Before starting the vulcanization process, you can select one to three fixed meeting points by simply pressing one of the three buttons on the HMI panel. When the vulcanization process starts, the software automatically prohibits the selection of any other type of meeting point.
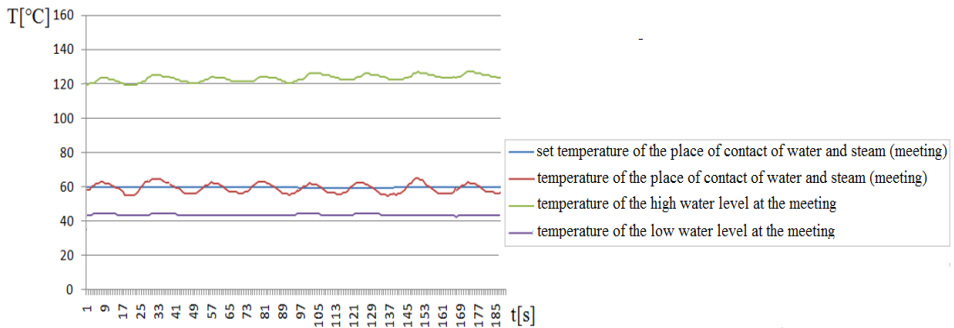

Fig. 7a Dependence of meeting point water and steam temperature, high and low water levels on meeting point, obtained from data from the database
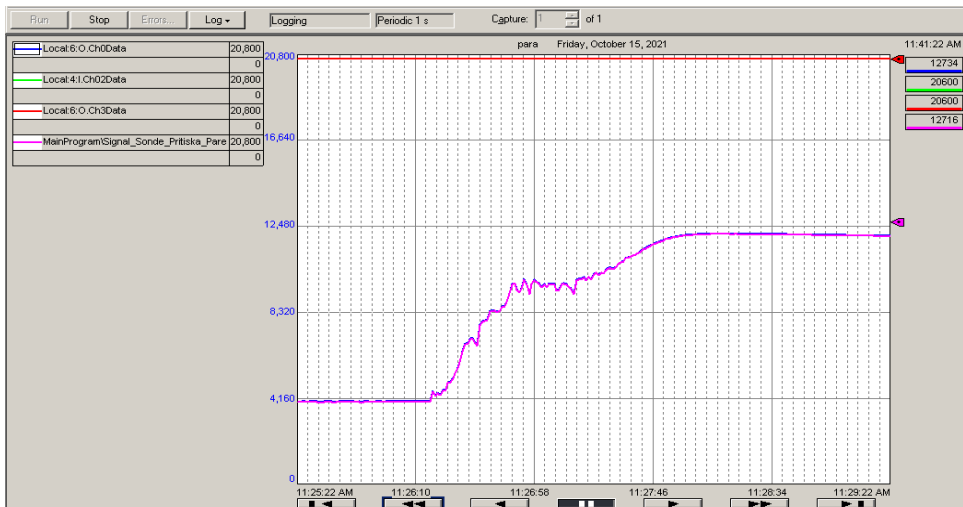

Fig. 7b Steam pressure trend when steam is admitted into the pipe obtained directly on the OP panel (HMI screen)
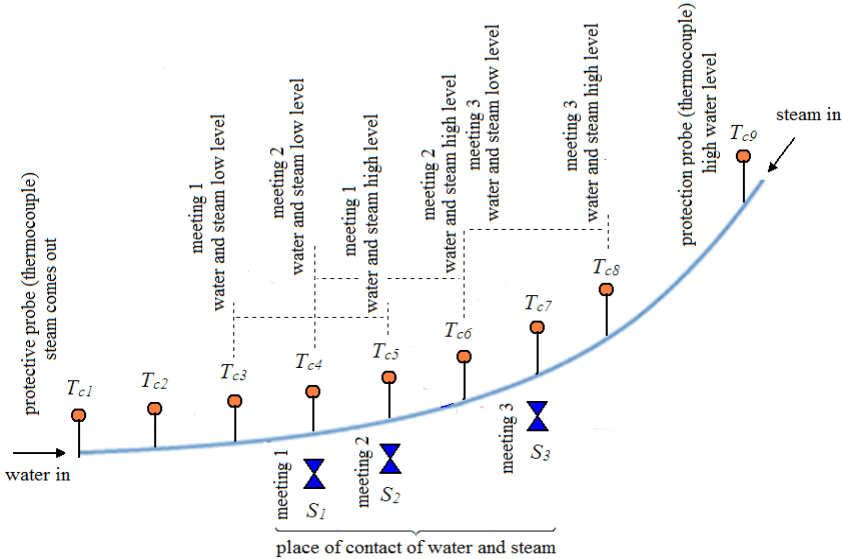
Fig. 8 Control of the meeting point of water and steam

The management system for vulcanization control consists essentially of a system for regulating the speed of the line (passage time of the cable through the vulcanization section) and regulating the pressure of steam and water in the pipe. In addition to the selection of the meeting point, it is possible to select the water injection operations, i.e. the flooding (cooling) of the pipes and the emptying of the pipes. These operations are allowed only when the line is not started. The filling action with water is also used for tube cooling.

The meeting point regulation routine realizes the control of the meeting point, the inlet of water and steam, the flooding and draining of water and steam. The length of the steam section is chosen by selecting the meeting point. The regulation of the water level is based on the set temperature of the meeting point, the temperature of the meeting point and the temperature of the high and low level of the meeting, while the regulation of the steam pressure is based on the measurement of the current steam pressure in the tube and the set desired value of the steam pressure. The temperature values on the thermocouples for the high and low water level at the junction also enter in the regulation process. The worker selects one of three encounters. The condition for letting steam in means that the vulcanization pipe is closed, i.e., connected to the extruder head at the inlet and closed with a seal at the outlet. By selecting the meeting point when the pipe is closed, the high pressure pumps are started in automatic mode and the water and steam injection starts. Before the pipe is closed, the worker adjusts the thickness of the insulation. Two PIDE instructions from the PLC [13] control the water steam meeting point depending on the temperature at the selected meeting point.

A screen monitoring part of the process of tempering the extruder with a heated liquid (distilled water) is shown in Fig. 9. The values of the desired temperatures of the extruder zones are entered in the blue boxes, and the red boxes indicate the current (reached) temperature. The blue and red bar graphs show the current and the (desired) set temperature trends, respectively.

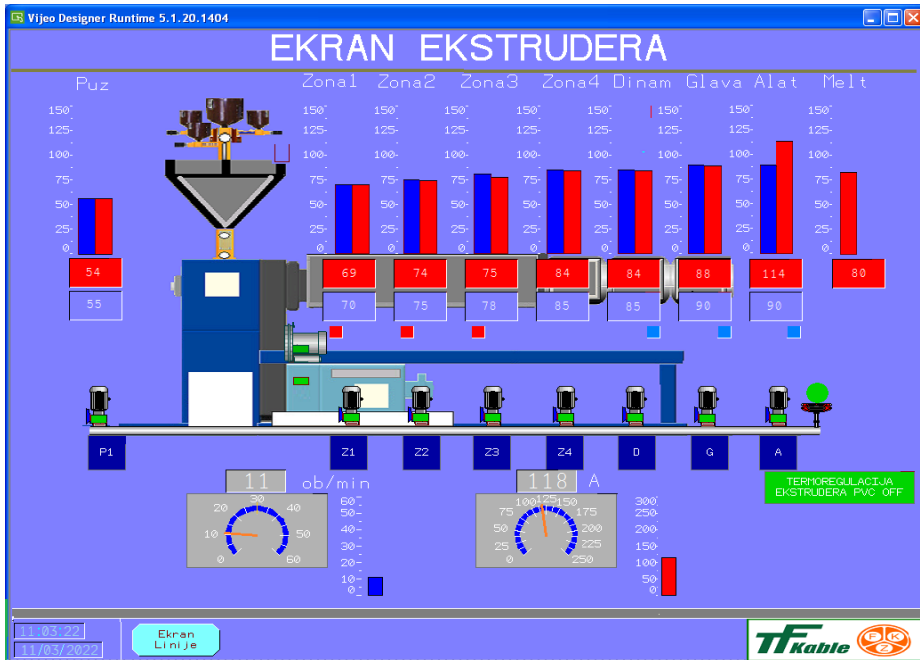**Fig. 9** Technological diagram of all parts of the system for driving and tempering the extruder (HMI screen)
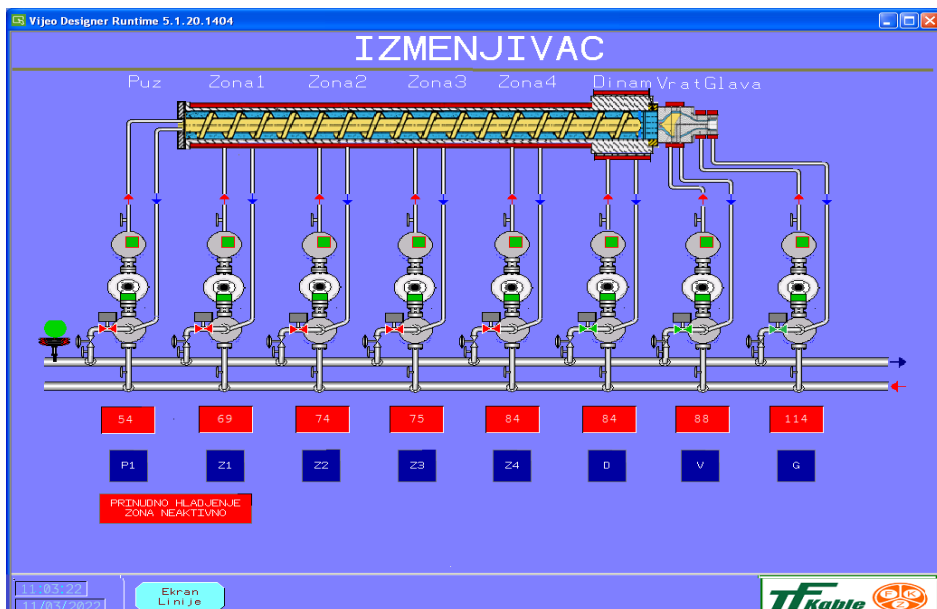

Fig. 10 Technological diagram of all parts of the system for driving and tempering the extruder (HMI screen)

All operating states of the extruder drive and the zone circulation pumps are signalled by colour, *yellow* - ready for operation, *red* -failure and *green* -in operation. The current drive motor current and the speed (screw revolutions) of the extruder are displayed with bar graphs and pointer gadgets. Pressing any circulation pump opens the screen for the exchanger, which is part of the extruder temperature control system (see Fig. 9).

5. Conclusion

A monitoring and control system based on HMI, PLC and KepwareEx server with all decentralized peripherals was developed to control the technological units that are an integral part of the production of rubber cables through the process of vulcanization in a water vapour atmosphere. The control of rubber granulate into extruder hoper loading, regulation of extruder temperature, speed, pressure and water level in the vulcanization tube, etc. was carried out taking into account all possible situations during the operation of the machine and all devices, with warning alarms and alarms that stop the operation of the line. All units from loading to the final product are controlled relatively easily through the graphic evaluation of all parts and units of the process.

The control system ensures proper operation of the line. In addition to regulating the operation, it also takes into account the quality of the insulation in terms of cable parameters and its thickness. With the help of the Kepware server and database, it is possible to create and print reports. Special attention is paid to the control and regulation of steam and water supply with a view to safe operation. Protections have been made to close the tube and automatically release the steam if the pressure is exceeded occurs or steam escapes from the tube of the end of tube. Alarm signals are displayed on the panels with text and flashing signals, accompanied by audible signals. Alarms are also stored in the panel's log and in the database. Lower priority alarms are displayed on the panel and are active as long as a fault is present, indicating the times of occurrence and fault. In addition, the current values of temperature, pressure, size of insulation thickness, etc. are recorded. The process has been completely automated which reduces waste and increases the reliability of the plant. Designing was carried out, new electrical cabinets were made, equipment was selected for operation and management of all parts and units of line, software for PLC and panels was developed, a cable position sensor was installed in the vulcanization tube. The proof of this is that the line in the cable factory has been in operation for five years; cables for the European and USA markets are produced on the line. A new technical solution was introduced to regulate the meeting point of water and steam in relation to the length of the vulcanization section, with regulation of the water level in the pipe based on the meeting temperature. A similar system was introduced in the insulation application line with a one traction device.

REFERENCES

[1] Novi katalog proizvoda Fabrike kablova Zaječar, 2022, [Online]. Available: http://www.fkz.rs/katalozi/FKZSPDF.pdf

[2] B. E. Roberts, S. Verne, "Industrial applications of different methods of cross-linking polyethylene", *Plast. Rubber Process Appl.*, vol. 4, no. 2, pp. 135–139, 1984. [Online]. Available: https://www.osti.gov/etdeweb/biblio/6510656

[3] K. Schwarr, C. H. Chien, Ethylene-propylene co and ter polymer rubber, Report 4b, Menlo Park, CA: Stanford Research Institute.

[4] V. Seymour, Z. Gomzi, "Modeling of the power cable production line", *Thermochimica Acta*, vol. 457, no. 1-2, pp. 70–82, 2007. doi: 10.1016/j.tca.2007.02.020

[5] I. Kocić, D. Mitić, S. S. Nikolić, N. Danković, P. Đekić, "Upravljanje multimotornim sistemom kontinualne linije upotrebom konvencionalnih regulatora", *Zbornik radova međunarodnog simpozijuma INFOTEH-JAHORINA,* Jahorina, Bosnia and Herzegovina, March 15.-17., 2023., pp. 158–163.

[6] S. S. Nikolić, I. Kocić, D. Antić, D. Mitić, N. Danković A. Milovanović, P. Đekić, "The winder dancer position control model using different PID control structures and micrologix PLC", *FACTA UNIVERSITATIS Series: Automatic Control and Robotics*, vol. 21, no. 2, pp. 77–93, 2022. doi: 10.22190/FUACR220409007N

[7] I. Kocić, Uputstvo za rad i održavanje linije za kontinualnu vulkanizaciju gumenih provodnika i kablova CCV2, "TFKable Fabrika kablova Zaječar" u Zaječaru, 2019.

[8] I. Kocić, S. S. Nikolić, D. Mitić, P. Đekić, N. Danković, N. Jotović, "Data collection tool for process identification using PLC and Kepware Tools", *FACTA UNIVERSITATIS Series: Automatic Control and Robotics*, vol. 21, no. 3, pp. 177–186, 2022. doi: 10.22190/FUACR221118014K

[9] I. Kocić, S. S. Nikolić, D. Mitić, A. Milovanović, N. Danković, P. Đekić, "Simulation analysis of feedforward-feedback control of winding device using 2-DOF control structure and control structure in state space", *Proceedings of the 20th International Conference on Thermal Science and Engineering of Serbia - SIMTERM 2022,* Niš, Serbia, October 18.-21., 2022., pp. 573–581.

[10] S. S. Nikolić, I. Kocić, D. Antić, D. Mitić, A. Milovanović, P. Đekić, N. Danković, "Torque regulation of the output pulling device of the cable line for insulation", *Proceedings of the 20th International Conference on Thermal Science and Engineering of Serbia - SIMTERM 2022,* Niš, Serbia, October 18.-21., 2022., pp. 558–572.

[11] S. S. Nikolić, I. B. Kocić, D. S. Antić, D. B. Mitić, N. B. Danković, M. B. Milovanović, P. S. Djekić, "Speed and tensile force control of the pulling devices of the continuous line", *Thermal Sciences*, vol. 27, no. 6A, pp. 4447–4460, 2023. doi: 10.2298/TSCI230418138N

[12] Allen-Bradley-Controllogix-Ethernet-Manual, [Online]. Available: https://www.kepware.com/getattachment/c7cd42b2-e3a8-403e-ac5b-ddff9cb03985/allen-bradley-controllogix-ethernet-manual.pdf

[13] Logix 5000 Controllers General Instructions, [Online]. Available: https://literature.rockwellautomation.com/idc/groups/literature/documents/rm/1756-rm003_-en-p.pdf

[14] SINAMICS DCM DC Converter Operating Instructions, 02/2015, A5E34763375/RS-AA/001, [Online]. Available: https://cache.industry.siemens.com/dl/files/240/109478240/att_851818/v1/manual-DC-Converter_en.pdf

[15] SINAMICS DCM List Manual (LH8), 02/2015, 6RX1800-0ED76, [Online]. Available: https://cache.industry.siemens.com/dl/files/243/109478243/att_851774/v1/Listenhandbuch_eng.pdf

[16] ACS880 primary control program, [Online]. Available: https://library.e.abb.com/public/6b0e2b9eba86e68bc1257b0c0053dab2/EN_ACS880_FW_Man_C.pdf

[17] ACS880-01 drives, Hardware manual, [Online]. Available: https://search.abb.com/Library/Download.aspx?DocumentID=3AUA0000078093&LanguageCode=en&DocumentPartId=1&Action=Launch&

[18] I. Kocić, P. Đekić, A. Milovanović, D. Antić, S. S. Nikolić, N. Danković, "Application of KEPServerEX applications for acquisition and supervision of production processes", *Proceedings of the XV International Conference on Systems, Automatic Control and Measurements, SAUM 2021,* Niš, Serbia, September 09.–10., 2021., pp. 17–20.

[19] I. Kocić, S. S. Nikolić, A. Milovanović, D. Mitić, P. Đekić, N. Danković, "Single screw extruder temperature control using PLC and HMI in cable production process", *Proceedings of the 9th International Conference on Electrical, Electronic and Computing Engineering-IcETRAN 2022,* Novi Pazar, Serbia, June 06.–09., 2022., pp. 137–142.

[20] MicroLogix™ 1200 and MicroLogix 1500 Programmable Controllers, [Online]. Available: https://literature.rockwellautomation.com/idc/groups/literature/documents/rm/1762-rm001_-en-p.pdf

[21] KEPServerEx manual, [Online]. Available: https://www.kepware.com/getattachment/2745a0a9-079a-4630-b15c-8081aba1a91d/kepserverex-manual.pdf

[22] XAMPP FOR MYSQL Amey Laxman Gawde, [Online]. Available: https://cs.nyu.edu/courses/Fall12/CSCIGA.2433001/XAMPP.pdf

SURVEYING ARTIFICIAL GLANDS IN ENDOCRINE NEURAL NETWORKS APPLIED IN CONTROL SYSTEMS

UDC (004.032.2)

Miroslav Milovanović[1], Jianxun Cui[2], Jelena Petrović[1], Anđela Đorđević[1], Saša S. Nikolić[1]

[1]University of Niš, Faculty of Electronic Engineering,
Department of Control Systems, Republic of Serbia
[2]Harbin Institute of Technology, School of Transportation Science and Engineering, China

ORCID iDs: Miroslav Milovanović   https://orcid.org/0000-0003-0535-0790
          Jianxun Cui   https://orcid.org/0000-0001-6902-7111
          Jelena Petrović   https://orcid.org/0009-0004-5582-3562
          Anđela Đorđević   https://orcid.org/0000-0003-2611-1246
          Saša S. Nikolić   https://orcid.org/0000-0003-2745-3862

Abstract. *In this paper, an effort would be made to provide a review of current state of the development of artificial glands within endocrine neural networks. The main goal is to systematize the approaches of building the glands, to offer mathematical apparatus behind them, and to describe control logics enabling smooth work and efficient synergy between the glands and traditional neural networks. In the final phase, this work will offer recommendations for selecting optimal gland profile in accordance with a specific use case.*

Key words: *Endocrine neural network, artificial gland, control systems, environmental stimulus, disturbance processing.*

1. INTRODUCTION

Artificial Neural Networks (ANNs) find extensive applications in control systems [1,2,3,4]. They emulate the functionality of the human nervous system, comprising interconnected neurons, hence their name. ANNs serve as nonlinear models for data generalization pertinent to specific processes, effectively tackling the complexity and nonlinearity inherent in systems. Consequently, they are employed to delineate intricate relationships between inputs and outputs, as well as for pattern recognition. ANNs exhibit

rapid and high-quality data processing capabilities, and once trained, these networks can predict potential states or answer queries regarding 'What if?' scenarios. While various types of ANNs and their iterations are utilized in control systems, the following are frequently considered the most prevalent.

A Feedforward Neural Network (FNN) [5] is a commonly employed type of ANN, frequently utilized for regression problems. It operates with information flowing through the network in a unidirectional manner, lacking feedback connections within the network. There exist two primary types of feedforward networks: single-layer networks comprising only one hidden layer, and multilayer networks capable of having multiple hidden layers. In [6], an overview of the utilization of these neural networks for control purposes is presented. This overview highlights the distinctions, as well as the advantages and disadvantages, between variations of feedforward neural networks. A Cascade Forward Neural Network (CFNN) [7], unlike the basic FFNN, has feedback connections that link the input and output layers. It is often used for analyzing time series data and provides feedback about the current state of the system. Recurrent Neural Networks (RNNs) [8] use information from the previous time step, allowing them to remember a sequence of data. RNNs have an additional recurrent layer, enabling the use of the output from the previous time step when processing the current input. This type can be viewed as adding a memory cell to the neural network. RNNs are suitable for speech recognition, applications predicting the next word a user might type, translation, etc [9,10].

Convolutional neural networks (CNNs) are analogous to traditional neural networks in that they self-optimize during operation through learning [11, 12]. A CNN typically consists of three layers: a convolutional layer, a pooling layer, and a fully-connected layer. This type of neural network is primarily used for image classification and pattern recognition, finding applications in facial recognition systems, autonomous vehicles, and various intelligent systems [13,14]. The most significant advantage of convolutional neural networks is the reduction in the number of parameters required for model training. Unlike traditional neural networks, which often require a large number of parameters for image classification tasks, CNNs excel in extracting features from data with a convolutional structure, thereby mitigating two common problems: limited computing power and duration of model training, as well as overfitting. The distinguishing characteristics of CNNs include: (i) neurons in a CNN are not necessarily connected to all neurons from the previous layer, but only to certain neurons, and (ii) multiple connections can share the same weight [15].

Forecasting using neural networks essentially involves processing a specific dataset, training a model, and expecting the network to perform well in predicting the output. However, during the learning process, the network is typically trained on a limited dataset comprising both training and test data, which may not encompass the full diversity of inputs and scenarios encountered by the neural network in a real-world environment [16]. This lack of diversity in the dataset means that the input database may not encompass all disturbances that could arise during the operation of the neural network. Disturbances to the network can arise from external environmental influences, such as external stimuli, or from changes in the internal state of the system itself, such as parameter variations due to system aging. A common challenge faced by ANNs is their inability to always respond adequately and adaptively to sudden disturbances and external influences. ANNs can be characterized by the following limitations: (i) they may not perform effectively at the border of chaos, operating more reliably in an ordered domain; (ii) they have limited memory storage for potentially

useful data; and (iii) they may be inefficient when confronted with dominant external influences.

Mathematically speaking, the general influence of other neurons (h) on a specific neuron i, due to external influences, can be represented as follows:

$$h_i = signal + noise + external\_stimulus \qquad (1)$$

where *signal* represents a useful signal transmitted between neurons, *noise* represents internal disturbances originating from other neurons in the network, and the *external_stimulus* is an external influence. A neural network that adequately responds to external stimuli is characterized by the ability to recognize an occurring pattern and react accordingly when the external stimulus outweighs the noise, allowing the useful signal to prevail.

Focusing on networks that are efficient in dealing with environmental disturbances and noises, in [17,18], the authors proposed a stimulus-dependent neural network (SDNN) that recognizes patterns, with its operation being dominantly influenced by external factors. Their idea was to adapt a neural network and form a model inspired by the way animals in nature react to environmental stimuli. They introduced SDNN with an external pattern serving as a fundamental element in the pattern recognition process. The research was conducted using a standard Hopfield model as a foundation. It was demonstrated that this modified model adequately responds to changes in the external environment, effectively recognizing new external patterns.

The remainder of the paper is organized as follows: Section 2 provides a brief review of endocrine neural networks predominantly used for controlling dynamical systems. Section 3 offers a detailed overview of various types of artificial glands, while Section 4 summarizes the findings and presents recommendations for selecting an optimal gland type and appropriate network structure.

2. A BRIEF OVERVIEW OF ENDOCRINE NEURAL NETWORKS

Given that artificial neural networks are inspired by human beings, it is logical to once again look at how humans react to external stimuli. When external influences act upon living beings, the nervous, endocrine, and immune systems come into play. Living beings receive various stimuli from the external environment, and the nervous system, as the central unit, detects and reacts to them. Considering the wide spectrum of stimuli from the external environment, the nervous system must be capable of detecting, processing, and reacting to them appropriately. After detecting the stimuli, the endocrine system plays a role in secreting hormones depending on the type of stimulus. Hormone secretion actually alters the current state within the system, and based on these hormones, specific cells in the body are activated to recognize that change. It is clear that not all cells in the body respond to all secreted hormones; rather, there is a cause-and-effect relationship between certain cells and hormones. Lastly, the immune system's reaction aims to restore the organism to its normal or original state before the external stimuli were induced.

This approach, concerning the system's response to changes in external conditions, served as the starting idea for the development of Endocrine Neural Networks (ENNs). In this type of neural network, gland cells that simulate cells of the endocrine system are implemented and responsible for secreting hormones depending on the influences from the external environment. In recent years, ENNs have attracted the attention of many

researchers, demonstrating their ability to adequately and effectively react in systems operating under variable conditions and their capacity to provide the system's response to external environmental influences.

The primary objective of this review paper is to offer readers a comprehensive understanding of the evolutionary trajectory of ENNs, elucidating their underlying structures and mathematical foundations. Through this exploration, we aim to underscore their profound relevance and efficacy within the domain of intelligent control for dynamic systems. Additionally, our focus extends to providing actionable recommendations for the selection of ENNs, tailored to environmental stimuli, disturbances, and specific application contexts. These insights will intend to empower researchers in strategically navigating the selection process, thereby optimizing the alignment between endocrine structures and the intricacies of their research problems within the domain of control systems.

3. AN OVERVIEW OF ARTIFICIAL GLANDS

The application of artificial gland cells is directly linked to adjusting neural network signals in response to environmental stimuli. In most cases, these stimuli are utilized to activate the appropriate artificial glands. The simplest and most common function of these glands is to produce specific hormone concentrations and influence the weight coefficients of the neural network. This approach has been observed in various works [6,19-21]. All other implementations of gland cells are partially based on these established principles, with certain modifications and upgrades.

Specifically, the utilization of artificial gland cells in [6,19] involves altering the default structure of neural networks to create endocrine neural networks. The gland cells are assigned the task of producing specific hormone concentrations that affect network weights by multiplying their values with unique endocrine factors generated for each gland. The concentration of hormones depends on environmental stimuli $\delta_1, \delta_2, ..., \delta_i$ representing external inputs corresponding to environmental conditions, disturbances, or noise. The hormone concentration of a single gland (C_g) is expressed in [6,19] as:

$$C_g(t+1) = \beta_g C_g + R_g(t+1) \tag{2}$$

where R_g and β_g are the stimulation parameter and decay constant, respectively. In continuation, index g represents the number of gland in question. Stimulation parameter R_g can be calculated as follows:

$$R_g(t) = \frac{\alpha_g}{1 + C_g(t-1)} \sum_j \omega_{ij}(t) X_{ij}, \tag{3}$$

where α_g is the stimulation rate, ω_{ij} is ij-th weight coefficient and X_{ij} represents a proper input value. Index i presents the current network input, while index j presents the current hormone.

The neuron's output value (before applying the chosen activation function) can be presented as:

$$u = \sum_{i=1}^{n} \omega_i X_i C_g S_j. \tag{4}$$

In (4), S_j signifies a hormone sensitivity parameter within the range of 0 to 1, and n represents the number of inputs for the specified neuron. Neurons with lower sensitivity S_j might produce a negligible impact to the network, whereas those with a sensitivity parameter close to 1 will greatly influence network performance.

The difference between the approaches of implementing artificial glands in [6] and [20] lies in the application of gland structures within different neural networks. In [6] is realized Orthogonal Endocrine Neural Network (OENN) merged with Orthogonal Endocrine Adaptive Neuro-Fuzzy Interface System (OEANFIS), both enhanced with endocrine factors. Such an intelligent hybrid solution was used for control purposes and showed improved performances after processing environmental stimuli. On the other hand, in [20] the same mathematical apparatus for realization of endocrine component was used in order to design a new type of endocrine neural network which is based on the gland implementation inside the traditional Nonlinear-autoregressive model with the exogenous inputs neural network (NARX). Graphical representation of implementing gland cells within the NARX network is presented in Fig. 1. The figure [20] represents a role model and most common way of implementing artificial glands within ANNs.
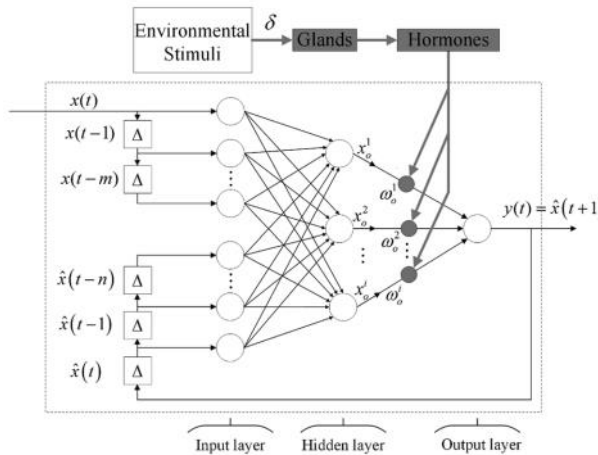
Fig. 1 Implementation of Gland cells within the NARX network [20]

In article [22], once again, the parameter δ, analogous to stimuli, embodies variations in system components and dynamics caused by changes in the environment or working conditions. In the paper, Generalized Quasi-Orthogonal Endocrine Adaptive Neuro-Fuzzy Inference System (GQOEANFIS) is designed with the OEANFIS once again as the core component. By injecting stimuli-like variations directly into the neurons of the fourth layer, the network becomes more adaptable to environmental changes even after the training process, enhancing its ability to respond to dynamic conditions while modeling complex mechatronic systems. In [22], a significant distinction in the implementation of the artificial gland cell is evident compared to the described scenarios in [6][20], where external stimuli influence hormone production. In this study, the stimuli directly affect the fourth layer of the neural network.

In article [19], the authors suggest a design approach for an orthogonal endocrine intelligent controller (OEI controller) applicable for the control of nonlinear dynamical systems. Artificial glands are incorporated into two conventional soft computing substructures (OENN and OEANFIS). These artificial glands serve to stimulate neural network weights in response to external disturbances, changes in the environment, or data from various sensors. In this research attempt, the OENN network's output forms an online stimulus signal (OLS), subsequently introduced to the fourth OEANFIS layer, as an artificially made stimulus. Here, the main contribution was made by proposing rhe OENN's output signal $\hat{y}(t)$ which will be computed using the following equation:

$$\hat{y}(t) = \sum_{i=1}^{n} (\omega_i(t) C_g(t) S_j(t)) \varphi_i(X) + R(X, m, C_g(t), S_j(t)) , \qquad (5)$$

where φ_i is an orthogonal function and $R(X, m, C_g(t), S_j(t))$ represents an expansion error, which is decreasing when the number of expansion terms m increases. OLS is directly introduced to the forth OEANFIS layer, which generates control signal $x(t)$. Finally, the limiter is introduced to restrict the control signal in a specified range.

In the article [23], the authors proposed a new approach to tuning and optimizing the sensitivity parameter S_j. The adaptation of the parameter relies on mimicking the biological mechanisms of excitation and inhibition. Inhibitory signals act as synaptic potentials that prevent a neuron from initiating a pulse (action potential), thereby halting its transmission through the network. Conversely, excitation serves to trigger a neuron to produce a pulse, facilitating the transmission of information across the network by engaging other neurons. Using these principles, the input value of each neuron in the output layer is calculated in [23] according to the following equation:

$$X * P_p = \sum_{i=1}^{n} \left[\begin{array}{l} YN_i W_{pi} C_{GEX}^{p,a} S(G_{EX}^{p,a}; \delta, N_{EX}) \\ + YN_i W_{pi} C_{GIN}^{p,b} S(G_{IN}^{p,b}; \delta, N_{IN}) \end{array} \right], \qquad (6)$$

where $S(G_{EX}^{p,a}; \delta, N_{EX})$ generates the sensitivity of the ath excitatory gland, $S(G_{IN}^{p,b}; \delta, N_{IN})$ calculates the sensitivity of the bth inhibitory gland for the pth output neuron. $G_{EX}^{p,a}$ represents the number of excitatory glands influencing pth neuron weights. Similarly, the number of inhibitory glands influencing pth neuron weights is labeled as b in $G_{IN}^{p,b}$. Finally, W_{pi} is the output weight, d - the adaptive factor, $C_{GEX}^{p,a}$ represents the hormone concentration of the ath excitatory gland of the pth output layer neuron, and $C_{GIN}^{p,b}$ is the hormone concentration of the bth inhibitory gland of the pth output layer neuron.

As an additional contribution in [23], given that the default output of a single neuron is (4), and in order to avoid a possibility of that u could become 0 (for sensitivity S_j equal to zero), the equation 4 is transformed in [23] to:

$$u = \sum_{i=1}^{n} \omega_i X_i (1 + C_g S_j) . \qquad (7)$$

Now, when hormone sensitivity S_j is equal to zero in (7), an endocrine neural network will function as a traditional network without any gland influence, producing neuron output as: $u = \sum_{i=1}^{n} \omega_i X_i$.

Differing from previous papers where each gland was treated as an independent unit, in [17], the authors proposed an approach for improving the performance of the endocrine neural network by establishing mutual connections between glands, thereby enabling comprehensive interactions among them. The role of each gland remains the same as described in papers [6] and [19]; however, in this approach, the concentration of hormones from one gland will depend on the others. For example, if a gland secretes a large concentration of a hormone that is important for other glands, that hormone will have a significant impact on them. This relationship is represented by the following equations:

$$AF_i = \frac{K}{1 + e^{-MO^i}} \; . \tag{8}$$

$$MO_i = \Pi_{h=1, h \neq i}^{n_g} c_h . \tag{9}$$

where AF_i is the interaction coefficient of i-th gland with the value between 0 and 1, and c_h is the concentration of hormone of h-th gland which is determined by accounting the concentrations of other hormones. Based on (8, 9) the cell output can be represented as follows:

$$u = \sum_{i=1}^{n_x} w_i x_i \Pi_{j=1}^{n_g} C_j S_{ij} M_{ij} AF_j - b , \tag{10}$$

where n_x is the number of inputs, n_g is the number of glands in the system, while b is the threshold of the cell.

The paper [18] introduces an Artificial Endocrine Neural Network (AES) as a part of the Artificial Homeostatic System (EAHS), which is inspired by the self-regulation principles in the human organism. AES consists of a module for Hormonal Level (*HL*), Hormone production controller (HPC) and endocrine gland (*EG*). HL is responsible for remembering the level of hormones in the system, the controller has the task of controlling the release of hormones based on the environmental conditions and the internal state of the system. The controller sends information to the endocrine gland, which is responsible for secreting and producing hormones when needed. The hormone production (HP_i) of the i-th hormone is updated as follows:

$$HP_i(t+1) = \begin{cases} 0 & if \; IS_i < \theta_i \\ (100 - \%ES_i) \, x \, \alpha_i \, (Max(HL_i) - HL_i(t)) , \\ \quad otherwise \end{cases} \tag{11}$$

$$IS_i(t+1) = \begin{cases} 0 & if \; (ES_i \geq \lambda_i) \; and \; (HL_i \geq \omega_i) \\ IS_i(t) + \beta(Max(IS_i) - IS_i(t)) , \\ \quad otherwise \end{cases} \tag{12}$$

$$HL_i(t+1) = HL_i(t) \, x \, e^{-1/T_i} + HP_i(t) , \tag{13}$$

In (11), IS_i represents the internal state, ES_i represents the external stimulus and HL_i represents the hormone level. Further, θ_i represents the target threshold for the *IS*, while α_i is the scaling factor. In Eq (12), λ_i is a threshold associated with *ES* and ω_i is a threshold associated with *HL* while β represents the gain value for the rate of change on the internal state. It is also considered that the variable *T* represents the half-life variable.

In the paper [24], an Artificial Hormone Network (AHN) was introduced to enable the robot to respond to changes in the external environment and the internal state of the system. This hormone network comprises hormone channels, sensory channels, hormone receptors (HR), and hormone glands (HG). A Hormonal Gland (Fig. 2) is tasked with secreting hormones whose concentration is influenced by information from the external environment and the system's state.
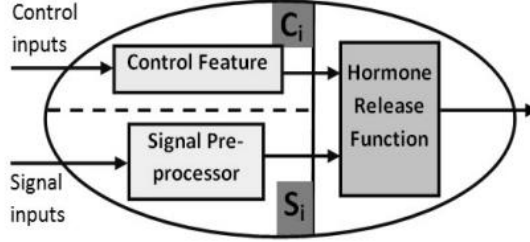

Fig. 2 The hormonal gland mechanism from [24]

There are two types of input signals on each gland: Signal input (Si) and Control input (Ci). These signals enter the Signal Pre-processor and Control Feature blocks, respectively. The pre-processing block receives the signal input and determines how the gland responds to other hormones and external influences, while the Control Feature unit processes the control input to define the effect of each signal input on hormone secretion.

There are two ways to manage hormone secretion: Inhibitory/Stimulatory control and Negative/Positive feedback control. The first method allows for preventing or stimulating hormone secretion based on the switch principle, depending on the presence of external signals or hormones (the presence of a signal is defined by a given threshold). The feedback control enables reduced or increased hormone secretion as a fine adjustment.

The final block is a hormone release mechanism, which identifies the required hormone concentration and instructs the gland to secrete the given hormone. The concentration of the hormone secreted by the gland at each time step depends on the processed input signal, subject to the influence of the stimulation rate (α_g), and the concentration of the hormone in the previous time step, subject to the decay rate (β_g). Below is the definition of the hormone concentration value at time step t:

$$C_g(t) = (\alpha_g F(S_i)) + (\beta_g C_g(t-1)), \tag{14}$$

where $C_g(t)$ represents the hormone concentration in the time step t, and $F(S_i)$ represents the output from the Signal Pre-processor block. It is important to note that the values for C_g, α_g and β_g should be between 0 and 1.

In [25], a hormone feedback mechanism was proposed to protect the system from overflow. The negative feedback cell (Fig. 3) is very similar to an ordinary endocrine gland introduced in previous papers. It is affected only by the concentration of the main hormone and undergoes determined deterioration according to the established dynamics of the gland. Utilizing this mechanism limits the rapid growth of hormone concentration and prevents overflow.
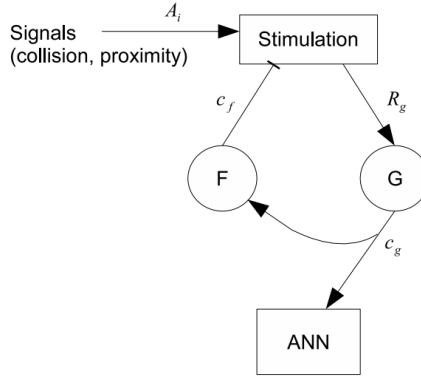
Fig. 3 An artificial neuroendocrine architecture with negative feedback proposed in [25]

The following equation presents the formula for the concentration of the feedback hormone as proposed in [25]:

$$c_f(t) = \beta_f c_f(t-1) + \alpha_f c_g(t) \tag{15}$$

Authors in [26] based their work on developing Artificial Orthogonal Gland (AOG) mechanism. Earlier presented studies focused mostly on acquiring environmental stimuli, converting them into suitable input signals, and delivering them to the glands. Subsequently, hormone concentrations within each gland were computed based on the stimuli level and these calculated values were fed into a neural network to update the values of proper network weight coefficients. Each gland in these papers primarily operated independently of the other involved glands, responding to distinct environmental stimuli. The authors in [26] made a progress in a different direction, proposing a mechanism (Fig. 4) that would enable dependent mutual operations of glands and mutual interactions between different hormones. The structure is designed to accommodate two types of input signals. The Control Input (CI) regulates hormone production, enabling interaction between glands and linking hormones within the hormone network. The Signal Input (SI) determines the hormone stimulation level within a gland and defines its influence on the neural network. As a final remark, it is important to highlight that this mechanism comprises three distinct types or substructures – hormonal, signal, and control mechanisms.
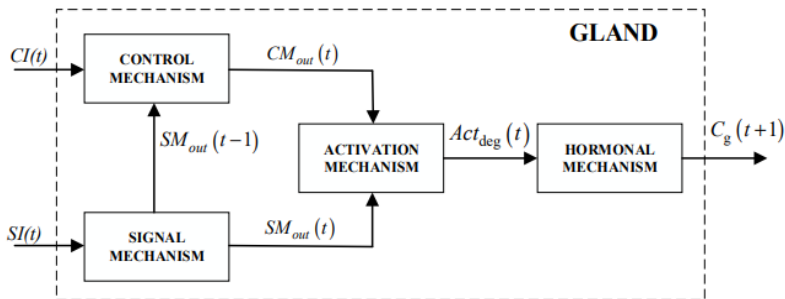

Fig. 4 AOG mechanism from [26]

Finally, in [27], the authors introduced a simplified hormone decay function derived from the Neal/Timmis system. In the original version of the system, the hormone is released and decays according to a geometric function as described by the following equations:

$$r_g = \alpha_g \sum_{i=0}^{nx} x_i \qquad (16)$$

$$C_g(t+1) = C_g(t)\beta \qquad (17)$$

where r_g represents the rate of hormone release, α_g represents the stimulation rate for gland g, x_i represents the input to the gland and n is the number of inputs. $C_g(t)$ and $C_g(t+1)$ represent the hormone concentration in time step t and the following time step $t+1$, while β is the decay constant. However, the authors decided to simplify this process to reduce the number of variables in the system. To achieve this, the hormone decay function was redesigned to use a single variable for both release and decay. This means that the same variable is used to determine the rate of hormone release as well as the rate of hormone decay. In this way, instead of using two separate variables for hormone release and decay, only one variable is used, which simplifies the model and reduces the number of variables to keep track of. The modified equation for determining hormone concentration at time step $t+1$ is below:

$$C_g(t+1) = C_g(t) - r(C_g(t) - q) \qquad (18)$$

where r represents the amount of hormone secreted, and q represents the decay/release rate.

4. RECOMMENDATIONS

In this section, the findings acquired during the review of endocrine networks in the previous part of the paper will be summarized through two perspectives for selecting the optimal type of endocrine network. The first perspective focuses on selecting the right network in accordance with the principles of addressing environmental stimuli and disturbances within the gland mechanisms. The second perspective is based on potential use cases and recommendations on how to select a proper network in accordance with the experimental setup and specific task.

4.1. Gland type selection approach

For control applications requiring adaptive responses to environmental stimuli, the OENN and OEANFIS prove effective. These networks demonstrate suitability in handling variable conditions and disturbances, showing improved performance after processing environmental stimuli. In scenarios where endocrine components need to be integrated into traditional neural network structures, the NARX is a good solution. This type of network is suitable for modeling dynamic systems with input-output relationships, making it a valuable tool in various applications.

For systems requiring a high-level adaptability to dynamic conditions and changes in the environment, the GQOEANFIS is recommended. This mechanism enhances the network's response to environmental variations, thereby improving adaptability while modeling complex systems. In applications where mutual interactions between glands are

desired, the AOG mechanism offers good application potential. This mechanism enables dependent mutual operations of glands and interactions between different hormones, facilitating comprehensive interactions among mathematical units. These networks are effective in scenarios where the concentration of hormones from one gland depends on others, enhancing network performance through comprehensive interactions. Finally, for systems requiring protection against overflow due to a rapid growth of hormone concentration, the Hormone Feedback Mechanism is recommended. This mechanism ensures the stability and reliability of the system in volatile conditions.

4.2. Network selection depending on the use case

Based on the diverse approaches and implementations of endocrine neural networks (ENNs) presented in the previous section, the choice of which type of ENN to use depends on the specific technical requirements of the application and the desired behavior of the control system. From simpler applications such as ENARX for data analysis purposes, to complex hybrid intelligent structures such as OENN-OEANFIS capable of performing complex system control, ENNs have proved as competent models for resolving a variety of control problems. For example, time-series forecasting has a wide range of applications in control systems, especially in the model predictive control since it provides useful information about the potential behavior of a variable in the future. ENNs specially tailored for time-series forecasting are ENARX, Improved Neuro-Endocrine Model (INEM) with gland interaction and OENNPP. All of these networks have proven to perform time-series forecasting and prediction tasks successfully.

Beside the ENN application in data analysis and prediction, these structures have found their purpose as control components of high applicability in control systems. For instance, the structure combining OENN and OEANFIS (OENN-OEANFIS) proved as an effective tool to be utilized for online PID controller tuning, providing the means to design an adaptive system control, sensitive to the varying environmental stimuli. The implementation of this structure is particularly recommended when there is a need to reduce the influence of disturbances and improve the control of highly nonlinear systems. Concretely, the effectiveness of the OENN-OEANFIS model is proved by successfully applying it for 3D crane tracking control. Moreover, the OENN-OEANFIS structure also finds its purpose as an intelligent controller itself, not solely as a PID tuner. As the control structure, it is especially suitable for nonlinear MIMO systems, such as two rotor aerodynamic systems. Another structure suitable to be employed as an intelligent controller in dynamical systems is OENN structure combined with Artificial Orthogonal Glands, or OENN + AOG structure. This structure can be successfully applied in the control of complex nonlinear systems such as magnetic levitation systems.

Further, ENN networks can be utilized in system modeling as well. GQOEANFIS, a structure carefully developed based on the regular ANFIS model with the aim to solve the issues of large computation time and to implement an adaptive mechanism, was designed with the main purpose of modeling complex and highly nonlinear mechatronic systems such as ABS systems. The strengths of this approach are even more emphasized when utilized alongside with a GQOENN model, a structure specialized in predicting the modeling error. This structure is highly recommended for nonlinear system modeling and as a part of complex control algorithms such as quasi-sliding mode control.

Finally, there is a wide range of ENN applications in robotics. For example an artificial endocrine controller has demonstrated promise as a means of solving the issue of the power management in robotic systems. Also, EAHS proved to be an effective structure for behavior coordination in autonomous mobile robots, while AHN network can be used to ensure the robot's high resilience to the changes in the dynamic surroundings. AAES-ANN structure can also be applied to incorporate online adaptation to faults and disturbance in robotic systems, while ANN-AES is successfully applied to enable collaboration in robotic swarm systems.

5. CONCLUSION

This survey paper represents an attempt to summarize the main insights, operational approaches, and applicability values of ENNs. To the best of the authors' knowledge, this is the first attempt to systematize the base of knowledge of ENNs, aiming to provide other researchers in this field with a helpful foundation for further work.

The paper begins by emphasizing the importance of properly addressing environmental stimuli and disturbances when working with dynamic control systems, offering various insights on overcoming these challenges. Subsequently, attention is directed towards a modern approach for efficiently addressing such issues, namely the application of ENNs to adapt systems to volatile conditions. Here, the paper provides basic operational principles of ENNs and introduces foundational components.

The third section constitutes the main part of this survey paper, presenting the primary variants of ENNs proposed thus far. Special attention has been paid to provide prospects for ENN application in robotics. The focus lies on showcasing the operational mechanisms of each endocrine structure, the development of artificial glands, and the integration of each proposed mechanism into a default ANN environment. Additionally, an emphasis is placed on comparing the analyzed solutions and identifying the differences that characterize them.

Finally, the fourth section aims to provide recommendations regarding the selection process of ENNs based on environmental stimuli and disturbances and/or specific use cases for which such networks should be utilized. These recommendations are intended to assist researchers in selecting an optimal endocrine structure for their specific research problem in the domain of control systems.

REFERENCES

[1] M. T. Hagan, H. B. Demuth, O. D. Jesús, "An introduction to the use of neural networks in control systems,", *International Journal of Robust and Nonlinear Control: IFAC-Affiliated Journal*, vol. 12 no 11, pp. 959-985, 2002, doi: 10.1002/rnc.727

[2] S. A. Emami, P. Castaldi, A. Banazadeh, "Neural network-based flight control systems: Present and future," *Annual Reviews in Control*, vol. 53, pp. 97-137, 2022, doi: 10.1016/j.arcontrol.2022.04.006

[3] I. Eski, A. Temürlenk, "Design of neural network-based control systems for active steering system", *Nonlinear dynamics*, vol. 73, pp. 1443-1454, 2013, doi: 10.1007/s11071-013-0875-y

[4]   J. Dunfied, M. Tarbouchi, G. Labonte, "Neural network based control of a four rotor helicopter", In *2004 IEEE International Conference on Industrial Technology*, 2004. IEEE ICIT'04, Hammamet, Tunisia, vol. 3, pp. 1543-1548, 2004, doi: 10.1109/ICIT.2004.1490796

[5]   V. K. Ojha, A. Abraham, V. Snášel, "Metaheuristic design of feedforward neural networks: A review of two decades of research," *Engineering Applications of Artificial Intelligence*, vol. 60, pp. 97-116, 2017, doi: 10.1016/j.engappai.2017.01.013

[6]   M. B. Milovanović, D. S. Antić, M. T. Milojković, S. S. Nikolić, S. Lj. Perić, M. D. Spasić, "Adaptive PID Control Based on Orthogonal Endocrine Neural Networks," *Neural Networks*, vol. 84, pp. 80–90, Print ISSN: 0893-6080, Publisher: Elsevier, December 2016, doi: 10.1016/j.neunet.2016.08.012.

[7]   B. Warsito, R. Santoso, R., Suparti, H. Yasin, "Cascade forward neural network for time series prediction," *Journal of Physics: Conference Series*, vol. 1025, p. 012097, IOP Publishing, May 2018,, doi: 10.1088/1742-6596/1025/1/012097

[8]   R. Qamar, B. A. Zardari, "Artificial Neural Networks: An Overview," *Mesopotamian Journal of Computer Science*, pp. 130-139, 2023, doi: 10.58496/MJCSC/2023/014.

[9]   K. K. Dutta, S. Poornima, R. Sharma, D. Nair, P.G. Ploeger, "Applications of recurrent neural network: Overview and case studies", *Recurrent Neural Networks*, pp. 23-41, CRC press, 2022, doi: 10.1201/9781003307822-3

[10]   A. K. Tyagi, A. Abraham, *Recurrent neural networks: Concepts and applications*, CRC Press, 2022, doi: 10.1201/9781003307822

[11]   K. O'shea, R. Nash, "An introduction to convolutional neural networks," arXiv preprint, 2015. [Online]. Available: https://arxiv.org/abs/1511.08458, doi: 10.48550/arXiv.1511.08458.

[12]   S. Albawi, T. A. Mohammed, S. Al-Zawi, "Understanding of a convolutional neural network," *2017 international conference on engineering and technology (ICET)*, Antalya, Turkey, pp. 1-6, August 2017, doi: 10.1109/ICEngTechnol.2017.8308186

[13]   A. Dhillon, G. K. Verma, "Convolutional neural network: a review of models, methodologies and applications to object detection," *Progress in Artificial Intelligence*, vol. 9 no. 2, pp. 85-112, 2020, doi: 10.1007/s13748-019-00203-0

[14]   M. M. Taye, "Theoretical understanding of convolutional neural network: Concepts, architectures, applications, future directions," *Computation*, vol. 11 no. 3, p. 52, 2023, doi: 10.3390/computation11030052

[15]   Z. Li, F. Liu, W. Yang, S. Peng, J. Zhou, "A survey of convolutional neural networks: analysis, applications, and prospects," *IEEE transactions on neural networks and learning systems*, vol. 33 no. 12, pp. 6999-7019, 2021, doi: 10.1109/TNNLS.2021.3084827.

[16]   H. Chen, J. Chen, J. Ding, "Data evaluation and enhancement for quality improvement of machine learning," *IEEE Transactions on Reliability*, vol. 70, no. 2, pp. 831-847, 2021, doi: 10.1109/TR.2021.3070863

[17]   D. Chen, J. Wang, F. Zou, W. Yuan, W. Hou, "Time series prediction with improved neuro-endocrine model," *Neural Computing and Applications*, vol. 24, no. 6, pp. 1465-1475, 2014, doi: 10.1007/s00521-013-1373-3.

[18]   R. C. Moioli, P. A. Vargas, P. Husbands, "A multiple hormone approach to the homeostatic control of conflicting behaviours in an autonomous mobile robot," *2009 IEEE Congress on Evolutionary Computation*, Trondheim, Norway, pp. 47-54, IEEE, May 2009, doi: 10.1109/CEC.2009.4982929.

[19]   M. B. Milovanović, D. S. Antić, M. T. Milojković, M. D. Spasić, "Adaptive Control of Nonlinear MIMO System With Orthogonal Endocrine Intelligent Controller," *IEEE Transactions on Cybernetics*, vol. 52, no. 2, pp. 1221-1232, Feb. 2022, doi: 10.1109/TCYB.2020.2998505.

[20]   M. Milovanović, D. Antić, M. Rajić, P. Milosavljević, A. Pavlović, C. Fragassa, "Wood Resource Management Using an Endocrine NARX Neural Network," *European Journal of Wood and Wood Products*, vol. 76, no. 2, pp. 687–697, Print ISSN: 0018-3768, Publisher: Springer Berlin Heidelberg, March 2018, doi: 10.1007/s00107-017-1223-6.

[21]   C. Sauze, M. Neal, "Artificial endocrine controller for power management in robotic systems," *IEEE transactions on neural networks and learning systems*, vol. 24 no. 12, pp. 1973-1985, 2013, doi: 10.1109/TNNLS.2013.2271094.

[22]   S. Lj. Perić, D. S. Antić, M. B. Milovanović, D. B. Mitić, M. T. Milojković, S. S. Nikolić, "Quasi-Sliding Mode Control with Orthogonal Endocrine Neural Network-Based Estimator Applied in Anti-Lock Braking System," *IEEE/ASME Transactions on Mechatronics*, vol. 21, no. 2, pp. 754–764, Print ISSN: 1083-4435, Publisher: IEEE, April 2016, doi: 10.1109/TMECH.2015.2492682.

[23]   M. Milovanović, D. Antić, M. Milojković, S. S. Nikolić, M. Spasić, S. Perić, "Time Series Forecasting with Orthogonal Endocrine Neural Network Based on Postsynaptic Potentials," *Journal of Dynamic

Systems, Measurement, and Control, vol. 139, no. 4, pp. 041006-1÷041006-9, DS-15-1656, Print ISSN: 0022-0434, Publisher: American Society of Mechanical Engineers, April 2017, doi: 10.1115/1.4035090.

[24] P. Teerakittikul, G. Tempesti, A. M. Tyrrell, "Artificial hormone network for adaptive robot in a dynamic environment," *In 2012 NASA/ESA Conference on Adaptive Hardware and Systems (AHS)*, Erlangen, Germany, pp. 129-136, IEEE, June 2012, doi: 10.1109/AHS.2012.6268640.

[25] J. Timmis, M. Neal, J. Thorniley, "An adaptive neuro-endocrine system for robotic systems," *2009 IEEE Workshop on Robotic Intelligence in Informationally Structured Space*, Nashville, TN, USA, pp. 129-136, IEEE, March 2009, doi: 10.1109/RIISS.2009.4937917.

[26] M. Milovanović, A. Oarcea, S. Nikolić, A. Djordjević, M. Spasić, "An approach to networking a new type of artificial orthogonal glands within orthogonal endocrine neural networks," *Applied Sciences*, vol. 12 no. 11, p. 5372, 2022, doi: 10.3390/app12115372.

[27] J. Timmis, L. Murray, M. Neal, "A Neural-Endocrine Architecture for Foraging in Swarm Robotic Systems," *González, J.R., Pelta, D.A., Cruz, C., Terrazas, G., Krasnogor, N. (eds) Nature Inspired Cooperative Strategies for Optimization (NICSO 2010), Studies in Computational Intelligence*, vol. 284, Springer, Berlin, Heidelberg, 2010, doi: 10.1007/978-3-642-12538-6_27

Survey Paper

DAILY DANUBE RIVER WATER LEVEL PREDICTION USING EXTREME LEARNING MACHINE APPROACH

UDC (004.85)

Miljana Milić[1], Novak Radivojević[1], Jelena Milojković[1], Miljan Jeremić[2]

[1]University of Niš, Faculty of Electronic Engineering, Department of Electronics, Republic of Serbia
[2]University of Niš, Faculty of Civil Engineering, Department of Mathematics, Physics and Informatics, Republic of Serbia

ORCID iDs: Miljana Milić   https://orcid.org/0000-0001-7037-7709
           Novak Radivojević   https://orcid.org/0009-0000-4423-6224
           Jelena Milojković   N/A
           Miljan Jeremić   N/A

Abstract. *Anticipating water levels in vast riverbeds is crucial for preventing and mitigating floods or droughts, assessing power plant capacity, and facilitating navigation management. This study introduces an innovative water level prediction model utilizing an Extreme Learning Machine developed to solve the issues of low performance of existing forecasting methods. Development of such a system is of extreme importance when talking about the largest European river – the Danube River. Experimental findings reveal the model's satisfactory performance across various accuracy metrics, complexity considerations, and calculation speed. The prediction with the highest error rate based on MAPE criteria was for Prahovo water level prediction over a 365-day period at 2.02%, whilst the most accurate predictions were for Novi Sad and Banatska Palanka over 30 days and 180 days horizons, respectively, at 0.0550%. The highest coefficient of determination (R^2) was achieved with the Novi Sad data at 0.9968, whilst the lowest was observed with the Prahovo data at 0.7353. The ELM model achieved high precision by adjusting the activation functions of the hidden layer neurons, which involved using different combinations of sigmoid and radial-basis activation functions.*

Key words: *Extreme learning machine, Danube river level, time series, forecasting.*

1. INTRODUCTION

Water is one of the most precious natural resources we possess [1]. Without it, life on Earth would not exist. The laws of nature limit our access to water. Although there is an abundance of water on Earth, it is not always easily accessible when needed, at the correct place, or of the right quality. Chemical pollutants that were improperly disposed earlier are now showing up in our water systems. The study of hydrology has evolved over time in order to better understand the complex water systems of the Earth and help with water-related problems. Hydrological challenges require innovative solutions.

On the other hand, it is widely acknowledged that the Danube River provides the foundation for the interstate collaboration and economic growth of the Danube countries. However, the Danube has a significant role in other areas as well, like the promotion of general cooperation among the Danube countries and socioeconomic, cultural, and political development. The Danube River plays a major role in planning and development of appropriate ecological concepts in the sphere of environmental protection, as well as in other areas of interstate cooperation involving the entire Danube region.

Reliable forecasts for various forecast horizons are necessary for solving critical decision-making problems. The hydrological characteristics of the Danube River impact a number of concerns, including navigation, droughts and floods, power plant capacity, and other issues. In time series research, forecasts have traditionally been made using a wide variety of statistical methods, including autoregressive models (ARIMA, SARIMA, etc.), exponential smoothing, dynamic regression models and many others [2-7]. Along with these methods, deep learning models have become popular in research for solving time-series prediction challenges due to their ease of implementation, availability of tools to create prediction models and notable achievements in many different areas of application [8-10]. Deep learning techniques encompass various artificial neural network structures, where recurrent networks such as Long Short-Term Memory (LSTM) [11], [12], Gated Recurrent Units (GRU), etc. stand out in the time series prediction domain due to their ability to capture time series patterns from historical data [13], [14]. The issue that arises with deep learning models is the lengthy process of network training when dealing with a considerable amount of data, together with the complex iterative computation of network parameters. This is particularly an issue with recurrent models as their training process causes high memory consumption due to the models' memory effect and due to the use of backpropagation through the time algorithm for updating the network weights. Another approach, the Extreme Learning Model (ELM), has arisen as a response to the expensive nature of neural network training. Unlike typical neural networks, it does not utilize an iterative error function minimization strategy. In this algorithm, a subset of network weights is initialized to a random value and during training, the rest of the weights are adjusted according to the training input-output pairs using a much simpler process. Due to its speed, simplicity and increasingly widespread usage, ELM is chosen to be the algorithm implemented in this paper for predicting the water level of Danube on multiple measurement stations.

A number of researchers address the hydrological forecasting challenges of the Danube River by employing different statistical or neural network modeling methodologies [15-19]. Because hydrological time series are influenced by numerous independent variables, traditional forecast models struggle to provide effective forecasts. Some advanced hybrid forecasting models have recently been created in order to improve reliability and precision of forecasting results [19-24].

In the study presented in this article, a development of a specific Extreme Learning Machine (ELM) model is performed to make one-step-ahead predictions for daily-time horizons in the Danube River flow through the Republic of Serbia, at seven measuring stations. They are: Bezdan, Zemun, Novi Sad, Banatska Palanka, Veliko Gradište, Donji Milanovac, and Prahovo. The initial study in this field was conducted in [25]. Further research, performed in this study aims to assess and improve the accuracy of the forecasts. Brief descriptions of water level data and ELM modeling follow. After that the Python computer language implementation of the forecasting model is shown. At the conclusion, appropriate forecast performance measures are evaluated and discussed together with suggestions for future research.

2. STUDY AREA

The Danube River's natural attributes set it apart and differentiate it from other European rivers. This river is Europe's watershed due to its length of 2,888 km, navigability, rich natural content, fish, and plant life. Geographically, the Danube springs in the Schwartzwald Mountains of Baden-Württemberg, which are located in the southwest of the Federal Republic of Germany. It is formed by the merger of the smaller rivers Briga and Breg near Donaueschingen [26]. The Danube flows from west to east, passing through several major towns in Central and Eastern Europe (Vienna, Bratislava, Budapest, and Belgrade) before forming a delta in Romania and Ukraine after 2850 kilometers on the Black Sea coast. Throughout history, the Danube has always been an important international waterway.

The Danube is the second European river in length and with a long-term daily mean discharge of about 6500 m^3/s [27]. Fig. 1 shows the portion of the flow of the Danube that goes through Serbia. A section of its course forms a natural border between Serbia and Croatia, as well as Serbia and Romania (138 km toward Croatia and 227 km toward Romania). The Danube has an average width of 600 meters and a maximum width of 2000 meters at the entrance to the Đerdap Gorge. The Đerdap Gorge, which is 97 kilometers long, is Serbia's largest gorge.
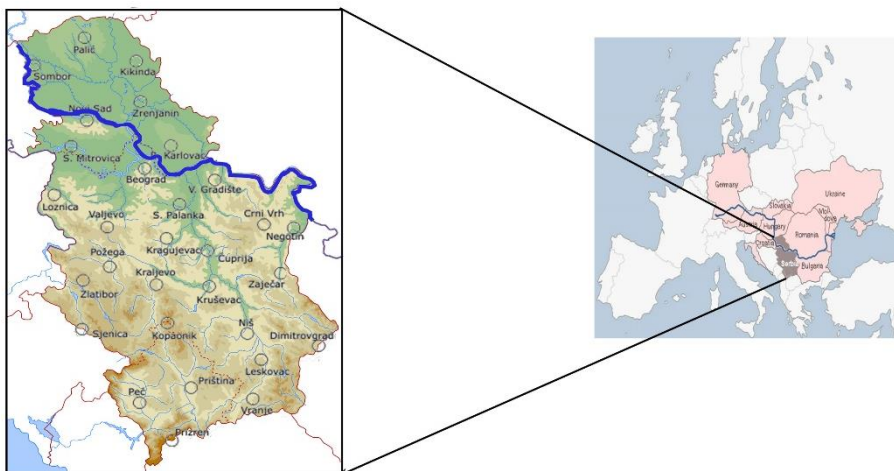

Fig. 1 The Danube River through the Republic of Serbia

The Danube basin, which covers an area of around 801,463 km^2 and represents 10% of the area of the European continent, is home to approximately 80.5 million people in 19 countries through which this river flows [27-29]. The Danube basin is separated into four areas based on its geological structure and geographical layout: upper, middle, and lower Danube, as well as the Danube's delta [30]:

1. Upper Danube Region, between its springs and the Devin Gate, (1,880 r km (river kilometer), basin area: 131,338km^2, long-term annual average discharge 2,051m^3/s).
2. The Central Danube Region lays between the Devin Gate and the Iron Gate (930 r km, basin area 444,894km^2, long-term annual average discharge 5,585m^3/s).
3. The Lower Danube Region is placed between the Iron Gate and the Danube's Delta (132 r km, basin area: 230,768 km^2, long-term annual average discharge 6,563m^3/s).
4. The Danube Delta is located at the Black Sea coast. As a crucial wetland in the Danube River Basin, the Danube Delta covers 6,750 km^2 in area [31], [32].

Since the Danube River supplies water for industry, agriculture, and several eco-systems, it is generally of tremendous ecological, social, and economic worth. In addition, the Danube is crucial for transportation, electricity production, recreation, tourism, fishing, and biodiversity. Aside from its natural features, the Danube region can be recognized by a variety of other characteristics, such as historical legacy, future-oriented planning, increased economic activity, collaboration in various areas of social life, etc.

In 2014 the Republic of Serbia's territory experienced one of the worst natural disasters i.e., an extreme flood [33]. The floods preventions systems either failed to prevent damage, or were never implemented. The riverbeds were rarely cleaned and maintained for decades, and the embankments were not renovated. The pumping stations were also neglected and their functionality was rarely checked. The authorities of the Republic of Serbia have conducted a post-disaster damage assessment after the floods [34], [35]. In general, the serious unpreparedness disturbed lives of many people and animals and did severe damages in urban systems, agriculture, and local economy [36].

Considering the noted deficiencies and the profound impact on the community, there is a compelling need and a motive to proactively address and enhance flood prediction and prevention measures especially in the context of such a large river basin like the Danube's basin. Current state of readiness, as evidenced by the 2014 flood, is insufficient to mitigate the potential future threats posed by the Danube River. The study, conducted in this research aims to contribute to the scientific understanding and practical management of water-related disasters. By employing advanced predictive modeling techniques, such as the ELM approach, this research attempts to provide accurate and timely predictions of the Danube River's water levels. The ultimate goal is to develop a robust framework that can assist authorities in the Republic of Serbia and other regions prone to flooding in implementing more effective flood prevention strategies.

3. THE METHODOLOGY OF ELM MODELLING

Extreme Learning Machine (ELM) is a feed-forward neural network (FFNN) training algorithm based on randomization of network weights, which is primarily applied to networks with a single hidden layer. ELM aims to achieve very high learning speed by initializing a portion of network parameters to a random value using a distribution function, rather than implementing an iterative process and backpropagation to update the weights' values [37]. In

particular, weights between the input layer and the hidden layer, as well as the bias of the hidden layer are randomized, while the weights between the hidden layer and the output are determined in a single step by solving a system of linear equations. This method is shown to be reliable through rigorous mathematical proofs and strong definitions [37].

Since no iterative steps are required, ELM's weight randomization has shown to be a much faster method compared to other algorithms used extensively (such as Gradient Descent) while keeping accuracy at a high level. Short training times achieved by the algorithm combined with easy implementation of feed-forward NNs have contributed to ELM being widely used in many different fields of application.

To generalize, Extreme Learning Machine time series modelling offers several advantages over other forecasting methodologies:

- Fast Training: ELMs usually consist of a single layer of hidden neurons that are randomly initialized, resulting in much quicker training when compared to conventional neural networks such as feedforward or recurrent neural networks. This enables faster testing and refinement of models [38].
- Simple implementation: ELMs are easy to implement and need minimal hyperparameter adjustment. Due to the single layer structure, they have a fewer number of parameters to optimize in comparison to other neural network topologies, which makes them simpler to train and implement.
- Efficient nonlinear modelling: ELMs have demonstrated the ability to perform as well as more advanced time series forecasting techniques, using fewer computer resources. Time series data with nonlinear relationships can be captured by ELMs without the need for explicit feature engineering. They automatically extract pertinent aspects from the incoming data, enabling them to efficiently represent intricate patterns and dynamics. This efficiency makes them appropriate for real-time forecasting applications or situations with restricted processing resources [39], [40].
- Generalization capability: ELMs have shown strong generalization capacity, especially when working with noisy or high-dimensional time series data. When applied to properly pre-processed data, overfitting is less likely to occur [41].
- Scalability: ELMs are capable of efficiently processing large-scale time series datasets because of their straightforward and parallelizable training procedure. Their scalability makes them well-suited for applications requiring handling large volumes of data, including financial forecasting or energy demand prediction [42].

A. *Mathematical formulation of the ELM model*

Mathematical model of the ELM algorithm will be explained on an example regression network (Fig. 2) with L hidden nodes, where:

- x_i is the i-th input node for input data of length N,
- $\mathbf{W}$ is the weight matrix of connections between the input and the hidden layer,
- b_i is the i-th hidden layer bias coefficient,
- a_i is the activation of i-th hidden node,
- y is the output node,
- β_i is the weight of a connection between the i-th hidden neuron and the output.

The goal of the ELM training algorithm is to find the optimal values of the output weights $\beta_1, \beta_2, \ldots \beta_L$ in order to find the best fit model based on the training data. The training algorithm consists of the following steps:

1) Training data preparation
2) Weight and bias initialization
3) Hidden layer output matrix calculation - **H**
4) Calculation of **H**† (the Moore-Penrose inverse of **H**)
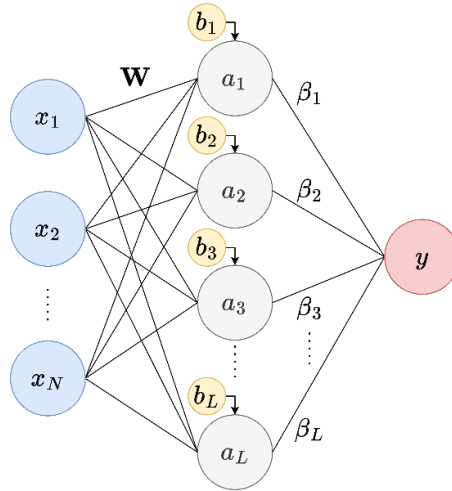5) Output weights vector calculation

Fig. 2 Neural network representation of ELM

Before the training, the pre-processed data set is split into training and test sets. The sets consist of pairs of input vectors and corresponding outputs. The portion of the data set used for training is usually picked to be 60% - 80% of the entire dataset.

Firstly, the input weights in matrix **W** and the biases of the hidden layer are assigned random values with a selected probability distribution. Then, the training samples are passed to the network one by one. For each input-output training pair, the activations of the hidden neurons are calculated by applying an arbitrary activation function $g(x)$. For the training sample t, the activations are computed as specified in equation (1):

$$a_i^{(t)} = g(\boldsymbol{w}_i \boldsymbol{x}^{(t)} + b_i) \tag{1}$$

Here, $\mathbf{w}_i$ is the vector of weights connecting i-th hidden node and the inputs, and $\mathbf{x}^{(t)}$ is the t-th input vector of the training set. All the activations are then stored in the hidden layer output matrix **H**, as shown in equation (2). The matrix consists of L columns (one for each hidden neuron) and n rows where i-th row of the matrix contains activations calculated for the i-th training pair.

$$\boldsymbol{H} = \begin{bmatrix} a_1^{(1)} & a_2^{(1)} & \cdots & a_L^{(1)} \\ a_1^{(2)} & a_2^{(2)} & \cdots & a_L^{(2)} \\ \vdots & \vdots & \ddots & \vdots \\ a_1^{(n)} & a_2^{(n)} & \cdots & a_L^{(n)} \end{bmatrix} \tag{2}$$

According to the model, the network output can be determined as a weighted sum of hidden node activations with $\boldsymbol{\beta}$ being the output weights vector. If all the output data in the training set are stored in a vector $\boldsymbol{y}$, then it follows that $\boldsymbol{H\beta} = \boldsymbol{y}$ which represents a system of linear equations in output weight coefficients consisting of n equations and L unknowns. The solutions to $\boldsymbol{H\beta} = \boldsymbol{y}$ can only be approximate since the high number of training samples results in a system with many more equations than variables which is impossible to solve directly. An approximate solution can be selected so that the norm of the system is minimized, i.e.:

$$\|\boldsymbol{H\hat{\beta}} - \boldsymbol{y}\| = \min_{\boldsymbol{\beta}}\|\boldsymbol{H\beta} - \boldsymbol{y}\| \tag{3}$$

In other words, the resulting vector of $\boldsymbol{H\beta}$ is as close as possible to $\boldsymbol{y}$, which results in a least-squares solution. It can be shown that the solution which satisfies the minimum norm condition is in the form of [43]:

$$\boldsymbol{\hat{\beta}} = \boldsymbol{H}^{\dagger}\boldsymbol{y} \tag{4}$$

Where $\boldsymbol{H}^{\dagger}$ represents the Moore-Penrose pseudoinverse matrix of $\boldsymbol{H}$, which can be calculated as follows:

$$\mathbf{H}^{\dagger} = (\mathbf{H}^{\mathrm{T}}\mathbf{H})^{-1}\mathbf{H}^{\mathrm{T}} \tag{5}$$

In this way, the network output weights are determined directly using a single matrix expression and calculating the Moore-Penrose pseudoinverse could be performed with the help of simpler algorithms such as singular value decomposition. After determining the output weights, the model is completely trained and can be tested or used for making predictions.

B. *ELM model fitting and prediction accuracy measures*

Some of the metrics commonly used for evaluating the accuracy of neural network prediction are Mean Absolute Error (MAE), Mean Absolute Percentage Error (MAPE), Mean Squared Error (MSE), Root Mean Squared Error (RMSE), R^2 or the coefficient of determination and many others. In this paper, MAPE, RMSE and R^2 were used for evaluating the models.

MAPE quantifies the accuracy of predicted values by calculating the average of the absolute percentage errors over all the predictions. The use of MAPE is often suitable for evaluating predictions made for huge datasets. MAPE can be calculated as follows:

$$MAPE = \left(\frac{1}{n}\sum_{i=1}^{n}\left|\frac{p_i - y_i}{y_i}\right|\right) \cdot 100\%, \tag{6}$$

where p_i is the value predicted by the model, y_i is the actual value from the dataset and n is the number of values in the dataset.

RMSE is another metric commonly employed in regression or time series model training. It quantifies the deviation of the predicted data from the line of best fit. It can serve as a decisive factor for choosing the most effective forecasting model from a set of models trained on the same dataset. RMSE can be calculated as follows:

$$RMSE = \sqrt{\frac{1}{n}\left(\sum_{i=1}^{n}(p_i - y_i)^2\right)}. \tag{7}$$

R[2], also known as the coefficient of determination, is a statistical metric used in regression analysis to quantify the percentage of variance in the dependent variable that can be predicted by the independent variable. R^2 quantifies the degree to which the regression model fits the dataset. R^2 can be calculated as follows:

$$R^2 = 1 - \frac{\sum_{i=1}^{n}(y_i - p_i)^2}{\sum_{i=1}^{n}(y_i - \hat{y})^2} \tag{8}$$

where $\hat{y}$ is the mean value of the dataset. A model can be considered as a good fit if its R^2 value is close to 1.

4. DANUBE WATER LEVEL DATA

The source of the data used for creating ELM water level prediction models comes from the hydrology section of the online-accessible weather records of Republic Hydrometeorological Service of Serbia (RHSOS) which contains measurements of a variety of hydrological characteristics of rivers in Serbia [44]. These characteristics include daily water level, water temperature, water flow measurements, ice phenomena, quality of water, and more.

The water level data provided by RHSOS is collected from the network of measurement stations installed on various locations including many rivers and lakes in Serbia. As of 2023, a total of 211 such stations are located throughout the territory of Serbia, with 15 of those stations being located on the Danube River [45]. There are a number of instruments that are utilized at the stations in order to measure the water level such as limnigraph water gauges and/or digital devices. At each station, measuring of the water level takes place once a day at a particular hour, on a regular basis. Water level is measured in centimeters and relative to a zero-elevation point defined for each station. Zero-elevation points are given in meters above the Adriatic Sea.

Every year, in the middle of the year, RHSOS publishes an annual report that includes information on the surface water parameters that were measured during the previous year. The section of the annual report regarding water level includes daily measurements for all stations, as well as minimum, average, and maximum readings for each month and for the entire year.

The ELM model for predicting the Danube water level was developed based on data from several RHSOS annual reports. Out of the total of 15 stations, 7 were selected: Bezdan, Novi Sad, Zemun, Banatska Palanka, Veliko Gradište, Donji Milanovac, and Prahovo. The RHSOS online source offers reports starting from 1991 up to 2021 (at the time of developing the models). However, for some stations, data before a particular year is missing and only a subset of the annual reports was used per station, starting from the year when the data was recorded for the first time for the given station and up to 2021 Fig. 3 provides a graphical representation of each of the stations' datasets, where water level values are shown relative to the Adriatic Sea level i.e. including the zero-elevation points of each station. Fig. 4 shows the distribution of water levels appearing in the data set relative to zero-elevation points. Table 1 presents a summary of station statistical details as well as the starting year of the subset of annual reports used for a particular dataset. Table 2 shows a sample of one of the datasets.
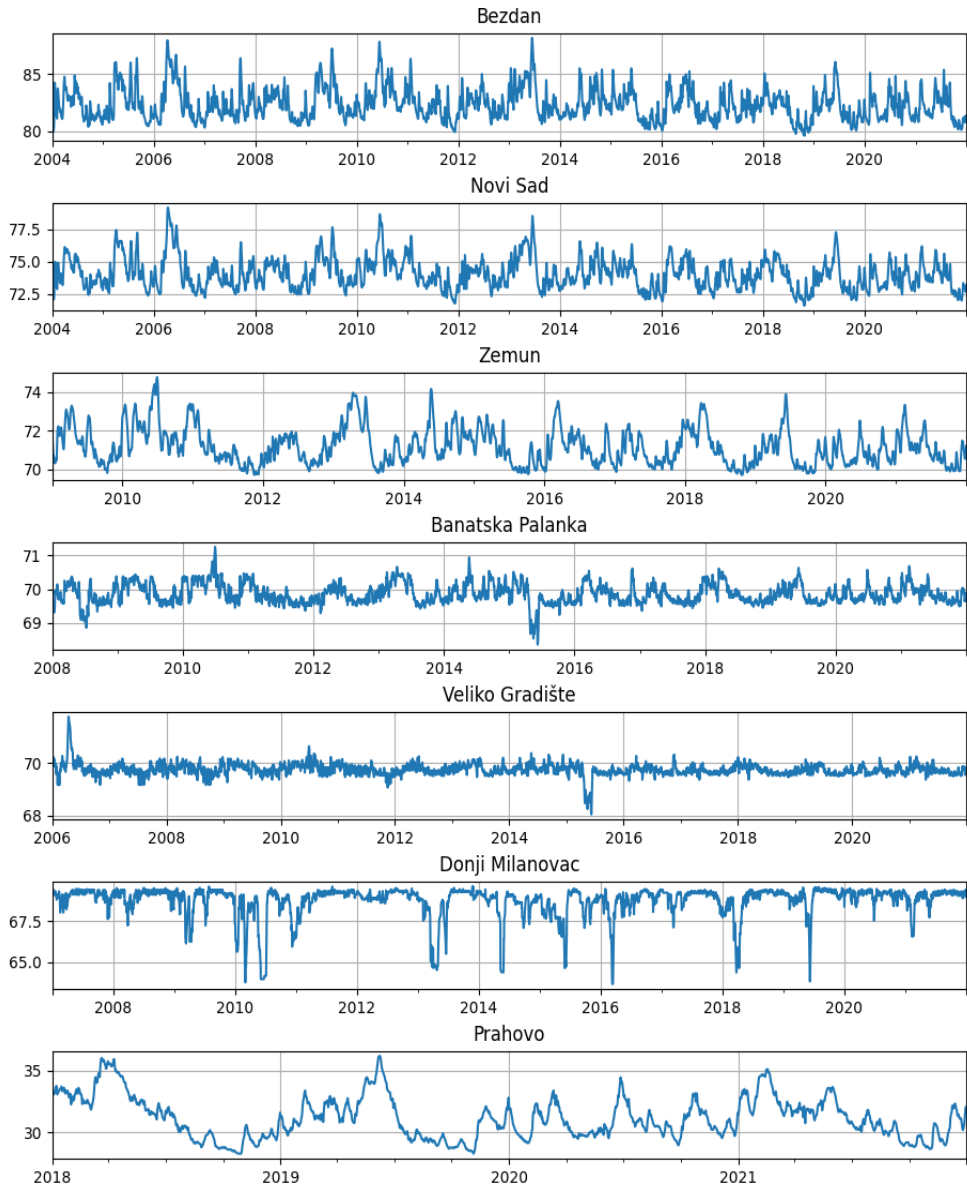
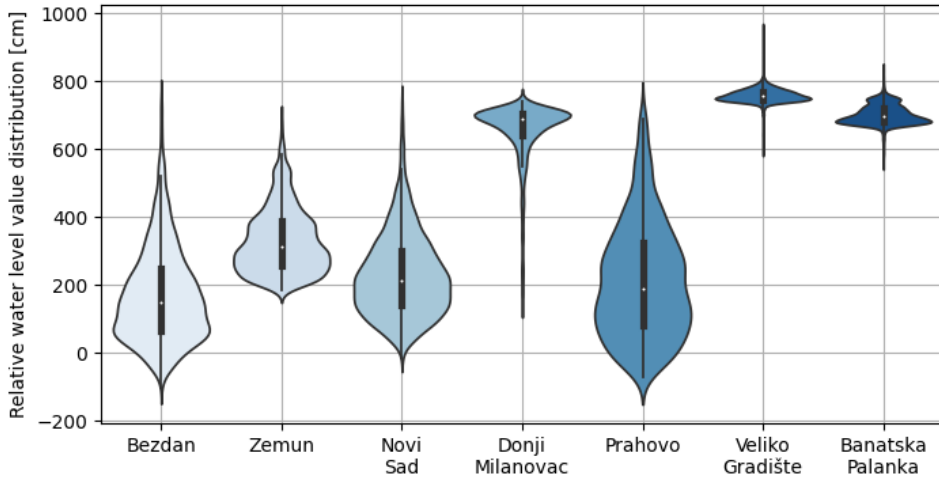**Fig. 3** Water level data measurements from each station

Fig. 4 Water level distribution violin plots across stations

Table 1 Statistical details of different datasets

	Bezdan	Novi Sad	Zemun	Donji Milanovac	Veliko Gradište	Banatska Palanka	Prahovo
Zero-elevation [m]	80.64	71.73	67.87	62.24	62.17	62.85	29.02
Starting year	2004	2004	2009	2007	2006	2008	2018
No. of samples	6575	6575	4748	5479	5844	5114	1461
Mean relative water level [cm]	171.64	230.49	331.28	651.34	757.64	701.14	214.18
Std. deviation	139.4	121.35	95.51	97.44	23.01	29.75	168.41
Min. [cm]	-101	-13	184	140	588	551	-72
25% (Q1) [cm]	166	141	256	642	745	680	80
50% (Q2) [cm]	148	215	312	687	755	695	190
75% (Q3) [cm]	248	302	388	705	770	721	324
Max. [cm]	755	744	691	742	960	840	718

For each dataset, the data from the reports has been organized into a single time series with samples ranging from a starting date to 31.12.2021. and then stored in individual *.csv* files. Missing data was imputed using linear interpolation. In order to eliminate unwanted noise in the data, a convolution filter (Centered Moving Average) was employed on each individual dataset.

5. DEVELOPMENT AND TRAINING OF ELM MODELS

Prediction of the next sample in a time series is in most cases based on the samples collected in a number of previous consecutive timesteps. For this purpose, the data is firstly reorganized into input-output pairs that are appropriate for time series prediction before the ELM models are trained. The sliding window technique is used to generate vector pairs for each model. This involves creating input-output pairs from consecutive dataset points of each dataset. For a model with an input length of *N,* the *i*-th pair is formed by taking in

total $N+1$ consecutive points, with points x_i, x_{i+1}, x_{i+2}, … x_{i+N-1}, forming the input vector of the pair and taking x_{i+N} as the target or the desired output. The total number of input-output pairs generated in this way is n-N-1, where n is the length of the dataset used for training. In this paper, 70% of all reorganized data in each dataset was used for training. The accuracy of the forecast can be influenced by the length of the input vector, also known as the prediction horizon, depending on the time series [46]. This study involved developing models for each station with input lengths taking 30, 60, 120, 180, and 365 samples and then selecting the model that yields the most accurate predictions after training. This accounts for a total of 35 models, one per horizon length and per dataset.

The structure of each ELM model is selected using the method of optimal pruning described in detail in [47]. This method involves selecting an initial number of hidden neurons, grading the neurons according to their "usefulness" (using RMSR [48]), then performing a Leave-One-Out (LOO) cross-validation to evaluate the model performance and, in the end, discarding some of the neurons based on their grade and the results of LOO. For models in this study, hidden layers were initially assigned 600 neurons in total, 100 of them implementing the sigmoid activation function and the other 500 the radial basis function with L2 norm, which is commonly used in ELMs [49].

6. RESULTS AND DISCUSSION

After training all the models, prediction testing was conducted using the corresponding test sets, which consisted of the remaining 30% of the data set that was not used for training. Table 3 shows the accuracy metrics for each station across different horizons, together with the count of hidden neurons in each network following optimal pruning. Fig. 5 shows the graphical representation of predictions with the highest R^2 value among different horizons over the entire test set for each station. Additionally, the subset of 60 consecutive predictions for which each stated model had the lowest RMSE is shown. Predicted values take the zero-elevation level into account. Plot lines colored in blue represent the actual recorded values, while red lines represent predictions.

Given the results in the tables, it can be concluded that the methodology used for generating and training has yielded models that perform very well across nearly all datasets. Most of the models obtained an R^2 value larger than 0.95, except for the model for the Veliko Gradište station which resulted in R^2 around 0.86 across all horizons due to larger levels of noise in the data than in the other datasets, but had considerably low RMSE values on the other hand. Among all the datasets, the Prahovo station had the smallest number of samples and thus the small training and test sets, which explains the drop in R^2 as the horizon increases. It can also be noticed that the longer the horizon, the less neurons would be dropped out of the network after pruning. Overall, the models were able to closely match the trend and predict sudden rises/drops of the water level, regardless of the water level values distribution and the value of the zero-elevation point.

Table 2 Summary of prediction accuracy and network complexity according to different criteria – a) Bezdan model, b) Zemun model, c) Novi Sad, d) Veliko Gradište model, e) Donji Milanovac model, f) Banatska Palanka model, g) Prahovo model

Bezdan	MAPE [%]	RMSE [cm]	R^2	Sigmoid neurons	RBF L2 neurons
30	0.0759	9.5251	0.9932	30	160
60	0.0784	9.7075	0.9930	48	268
120	0.0858	10.2512	0.9922	81	433
180	0.0888	10.4440	0.9920	92	479
365	0.1154	12.8260	0.9881	100	500

Zemun	MAPE [%]	RMSE [cm]	R^2	Sigmoid neurons	RBF L2 neurons
30	0.0556	5.2561	0.9961	21	114
60	0.0579	5.4199	0.9959	47	206
120	0.0604	5.6002	0.9956	60	334
180	0.0705	6.3614	0.9939	99	485
365	0.0817	7.3589	0.9907	100	500

Novi Sad	MAPE [%]	RMSE [cm]	R^2	Sigmoid neurons	RBF L2 neurons
30	0.0550	5.6510	0.9968	28	138
60	0.0563	5.7810	0.9967	39	218
120	0.0604	6.1031	0.9963	78	388
180	0.0619	6.1402	0.9963	100	495
365	0.0832	7.9453	0.9939	100	500

Veliko Gradište	MAPE [%]	RMSE [cm]	R^2	Sigmoid neurons	RBF L2 neurons
30	0.0562	5.1765	0.8642	8	48
60	0.0558	5.1451	0.8653	39	171
120	0.0558	5.1348	0.8667	39	217
180	0.0553	5.0975	0.8679	62	265
365	0.0561	5.1336	0.8678	99	499

D. Milanovac	MAPE [%]	RMSE [cm]	R^2	Sigmoid neurons	RBF L2 neurons
30	0.1202	11.9476	0.9747	25	99
60	0.1213	11.9684	0.9747	51	238
120	0.1226	12.0287	0.9747	89	445
180	0.1245	12.1552	0.9744	100	500
365	0.1301	12.5917	0.9732	100	499

Ban. Palanka	MAPE [%]	RMSE [cm]	R^2	Sigmoid neurons	RBF L2 neurons
30	0.0559	5.0858	0.9562	35	152
60	0.0557	5.0737	0.9565	49	209
120	0.0551	5.0256	0.9576	48	267
180	0.0550	5.0179	0.9580	93	469
365	0.0555	5.0105	0.9564	100	497

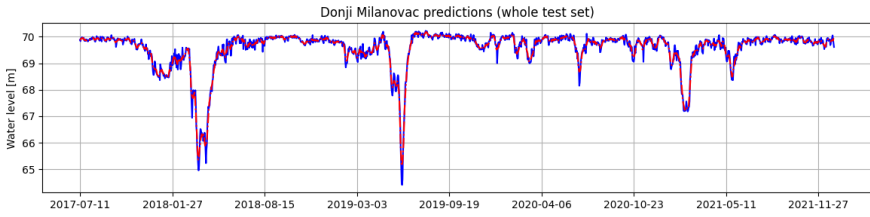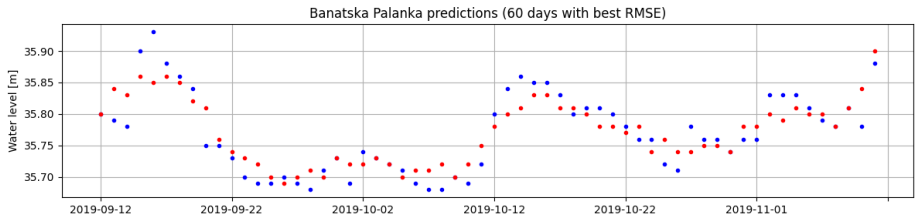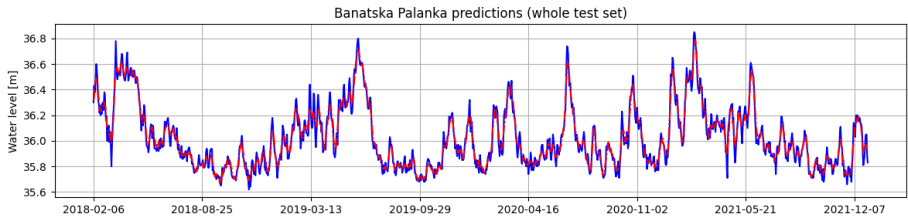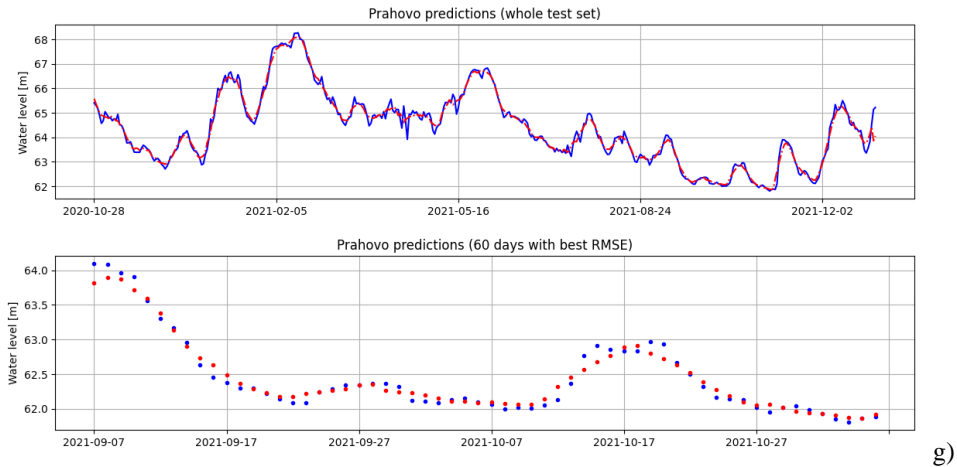| Prahovo	MAPE [%]	RMSE [cm]	R^2	Sigmoid neurons	RBF L2 neurons
30	0.4234	18.9374	0.9833	14	79
60	0.4210	18.9479	0.9836	29	163
120	0.8653	34.2724	0.9483	84	408
180	1.0182	40.1830	0.9301	87	363
365	2.0199	78.2243	0.7353	77	406

a)

b)

c)

d)

e)

f)

g)
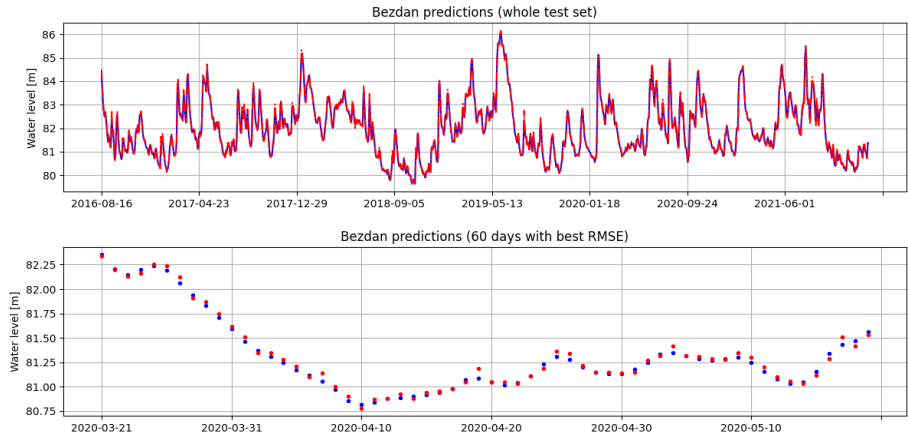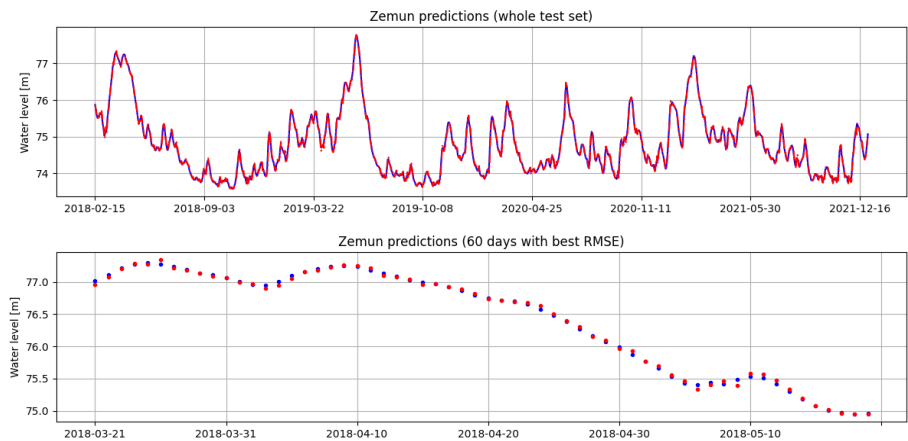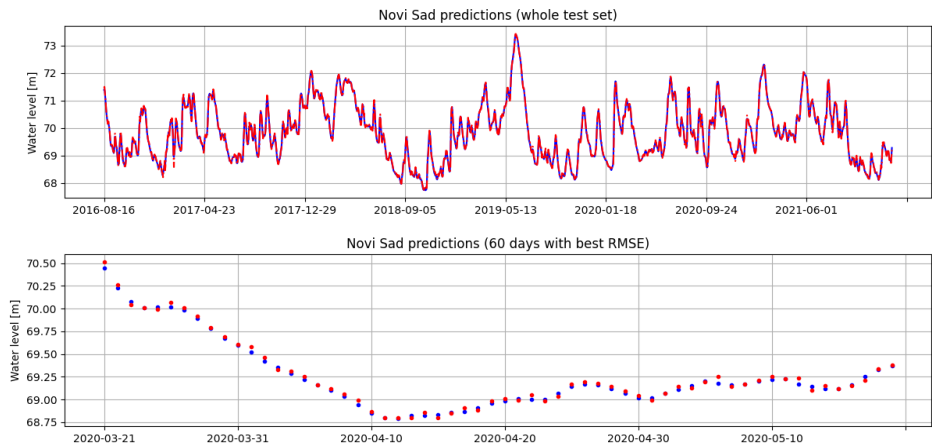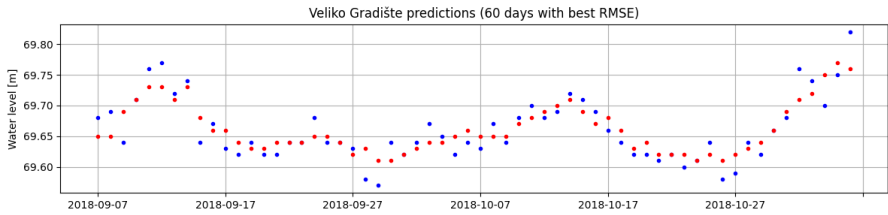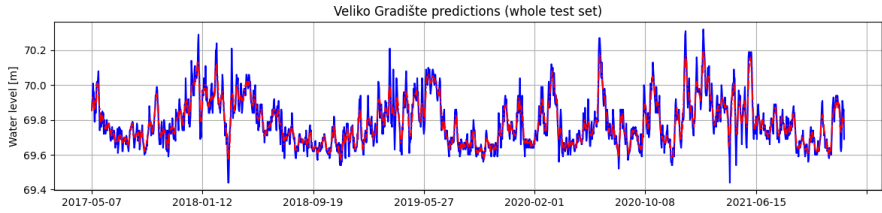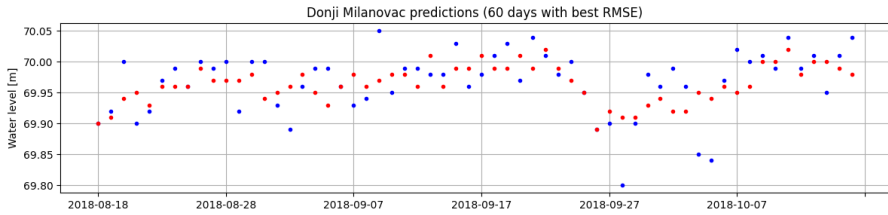
Fig. 5 Predictions for different models and best RMSE days – a) Bezdan model, b) Zemun
model, c) Novi Sad, d) Veliko Gradište model, e) Donji Milanovac model, f) Banatska
Palanka model, g) Prahovo model

7. CONCLUSION

This research examines the use of Extreme Learning Machine for predicting the daily water level of the Danube River. Numerous experiments with different ELM hidden neuron structures have been conducted across various datasets of different water level distributions. Models' accuracies were assessed in order to determine the optimal models for each dataset.

The ELM models demonstrated promising results in terms of prediction, considering their complexity, accuracy, and training time across most datasets. Most models showed desirable R^2 values (above 0.95), except for the Veliko Gradište station model, which had lower R^2 values due to higher data noise but low RMSE values. Regardless of the water level distribution or zero-elevation point, the models were able to accurately predict the water level.

For future studies, modifications of the models could be applied to further investigate the effect of different model parameters and properties on the models' predictive power. For instance, the number of output neurons could be increased in order to perform predictions for longer periods, such as one week or one month ahead. Since the models in this paper contained neurons of mixed activation functions, the effect of each activation function could be investigated by creating models with hidden layers with a single activation function and their performance can be compared with the models with mixed-activation function in hidden layers' neurons.

REFERENCES

[1]   J. Fabryka-Martin, and J. Merz, "The Study of Water and Water Problems: A Challenge for Today and Tomorrow", Universities Council on Water Resources, Hydrology, Carbondale, Ill., 1983.

[2]   P. Dabral, and Z. M. Mharhoni. "Modelling and forecasting of rainfall time series using SARIMA", *Envir. Processes,* vol. 4, no. 2, pp. 399-419, 2017, doi.org/10.1007/s40710-017-0226-y.

[3]   O. Bazrafshan, A. Salajegheh, J. Bazrafshan, M. Mahdavi, and A. F. Maraj. "Hydrological drought forecasting using ARIMA models (case study: Karkheh Basin)", *Ecopersia* vol.3, no. 3, pp. 1099-1117, 2015.

[4]   W. Handoko, and A. N. Handayani. "Forecasting Solar Irradiation on Solar Tubes Using the LSTM Method and Exponential Smoothing", *J. Ilm. Tek. Elektro Komput. dan Inform*, vol. 9, no. 3, pp. 649-660, 2023, DOI: http://dx.doi.org/10.26555/jiteki.v9i3.26395.

[5]   Y. Du, J. Wang, W. F. S. Pan, T. R. Xu, and C. Wang. "Adarnn: Adaptive learning and forecasting of time series", In *Proceedings of the 30th ACM international conference on information & knowledge management*, pp. 402-411. 2021.

[6]   M. Bender, and S. Simonovic. "Time-series modeling for long-range stream-flow forecasting", *Journal of Water Resources Planning and Management*, vol. 120, no. 6, pp. 857-870, 1994, https://doi.org/10.1061/(ASCE)0733-9496(1994)120:6(857)

[7]   D. Noakes, A. I. McLeod, and K. Hipel. "Forecasting monthly riverflow time series", *International Journal of Forecasting,* vol. 1, no. 2, pp. 179-190, 1985, https://doi.org/10.1016/0169-2070(85)90022-6.

[8]   J. Torres, D. Hadjout, A. Sebaa, F. Martínez-Álvarez, and A. Troncoso. "Deep learning for time series forecasting: a survey", *Big Data* vol. 9, no. 1, pp. 3-21. 2021, doi.org/10.1089/big.2020.0159.

[9]   D. C. McKinney. "Modeling water resources management at the basin level: Review and future directions", International Water Management Institute, (1999), ISBN: 9789290903765.

[10] H. Maier, and G. C. Dandy. "Application of artificial neural networks to forecasting of surface water quality variables: issues, applications and challenges", *Artificial neural networks in hydrology (Book Section) - Springer*, pp. 287-309, 2000, doi.org/10.1007/978-94-015-9341-0_15

[11] R. Solgi, H. Loaiciga, and M. Kram. "Long short-term memory neural network (LSTM-NN) for aquifer level time series forecasting using in-situ piezometric observations", *Journal of Hydrology* vol. 601, October 2021, 126800, doi.org/10.1016/j.jhydrol.2021.126800.

[12] H. Han, C. Choi, J. Jung, and H. Kim. "Application of sequence to sequence learning based LSTM model (LSTM-s2s) for forecasting dam inflow", *Journal of Korea Water Resources Association* vol. 54, no. 3, pp. 157-166, 2021,

[13] K. Park, Y. Seong, Y. Jung, I. Youn, and C. K. Choi. "Development of Water Level Prediction Improvement Method Using Multivariate Time Series Data by GRU Model", *Water* vol. 15, no. 3 pp. 587, 2023, doi.org/10.3390/w15030587.

[14] K. Park, Y. Jung, Y. Seong, and S. Lee. "Development of deep learning models to improve the accuracy of water levels time series prediction through multivariate hydrological data", *Water* vol.14, no. 3, pp. 469, 2022, doi.org/10.3390/w14030469.

[15] N. Bezak et al., "A catalogue of the flood forecasting practices in the Danube River Basin", River Research and Applications, vol. 37, no. 7, pp. 909-918, 2021, doi.org/10.1002/rra.3826.

[16] T. Zabolotnia, L. Gorbachova, and B. Khrystiuk, "Estimation of the long-term cyclical fluctuations of snow-rain floods in the Danube basin within Ukraine", Meteorology Hydrology and Water Management. Research and Operational Applications, vol.7, no. 2, pp. 3-11, 2019.

[17] I. M. Santos et al., "Analysis of seasonal hindcasts for mean-term hydrological forecasting in the Upper Danube River Basin", Geophysical Research Abstracts, vol. 21, ISSN: 1029-7006, 2019.

[18] A. Z. Liptay, and B. Gauzer, "Operational River Ice and Water Temperature Forecasting on the Hungarian Danube Reach", FLOOD risk 2020 - 4th European Conference on Flood Risk Management, Budapest University of Technology and Economics, http://hdl.handle.net/10890/15156, 2021.

[19] D. Hussain et al., "A deep learning approach for hydrological time-series prediction: A case study of Gilgit river basin", Earth Science Informatics, vol. 13, pp. 915-927, 2020, doi.org/10.1007/s12145-020-00477-2.

[20] Z. Wang, and Y. Lou, "Hydrological time series forecast model based on wavelet de-noising and ARIMA-LSTM", In 2019 IEEE 3rd Information Technology, Networking, Electronic and Automation Control Conference (ITNEC), pp. 1697-1701, IEEE, March, 2019.

[21] Z. M. Yaseen et al., "Non-tuned machine learning approach for hydrological time series forecasting", Neural Computing and Application, vol. 30, pp. 1479-1491, 2018.

[22] W. J. Niu et al., "Parallel computing and swarm intelligence based artificial intelligence model for multi-step-ahead hydrological time series prediction", Sustainable Cities and Society, vol. 66, 2021, doi.org/10.1016/j.scs.2020.1026.

[23] Z. K. Feng et al., "Evolutionary artificial intelligence model via cooperation search algorithm and extreme learning machine for multiple scales nonstationary hydrological time series prediction", Journal *of Hydrology*, vol. 595, 2021, doi.org/10.1016/j.jhydrol.2021.1260.

[24] J. Qin et al., "Simulating and Predicting of Hydrological Time Series Based on TensorFlow Deep Learning", Polish Journal of Environmental Studies, vol. 28, no. 2, 2019, DOI: 10.1524/pjoes/81557.

[25] M. Jeremić, M. Milić, J. Milojković, and M. Gocić, "Development of geo-da based android application for spatial and statistical analysis of Serbian long-term precipitation data", FACTA UNIVERSITATIS Series: Automatic Control and Robotics, vol. 21, no. 3, pp. 131-145, 2021, doi.org/10.2219/FUACR220623011J.

[26] M. D. Mijatović, Ž. Bjelajac, and I. Joksić, Overview of the ecological, economic and security capacities of the Danube River (in Serbian), Danubius, ISSN: 2217-4826, 2012.

[27] P. Pekarova et al., "Statistical analysis of hydrological regime of the Danube River at Ceatal Izmail Station", IOP Conference Series: Earth and Environmental Science. vol. 221, no. 1. IOP Publishing, 2019, DOI 10.1088/1755-1315/221/1/012035.

[28] T. Pulka et al., "A Near Real-Time Hydrological Information System for the Upper Danube Basin", Hydrology vol. 8, no. 4, 2021, doi.org/10.3390/hydrology8040144.

[29] ICPDR. Danube Basin: Facts & Figures. International Commission for the Protection of the Danube River. Available online: https://www.icpdr.org/flowpaper/viewer/default/files/nodes/documents/icpdr_facts_figures.pdf (accessed on 1 December 2020).

[30] P. Pekárová et al., "Identification of long-term high-flow regime changes in selected stations along the Danube River", Journal of Hydrology and Hydromechanics, vol. 64, no. 4, pp. 393-403, 2016, DOI: 10.1515/johh-2016-0045.

[31] J. Wesemann, H. Holzmann, K. Schulz, and M. Herrnegger, "Behandlung künstlicher Speicher und Überleitungen in der alpinen Niederschlags-Abfluss-Vorhersage", Osterr. Wasser Abfallwirtsch. vol.70, no. 11, pp. 485-496, 2018, DOI: 10.1007/s00506-018-0501-9.

[32] D. Bănăduc et al., "The Danube Delta: The Achilles Heel of Danube River–Danube Delta–Black Sea Region Fish Diversity under a Black Sea Impact Scenario Due to Sea Level Rise—A Prospective Review", Fishes, vol. 8, no. 7, 2023, doi.org/10.3390/fishes8070355.

[33] A. M. Petrović, I. Novković, and S. Kostadinov, "Hydrological analysis of the September 2014 torrential floods of the Danube tributaries in the Eastern Serbia", Natural Hazards, vol. 108, pp. 1373-1387, 2021.

[34] K. P. Schneider et al., "A Distributed Power System Control Architecture for Improved Distribution System Resiliency", IEEE Access, vol. 7, pp. 9957-9970, DOI: 10.1109/ACCESS.2019.2891, 2019.

[35] A. Bidram, F. L. Lewis and A. Davoudi, "Distributed Control Systems for Small-Scale Power Networks: Using Multiagent Cooperative Control Theory," IEEE Control Systems Magazine, vol. 34, no. 6, pp. 56-77, Dec. 2014, doi: 10.1109/MCS.2014.2350.

[36] Flood recovery and prevention, Studie, https://neighbourhood-enlargement.ec.europa.eu/system/files/2016-12/ipa2014_037788.06_rs_floods_recovery_and_prevention.pdf.

[37] G. B. Huang, Q. Y. Zhu and C. K. Siew, "Extreme Learning Machine: Theory and Applications", Neurocomputing, vol. 70, no. 1, pp. 489-501, 2006, doi.org/10.1016/j.neucom.2005.12.126.

[38] C. W. Deng, G. B. Huang, J. Xu, and J. X. Tang, "Extreme learning machines: new trends and applications" Science China, Information Sciences, vol. 58, no. 2, pp. 020301–020301, 2015, doi.org/10.1007/s11432-014-5269-3.

[39] G. B. Huang, D. H. Wang, and Y. Lan, "Extreme Learning Machines: A Survey", International Journal of Machine Learning and Cybernetics, vol. 2, no. 2, pp. 107-122, 2011, doi.org/10.1007/s13042-011-0019-y.

[40] Aranildo R. Lima, Alex J. Cannon, William W. Hsieh, "Nonlinear regression in environmental sciences using extreme learning machines: A comparative evaluation", Environmental Modelling & Software, vol. 73, pp. 175-188, 2015, doi.org/10.1016/j.envsoft.2015.08.002

[41] S. Ding, H. Zhao, Y. Zhang, X. Xu and R, Nie, "Extrem.e learning machine: algorithm, theory and applications", Artificial Intelligence Review, vol. 44, no. 1, pp. 103–115, 2015, doi.org/10.1007/s10462-013-9405-z.

[42] M. van Heeswijk, Y. Miche, E. Oja, A. Lendasse, "GPU-accelerated and parallelized ELM ensembles for large-scale regression", Neurocomputing, vol. 74, no. 16, pp. 2430-2437, 2011, doi.org/10.1016/j.neucom.2010.11.034.

[43] J. C. A. Barata, M. S. Hussein, "The Moore-Penrose Pseudoinverse. A Tutorial Review of the Theory", Brazilian Journal of Physics, vol. 42, pp. 146-165, 2011, doi.org/10.4855/arXiv.1110.6882

[44] Annual reports for hydrological data of Danube River 1991-2021 (in Serbian), available online at: https://www.hidmet.gov.rs/ciril/hidrologija, Accessed on 10th of December 2023.

[45] "Operational jobs in general working program of surface water hydrological stations network", Republic Hydrometeorological Service of Serbia, available online at: https://www.hidmet.gov.rs/latin/hidrologija/delatnost_mreza.php, Accessed on 10th of January 2024.

[46] M. Andrejević Stošović, N. Radivojević, I. Jovanović and A. Petrušić, "Artificial Neural Networks Application to Prediction of Electricity Consumption". Facta Universitatis, Series: Automatic Control and Robotics, 20(1), 033-042. Doi: HTTPs://doi.org/10.2219/FUACR201231003A.

[47] Y. Miche et al., "OP-ELM: Optimally Pruned Extreme Learning Machine", in IEEE Transactions on Neural Networks, vol. 21, no. 1, pp. 158-162, Jan. 2010, DOI: 10.1109/TNN.2009.2036.

[48] T. Similä and J. Tikka, "Multiresponse sparse regression with application to multidimensional scaling", in Proc. Int. Conf. Artif. Neural Netw., pp. 97–102, 2005 DOI:10.1007/11550907_16.

[49] Ch. S. K. Dash, A. K. Behera, S. Dehuri and S. B. Cho, (2016). "Radial basis function neural networks: A topical state-of-the-art survey", Open Computer Science, vol. 6, no. 1, 2016, DOI 10.1515/comp-2016-0005.